Development of X-ray Dark-Field Imaging for Early Clinical Diagnosis of Arthropathy

Daisuke SHIMAO

DOCTOR OF PHILOSOPHY

Department of Materials Structure Science
School of High Energy Accelerator Science
The Graduate University for Advanced Studies

2005

Contents

List of figures

List of tables

Chapter 1

Introduction

X-rays are widely applied in different scientific fields as a non-destructive examination for the observation of internal structures. Especially in the field of clinical medicine, X-ray absorption contrast images are easily interpreted and have proved to be useful in medical diagnosis as projection image or computer tomography (CT). Projection images are used to visualize bone for diagnosing bone fractures and bone alignment, for observing the condition of the chest, and for abdominal imaging; angiography, urography, arthrography and digestive tract imaging are undertaken using contrast medium. In using these methods, however, there is insufficient soft tissue contrast to enable the detection of pathologic lesions because the image contrast is based on differences in the linear absorption coefficient μ. The differences in μ in bone, contrast medium and

soft tissues are sufficiently large to provide contrast but insufficient to provide adequate contrast between different soft tissues. Contrast between tissues with small differences in μ can only be detected using lower incident X-ray energy. Mammography, which utilizes low X-ray energy from a dedicated X-ray tube, is the only imaging method that aims to depict soft tissue.

So far several kinds of X-ray imaging have been developed based on the slight differences in the refractive index n:

$$n=1-\delta \tag{1}$$

of an object [1-29] using synchrotron radiation [7-9, 12, 14-19, 21-29] and have been studied with a view to their medical application [30-65]. Here δ is the unit decrement of the refractive index

$$\delta = \frac{e^2}{mc^2}\frac{N\lambda^2}{2\pi}\frac{Z\rho}{A} \tag{2}$$

where e^2/mc^2 is the classic electron radius, λ is the wavelength, N is the Avogadro number, ρ is the medium density and Z and A are the medium atomic number and weight, respectively. Therefore, δ is proportional to ρ and λ^2 and is approximated as follows [31],

$$\delta \cong 1.35\times10^{11}\times\rho\lambda^2 \tag{3}$$

Three major techniques for detecting the effect of refraction by an object have been attempted for medical applications. The simplest method is in-line holography [4, 5, 7-11, 13-15, 19, 20, 32-34, 37, 41-43, 51, 61,

65]. The method works with both monochromatic and polychromatic X-rays, and differs from conventional X-ray absorption contrast imaging only in that a gap is introduced between the object and the detector to allow sufficient distance for refracted and non-refracted X-rays to interfere and produce contrast. Fine edge enhancement of the borders between objects is produced, with relatively large differences in their refractive indices. The technique has been performed using both conventional microfocus X-ray sources [4, 5, 10, 11, 13, 20] and synchrotron radiation [7-9, 14, 15, 19, 32-34, 37, 41-43, 51, 61, 65] and has been studied for medical applications in mammography [34, 61] and the imaging of bone [33, 37, 41], articular cartilage [51], the chest [42, 65] and foreign bodied [43].

The second method for detecting refraction effects exploits the narrow angular acceptance of Bragg diffraction in a perfect silicon crystal. In practice, this is realized using monochromatic synchrotron X-rays. An analyzer crystal is positioned behind an object and resolves those X-rays refracted by the object. Two types of crystal geometry for diffraction have been studied: Bragg and Laue case methods. The Bragg case method has been actively researched internationally using a line-scanning method to obtain the necessary field of view (FOV), which needs scanning the object and detector at the same speed through the line beam [12, 25, 27, 34, 38, 39, 44, 46, 53, 58], with the exception of ref. [31]. Only those X-rays that satisfy the Bragg condition for the analyzer are diffracted into a detector to

form an image. This method has been applied to imaging of the breast [31, 34, 53], articular cartilage and/or tendons [38, 39, 44, 58]. If the analyzer crystal is prepared sufficiently thin that forward diffracted X-rays are transmitted, two kinds of images are formed on diffracted and forward diffracted X-rays [24, 29]. The Laue case method using X-rays was first applied to imaging by Ingal *et al.* [6]. The authors demonstrated the principles of the technique and took images of aquarium fish and test samples made of Plexiglas containing air and 5% KBr solution on the forward diffracted X-rays using laboratory X-ray source. Lately, supporting their idea I have applied this method to the imaging of ligaments and articular cartilage using synchrotron X-rays [45, 47, 51]. X-ray Dark-Field Imaging (DFI) utilizing Laue geometry has recently been proposed by Ando *et al.* [21, 22, 23]. This novel method differs from that of by Ingal *et al.* [6] in terms of introducing tuning of incident X-ray energy and the thickness of analyzer crystal; this allows the intensity of forward diffracted X-rays to approach zero at the Bragg condition. Consequently, X-rays that are non-refracted at an object no longer pass through in the forward diffraction direction. Higher image contrast related to refraction by an object can be expected with DFI, as minute contrast can be detected with almost no background illumination. DFI has been applied to the imaging of bone [21, 23, 48, 49], articular cartilage [48, 49, 50, 55, 60] and breast

specimens [52, 55, 60]. Imaging that utilizes Laue geometry is basically performed by two-dimensional (2D) single-shot method.

The third method is X-ray interferometry, which offers phase contrast images based on the phase shift of X-rays at an object. An X-ray interferometer with three or four blades is usually fabricated from a single block of silicon. An interference pattern is obtained when the beam passing through an object interferes with a reference beam that is divided from the incident beam incident on the object and that has the same phase as the incident beam. This interference is generated by the X-ray interferometer. An advantage of this method is that it allows the introduction of known phase shifts into the reference beam, which then enables phase map of the object to be obtained directly from the interference patterns. A detailed description of this method can be found in Momose *et al.* [16, 17, 30, 35, 36, 40]. Fine phase contrast images have been acquired of specimens including such as liver [30, 36], blood vessels [35, 40], and brain [40]; however, this method is the most complex to realize experimentally because minute changes in room temperature and/or vibration of the device are detrimental to the sequential measurements required to acquire a phase map.

All the methods described above have also been developed as CT techniques to create 2D tomograms and three-dimensional (3D) images. These CT images would be extremely useful for image diagnosis in clinical

medicine, however, synchrotron X-rays have fixed incident direction, which necessitates rotation of the object (patient) during image acquisition. As rotation of the patient, which tends to induce patient movement, is unrealistic in terms of patient care, only the 2D one-shot projection imaging method is applicable to clinical imaging.

Conventional plane radiography is currently used for the detection of joint abnormalities such as osteoarthritis and rheumatoid arthritis; however, as cartilage shows little X-ray absorption contrast, diagnosis of joint abnormalities is undertaken by detecting bone erosion and/or measuring the joint space width on the images [66-75]. This method is sensitive only to advanced cases, and cannot detect early-stage structural abnormalities of cartilage. It is therefore desirable to develop a technique that enables the detection of cartilage with high spatial resolution, as this will lead to new treatment strategies for the early stages of cartilage defects. For this reason, many researchers have studied the depiction of cartilage using magnetic resonance imaging (MRI) [76-93], but such a technique remains to be firmly established, and there is demand for an alternative technique.

For the purposes of clinical imaging of articular cartilage, Laue geometry is adopted, as it offers a larger 2D one-shot field size than Bragg geometry using the same size of analyzer crystal; the X-ray DFI technique was introduced to acquire fine contrast of articular cartilage. The object

imaged in the present study was an intact human finger, unsliced and with skin on while sliced and/or naked or skin stripped objects had been used in almost all of the similar studies by other refraction detection techniques. In a projection image, it is difficult to depict articular cartilage located inside an intact object because of the interference of numerous surrounding soft tissues such as skin, adipose tissues and muscles. The main goal of the current study is to overcome this difficulty in order to apply refraction imaging of articular cartilage to a clinical use.

This thesis consists 8 chapters. Chapter 2 summarizes rheumatoid arthritis, one of the most promising clinical applications of X-ray DFI, and the importance of its early image diagnosis. In Chapter 3, X-ray refraction and X-ray DFI are described from a theoretical perspective. The main subject of this thesis deals with the application of X-ray DFI to the early diagnosis of arthropathy. Experiments related to the clinical application of X-ray DFI and experimental results are presented in chapter 4 and 5, respectively. MRI is the current standard examination for the investigation of abnormalities of articular cartilage. In chapter 6, images of the same object acquired by MRI are presented for comparison with X-ray DFI. Based on the results of this study, the applicability of X-ray DFI to the early diagnosis of arthropathy is discussed in Chapter 7. Chapter 8 contains concluding remarks.

Chapter 2

Rheumatoid arthritis
– On behalf of arthropathy –

The term ‘arthropathy’ encompasses rheumatoid arthritis (RA), osteoarthritis (OA), neuropathic arthropathy, infectious arthritis and so on. Among them RA reduces Quality of Life (QOL) as it progresses [94, 95]. Furthermore, some studies from rheumatology clinical settings indicate that patients with RA die earlier than expected in comparison with individuals in the general population of the same age and sex but without the disease [95-98]. Recent pharmacotherapy developments for the treatment of RA using a biologic agent such as cytokine inhibitors have reported that prognosis improves dramatically provided that the biologic agent is used together with the usual antirheumatic [99]. A conception diagram that represents the effects of pharmacotherapy on RA is shown in Fig. 1. If RA

is treated using a cytokine inhibitor and an antirheumatic in the early stage of the disease, dissemination is restrained and the patients' QOL is preserved. Therefore, early diagnosis and treatment are of great importance.

RA is a common systemic autoimmune disease that is prevalent in approximately 1% of the population worldwide. It is multifunctional in origin and is characterized by the inflammation of the membrane lining joints. Its occurrence is more frequent in females than males, which suggests that sex hormones are influential in its etiology. RA occurs most commonly in the fingers and toes, and progressively disseminates to joints throughout the body in later stages of the disease. The diagnosis of RA is based primarily on clinical, radiological, and immunological features. Current laboratory-based serological tests measure factors such as rheumatoid factor (RF). Despite offering reasonable sensitivity, as a diagnostic tool this parameter has poor specificity. It has been recognized for several years that antibodies to anti-perinuclear factor (APF) and keratin (AKA) are highly specific for RA. The antigen of both these antibodies has recently been identified as epidermal filaggrin, an intermediate filament-associated protein involved in the cornification of the epidermis [100, 101]. Profilaggrin which is present in the keratohyaline granules of human buccal mucosa cells is proteolytically cleaved into filaggrin subunits during cell differentiation. The protein is then dephosphorylated and arginine residues are converted into citrulline by the

enzyme peptidylarginine deiminase (PAD) [102].

In 1998, Schellekens *et al.* [103] reported that antibodies that are reactive with synthetic peptides that contain the unusual amino acid citrulline are present in 76% of RA sera. Furthermore, these antibodies display a specificity of 96% for RA. The antibodies in patients with RA that recogniz the citrulline containing epitopes are predominantly of the IgG class and of relatively high affinity. A subsequent paper by the same group reported that an ELISA test based on cyclic citrullinated peptide (CCP) showed superior performance to the linear version in the detection of antibodies to RA [104]. It has also been observed that anti-CCP antibodies can be detected very early in RA and appear to have a high prognostic value as a marker, with good discriminating power between erosive and non-erosive RA.

As described above, immunological researches in this field is currently active, while radiological research is inactive. This inactivity may reflect the fact that conventional X-ray absorption images can reveal bone structure alone. If minute changes in articular cartilage were able to be detected by X-ray, the situation would be different.

Schemas of the joint structure and the function of immunosystem are shown in Fig. 2 (a) and 2 (b), respectively. A typical joint consists of two opposing bones, the tips of which are covered with articular cartilage. Joints are wrapped in articular capsule, which is lined with synovial

membrane and filled with synovial fluid. When bacteria or viruses invade in a joint, they are attacked by antibodies produced in response to the invasion. In the joints of patients suffering from RA, however, antibodies are produced because of immunodeficiency, without the invasion of foreign bodies, and this leads to the destruction of a joint. Figure 3 shows schemas of this process. Figure 3 (a) shows a normal joint. Antibodies produced because of immunodeficiency stimulate synovial membrane (Fig. 3 (b)). Synovitis progresses with swelling of the joint, which leads to the erosion of bones and articular cartilage (Fig. 3 (c)). Articular cartilages disappear and the joint is destroyed (Fig. 3 (d)). Typical photographs and X-ray absorption contrast images of the hands of patients suffering from RA are shown in Fig. 4 and Fig. 5, respectively. Figures 4 (b)-(d) and 5 (b)-(d) show advanced stages that cannot be cured. These findings correspond to the stage of Fig. 3 (d) and easily observed on X-ray absorption contrast images. Relatively early-stage RA showing bone erosion can also be detected by X-ray absorption contrast images, although articular cartilage cannot be depicted; this corresponds to the stage shown in Fig 3 (c). The early diagnosis of RA will be possible with the successful detection of minute changes in articular cartilage and bone surface specific to RA at an earlier stage, such as the stage noted in Figs. 3 (b), 4 (a), and 5 (a), which demonstrate just swelling of joint. The main goal of this study is to develop a method to depict articular cartilage and the bone surface in detail.

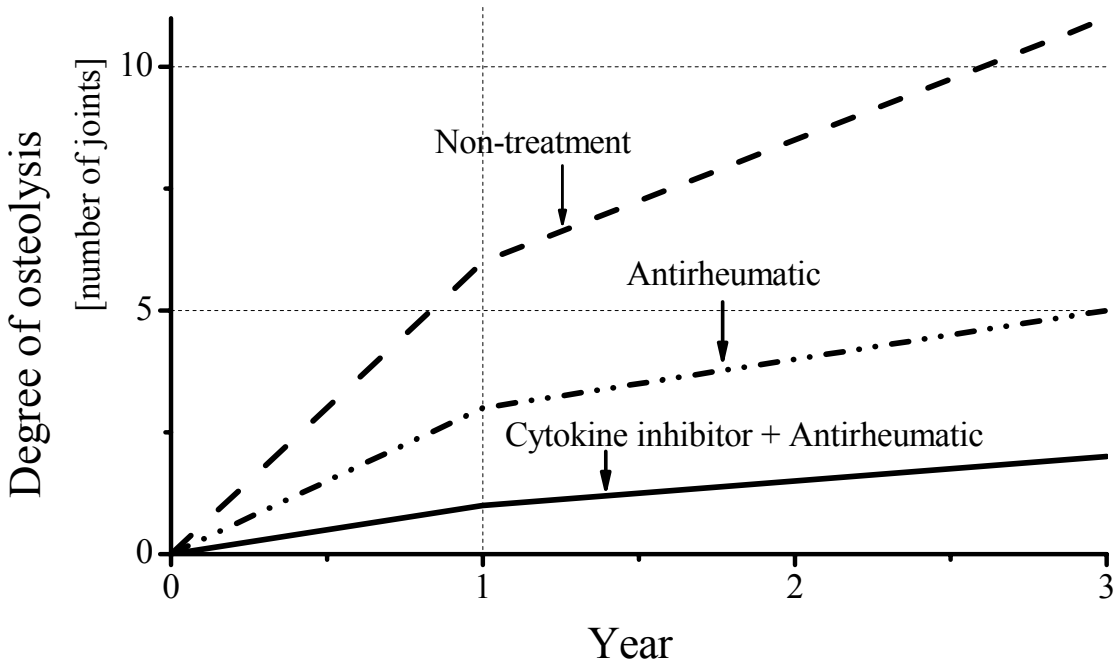

Figure 1. Conception diagram representing the effects of pharmacotherapy on rheumatoid arthritis.

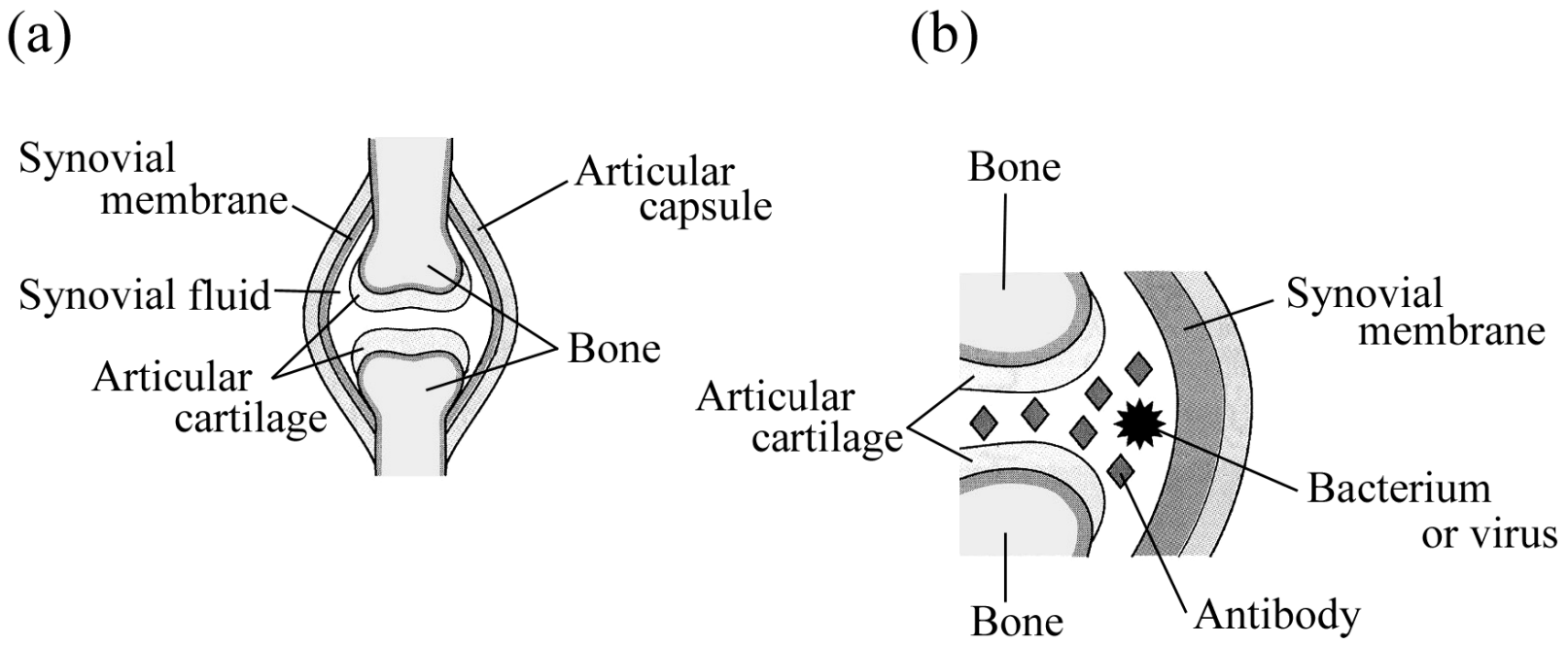

Figure 2. Schemas of (a): joint structure and (b): function of the immunosystem.

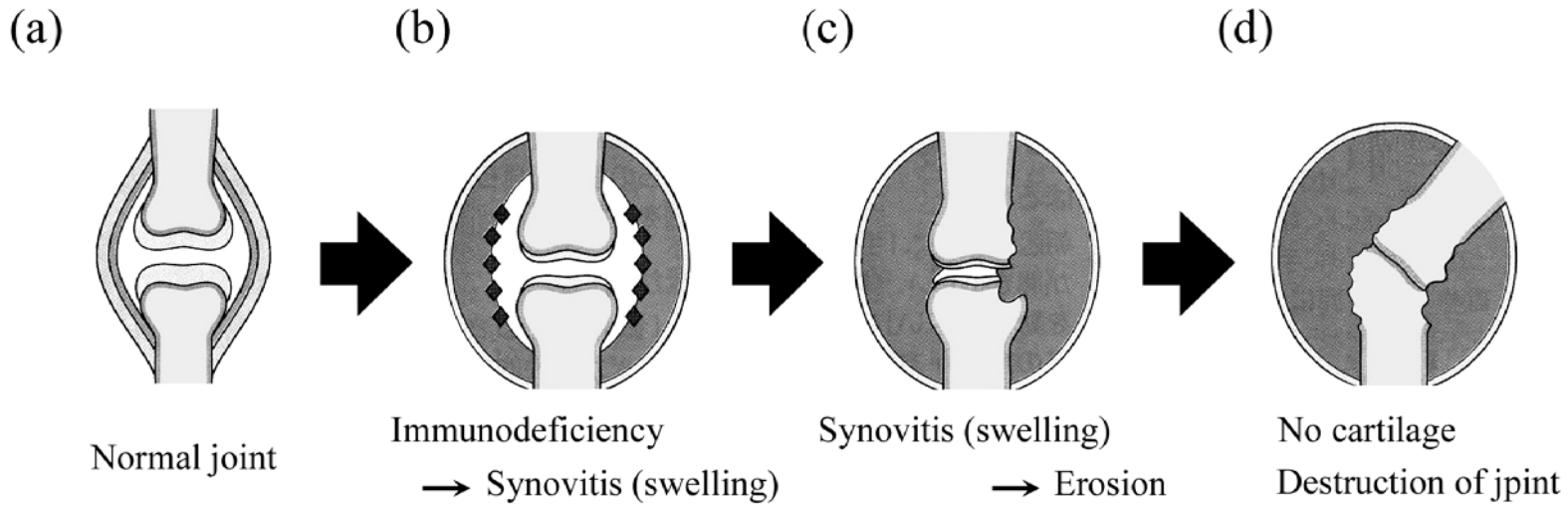

Figure 3. Process of joint destruction due to rheumatoid arthritis.

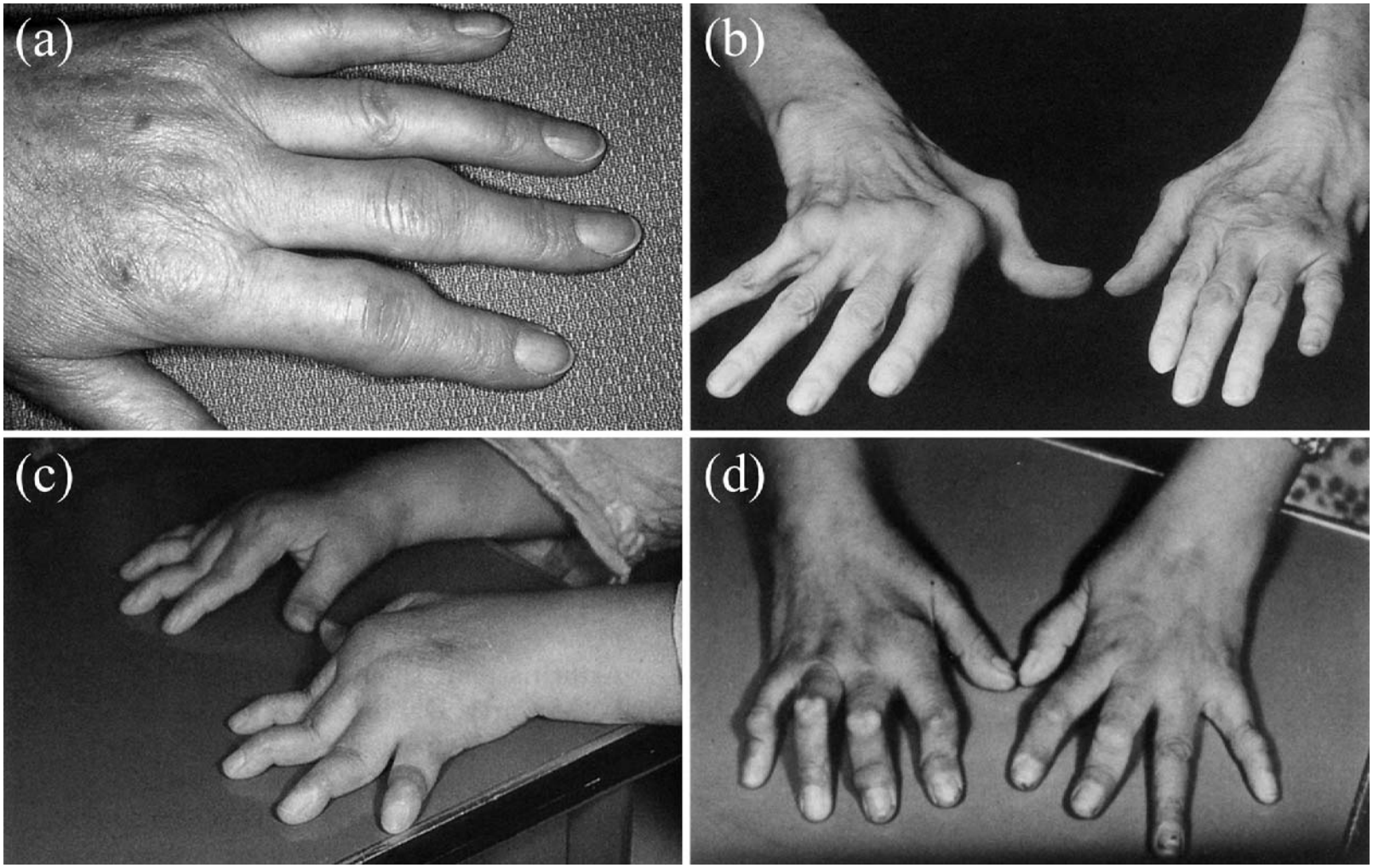

Figure 4. Photographs of typical appearances of the hands of patients suffering from rheumatoid arthritis in (a): early stages and (b)-(d): advanced stages.

Figure 5. Typical X-ray absorption contrast images of the hands of patients suffering from rheumatoid arthritis in (a): early stages and (b)-(d): advanced stages.

Chapter 3

Theoretical consideration of X-ray refraction at an object and X-ray DFI

3.1 X-ray refraction at an object

When X-rays pass through an object, refraction of the beam occurs at the border that separates various media, and absorption takes place according to the absorption coefficients of their components. As soft tissues of biomedical objects have only slight differences in density values, they are barely distinguishable by absorption contrast images. It is therefore open to discussion whether X-ray images based on refraction can reveal soft tissue structures. It is well known that X-rays are also refracted according to Snell's Low. The deflection angle by X-ray refraction is determined as follows. Let us consider a flat boundary between two media

with different refractive indices n_1 and n_2 (Fig. 6). When an X-ray is incident on the flat boundary at an angle φ, it deviates $\Delta\varphi$ from its initial direction according to Snell's Low as follows:

$$\frac{\sin\varphi}{\sin(\varphi+\Delta\varphi)} = \frac{n_2}{n_1} \tag{4}$$

This equation is modified by Taylor's expansion [105] for the function $\sin\varphi/\sin(\varphi+\Delta\varphi)$ as follows:

$$\frac{\sin\varphi}{\sin\varphi+\cos\varphi\cdot\Delta\varphi} \cong \frac{n_2}{n_1} \tag{5}$$

Following manipulation of this equation, we have:

$$\Delta\varphi \cong \frac{n_1-n_2}{n_2}\tan\varphi \tag{6}$$

From Eq. (1), Eq. (6) finally takes the form:

$$\Delta\varphi \cong \frac{\Delta\delta}{n_2}\tan\varphi \tag{7}$$

Here, $\Delta\delta = n_1 - n_2 = \delta_2 - \delta_1$, where δ_1 and δ_2 are unit decrements of media n_1 and n_2, respectively. The deviation angle can become sufficiently large in the case of a circular boundary because of the large value of the possible incident angle. Let us suppose an elliptical boundary where X-rays are incident on the surface at angle φ (Fig. 7). In this case, X-rays are deviated once more when exiting the object. If the angle of incidence at the boundary on the opposite side is ψ, deflection angle $\Delta\psi$ is calculated as

follows:

$$\frac{\sin\psi}{\sin(\psi-\Delta\psi)}=\frac{n_1}{n_2} \tag{8}$$

$$\frac{\sin\psi}{\sin\psi-\cos\psi\cdot\Delta\psi}\cong\frac{n_1}{n_2} \tag{9}$$

$$\Delta\psi\cong\frac{n_1-n_2}{n_1}\tan\psi \tag{10}$$

$$\Delta\psi\cong\frac{\Delta\delta}{n_1}\tan\psi \tag{11}$$

After propagating through an elliptical object, the incident X-rays attain a total deflection angle of θ:

$$\theta\cong\Delta\varphi+\Delta\psi$$

$$=\frac{\Delta\delta\tan\varphi}{n_2}+\frac{\Delta\delta\tan\psi}{n_1}$$

$$=\frac{\Delta\delta}{n_1n_2}(n_1\tan\varphi+n_2\tan\psi) \tag{12}$$

To simplify the geometrical consideration, let us suppose a circular boundary, as shown in Fig. 8. Because of its symmetrical shape, ψ can be expressed as follows:

$$\psi=\varphi+\Delta\varphi \tag{13}$$

Therefore, θ can be calculated as a function of φ using the following equation:

$$\theta \cong \frac{\Delta\delta}{n_1 n_2}(n_1 \tan\varphi + n_2 \tan(\varphi + \frac{\Delta\delta}{n_2}\tan\varphi)) \quad (14)$$

To estimate θ, the δ of the two media that comprise a boundary are required; these values are calculated from their densities ρ and wavelength of the incident X-rays λ (see Eq. (3)). As an incident X-ray energy of approximately 35 keV was adopted in our experiments aimed for clinical use, we calculated the δ of representative tissues and that of water for this X-ray energy; the results are shown in Table 1 [31, 106]. We also calculated the φ values for the circular boundary around the point where the X-ray is tangentially incident; this is shown in Fig. 9. In this instance, the circular boundary was assumed to be the arc of a circle with a radius of 10 mm. φ tends to 90° close to the point where the X-ray beam is tangentially incident, and diminishes to 80° at the point of 150 μm from the tangentially incident point along the radius direction. Here, let us suppose a circular boundary of water and articular cartilage with a radius of 10 mm. Water is assumed as the synovial fluid within the articular capsule. The relationship between the incident angle φ of the 35 keV X-ray beam and the deviation angle θ for this case is shown in Fig. 10. The gradient of the curve increases sharply around a φ value of 86°. This angle of φ corresponds to a distance of 25 μm from the tangentially incident point along the radius direction.

3.2 X-ray DFI by Laue geometry

3.2.1 Bragg geometry or Laue geometry?

Angular resolving analyzer imaging from refraction at an object has been actively studied over the last 10 years. There are two types of analyzer arrangement: those that utilize Bragg geometry and those that utilize Laue geometry. The Bragg case analyzer was first developed by Chapman *et al.* in 1997 [12] using an analyzer of relatively large thickness; this method is termed diffraction enhanced imaging (DEI). The Laue case analyzer was developed by Ingal *et al.* in 1995 [6], using a thin analyzer. In 2001, Ando *et al.* modified Laue type analyzer imaging to enable the detection of weak signals related to refraction at an object, with almost no background illumination, by tuning the incident X-ray energy and thickness of the analyzer [21]. This technique is termed dark-field imaging (DFI). Hirano *et al.* then applied a thin Bragg case analyzer to DFI in 2002 [24].

The aim of the present study is the application of these imaging methods to clinical use; therefore, the choice of either Bragg or Laue geometry must be undertaken from the point of view which is more proper for imaging of patients. 2D single-shot imaging without line-scanning and/or image processing would be indispensable for this purpose. The

characteristic of this method will also enable us to observe an object dynamically under fluoroscopy. Laue geometry is more suitable for clinical use than Bragg geometry because it offers a larger field size for a given size of analyzer crystal. Figure 11 demonstrates that for Bragg geometry, the analyzer must be five-times larger than that required for Laue geometry to obtain the same field size. It is anticipated that larger 2D single-shot field sizes will be readily obtained by Laue geometry in the future; these will enable the imaging of larger objects.

3.2.2 Theory of X-ray DFI by Laue case

The combination of a monochro-collimator (MC) and a Laue case analyzer A(L), both of which are manufactured from perfect silicon crystal, is a key technological factor for 2D one-shot X-ray DFI. An MC enlarges the size of the incident X-ray beam and also improves its angular divergence. The cut surface is oriented at an appropriate angle α to the reflecting planes. An asymmetric factor b [107] is defined as $\sin(\theta_B - \alpha) / \sin(\theta_B + \alpha)$. Here, θ_B is the Bragg angle. The MC, with an asymmetric factor b, enlarges the incident beam $1/b$ times to the reflecting direction and improves its angular divergence by a factor of $b^{1/2}$. An A(L) works as a kind of angle-resolving filter for the incident X-ray, and has a thickness of several millimeters. I_O and I_G in the Laue case diffraction are defined as the

beam intensity in the directions of forward diffraction and diffraction, respectively. Considering negligible absorption for simplicity, these terms are defined as follows:

$$I_O = \frac{W^2 + \cos^2(\pi H\sqrt{W^2+1}/\Lambda)}{W^2+1} \tag{15}$$

$$I_G = \frac{\sin^2(\pi H\sqrt{W^2+1}/\Lambda)}{W^2+1} \tag{16}$$

$$\Lambda = \lambda\cos\theta_B / |P||\chi_G| \tag{17}$$

$$I_O + I_G = 1 \tag{18}$$

where H is A(L) thickness, and W is the normalized angular deviation from the center of the Bragg peak. Λ is the extinction distance as defined in Eq. (17), where λ is the X-ray wavelength, P the polarization factor, and χ_G the electric susceptibility.

Although Eqs. (15) and (16) are realized under the condition that there is no absorption by A(L), they are useful for observing the oscillations of peak intensities for I_O and I_G at $W = 0$. When $W = 0$, Eqs. (15) and (16) are expressed as follows:

$$I_O = \cos^2(\pi H/\Lambda) \tag{19}$$

$$I_G = \sin^2(\pi H/\Lambda) \tag{20}$$

Figures 12 and 13 show I_O for a particular X-ray energy in the

angular range of ± 4 about W for decreasing and increasing thickness of H (at 15 μm intervals), respectively, from the base thickness H to 60 μm. The curves of I_G are found by reversing the corresponding curve of I_O, which is clear from the Eq. (18). The key manipulation for X-ray DFI is to make the reflectivity of I_O at $W = 0$ approximately equal to 0. This condition can be easily realized by increasing the incident X-ray energy (see Fig. 12) or by inclining A(L) to increase its effective thickness (see Fig. 13). In practice, the inclination of A(L) is limited to about 15°, which corresponds to up to approximately 35 μm correction of effective thickness for a 1-mm-thick A(L). Figure 14 shows the relationship between the inclination angle and effective thickness. The curve 'e' in Fig. 12 and 13 is desirable to realize the X-ray DFI. I_O outside $|W| = 1$ maintains a high reflection percentage, while I_O inside $|W| = 1$ is low, and is close to 0 at $|W| = 0$. One can easily observe that X-rays refracted by $|W| > 1$ at an object will have a high reflectivity of I_O, while those with $|W| < 1$, or non-refracted X-rays, show low reflectivity if the imaging is performed with A(L) set at exactly the Bragg angular position, that is, $|W| = 0$. As a result, X-rays refracted by larger than $|W| = 1$ will be highly contrasted with non-refracted X-rays in the forward diffracted X-ray direction. Accordingly, $I_O = 0$ at $|W| = 0$ realizes X-ray DFI, which is formed solely out of X-rays refracted at the object, with a low level of background illumination that is derived from X-rays non-refracted at the object.

The steps involved in acquiring X-ray DFI are as follows:

Ⅰ.Tune the effective thickness of A(L) and incident X-ray energy, and fix the A(L) to the Bragg condition.

Ⅱ. Close the shutter and position an object in front of the A(L).

Ⅲ. Open the shutter and detect the forward diffracted X-rays.

The top view of this process is illustrated in Fig. 15. The different gray levels on the object indicate the different X-ray refractive indices for each of the four areas. Note that true X-ray DFI is composed only of X-rays refracted at an object.

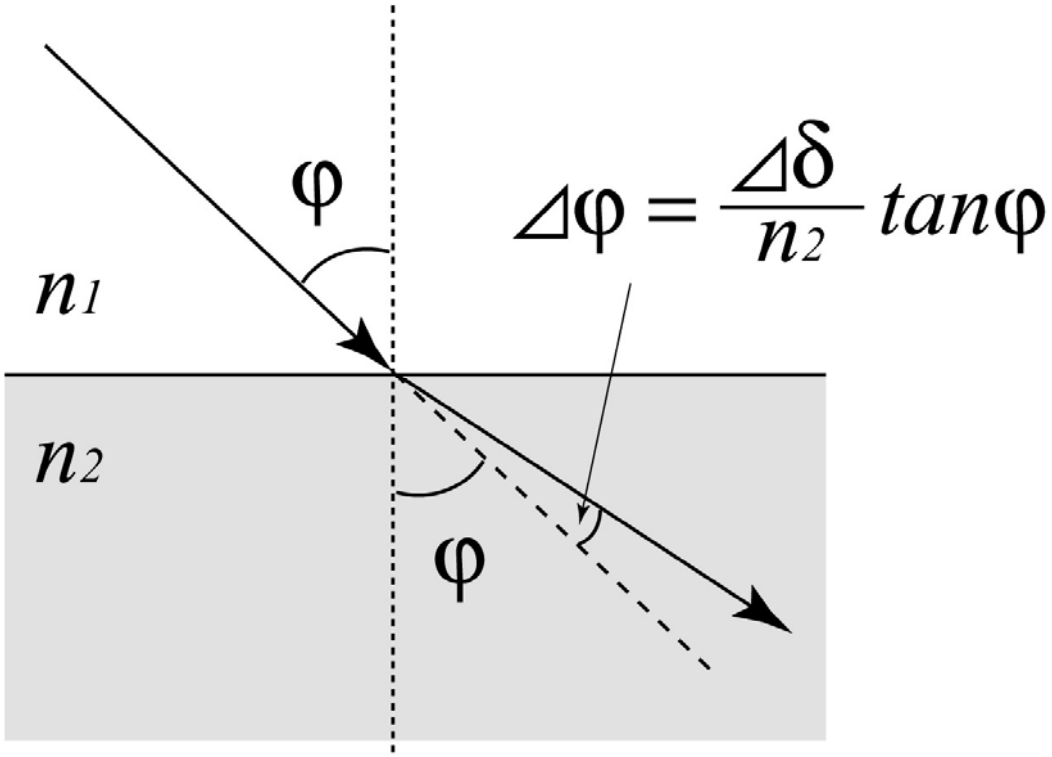

Figure 6. Refraction of X-rays at a flat boundary between media with refractive indices n_1 and n_2.

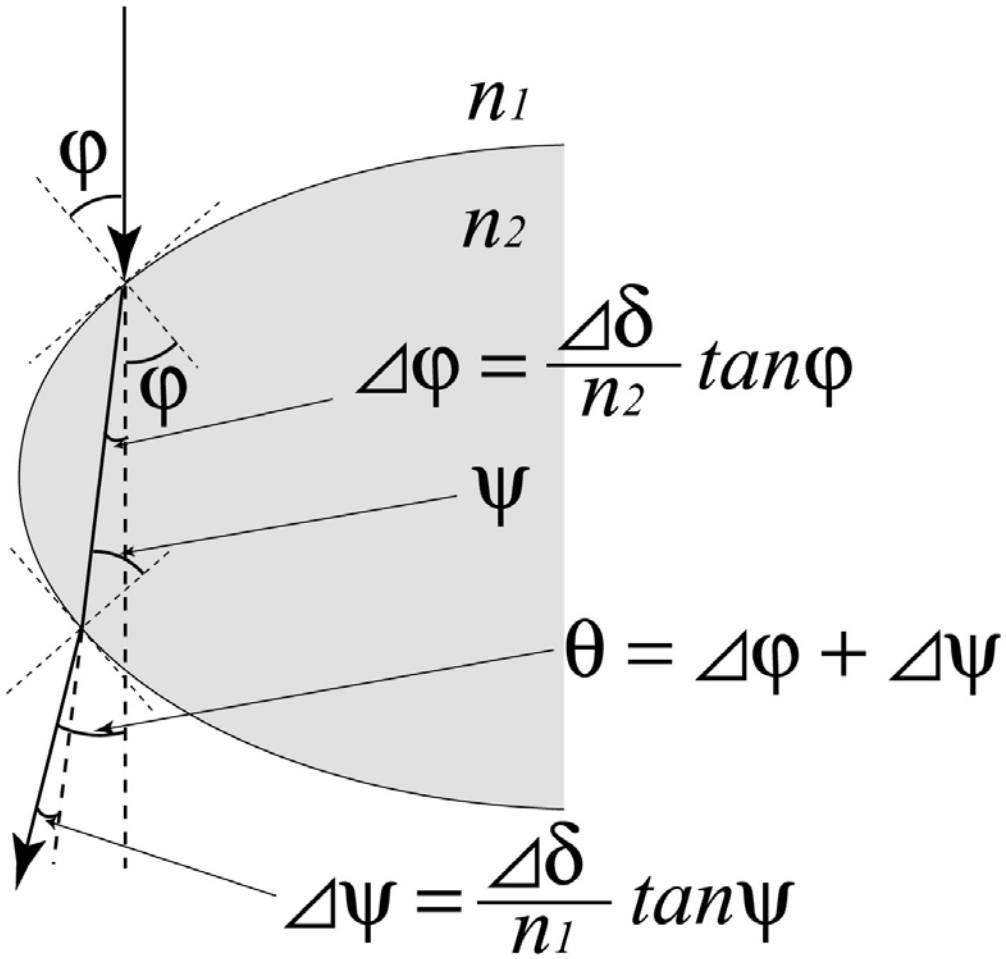

Figure 7. Refraction of X-rays at an elliptical boundary between media with refractive indices n_1 and n_2.

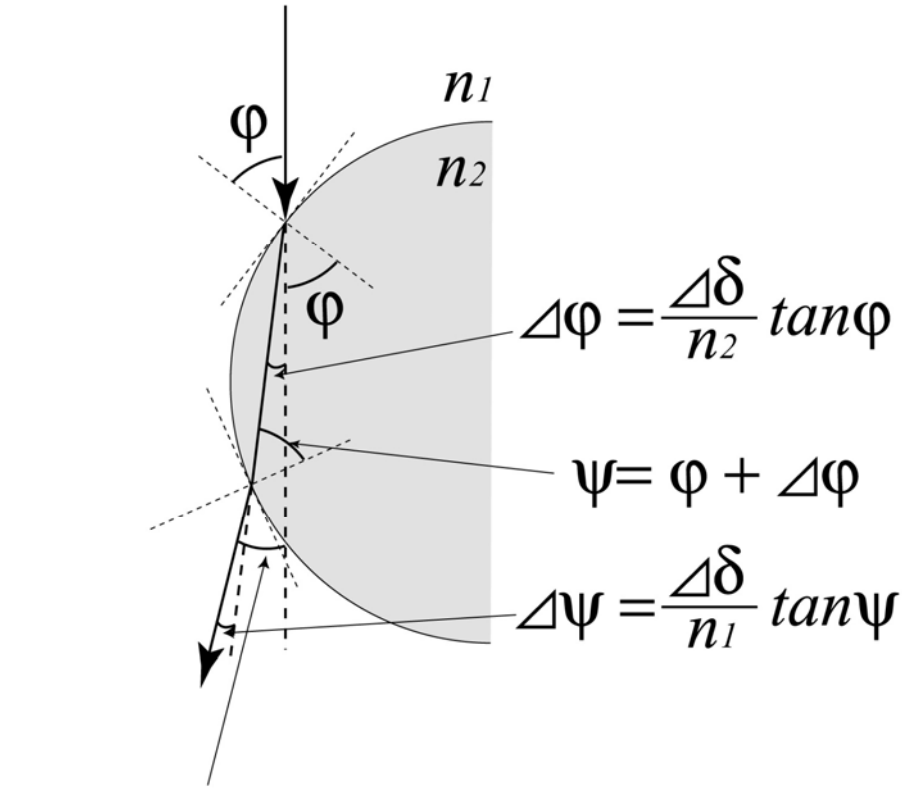

$$\theta = \Delta\varphi + \Delta\psi$$

$$= \frac{\Delta\delta}{n_1 n_2} (n_1 tan\varphi + n_2 tan(\varphi + \Delta\delta / n_2 tan\varphi))$$

Figure 8. Refraction of X-rays at a circular boundary between media with refractive indices n_1 and n_2.

Tissue	ρ**[kg/m^3]**	δ
Skin	1090	1.84×10^{-7}
Adipose tissue	950	1.61×10^{-7}
Articular cartilage	1100	1.86×10^{-7}
Muscle skeletal	1050	1.78×10^{-7}
Breast (Mammary gland)	1020	1.73×10^{-7}
Kidney	1050	1.78×10^{-7}
Liver	1060	1.79×10^{-7}
Lung(Deflated)	1050	1.78×10^{-7}
Lung(Inflated)	260	0.44×10^{-7}
Cortical bone	1920	3.25×10^{-7}
Spongiosa	1180	2.00×10^{-7}
Water	1000	1.69×10^{-7}

Table 1. ρ and δ values of representative tissues and water for 35 keV X-rays.

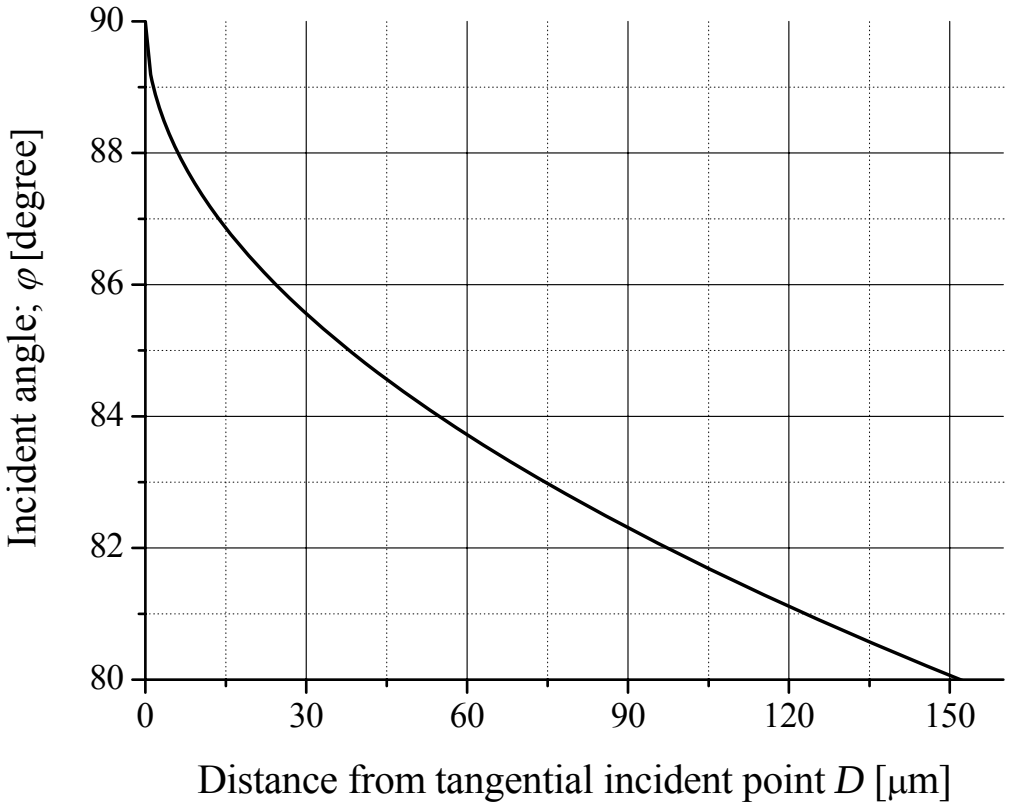

Figure 9. Values of φ for the circular boundary around the point where X-rays are tangentially incident.

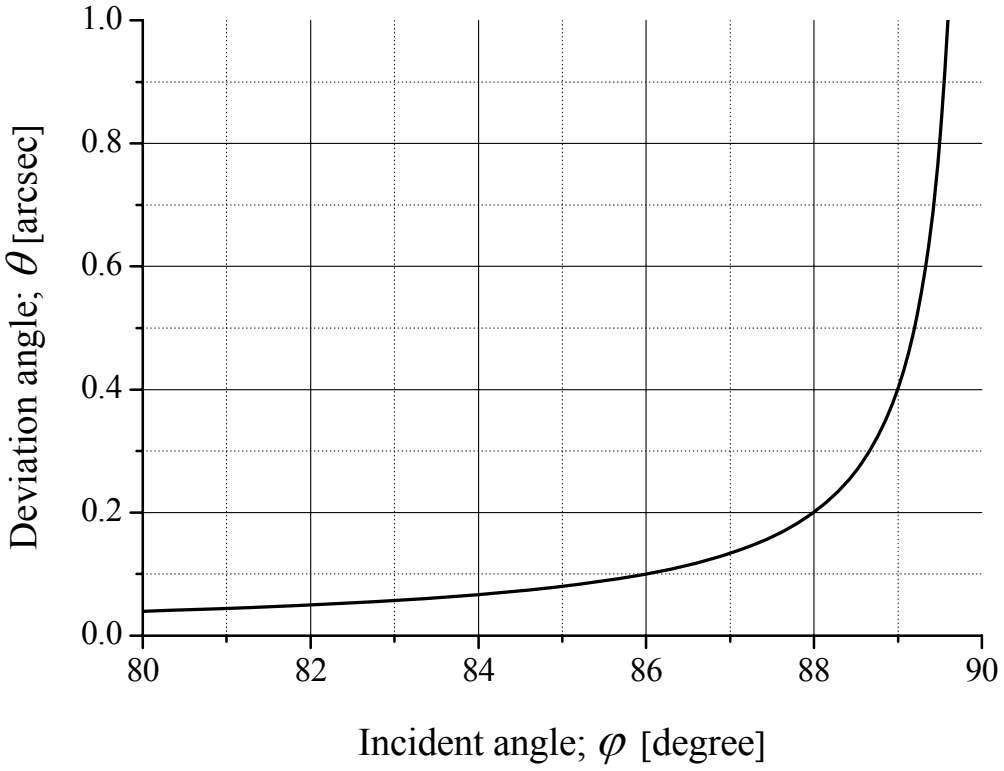

Figure 10. Relationship between incident angle φ of 35 keV X-rays and deviation angle θ for the boundary between synovial fluid and articular cartilage.

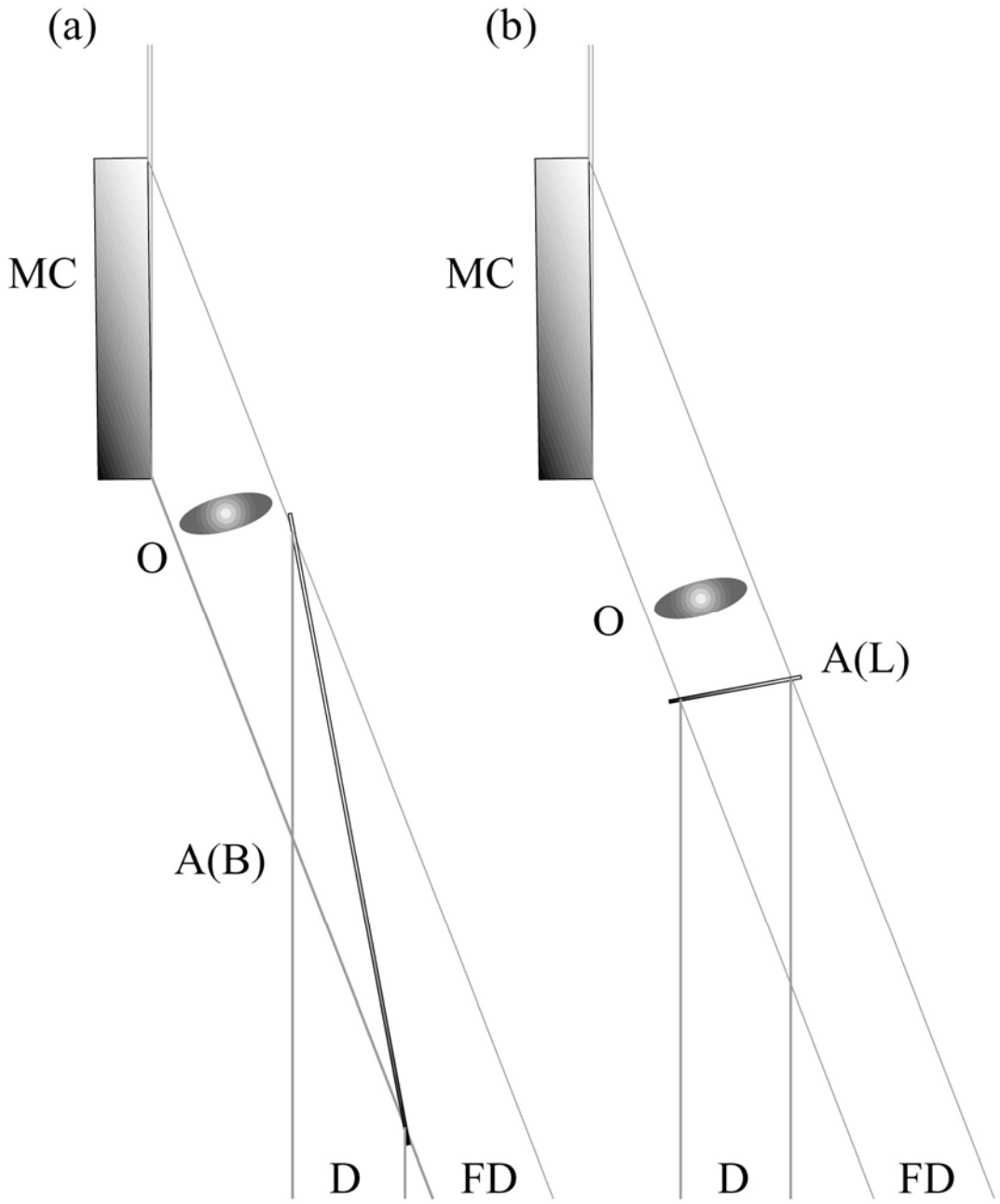

Figure 11. Comparison of Bragg geometry (a) and Laue geometry (b) in obtaining an equivalent field of view. MC: monochro-collimator, O: object, A(B): Bragg case analyzer, A(L): Laue case analyzer, D: diffracted X-rays, and FD: forward diffracted X-rays.

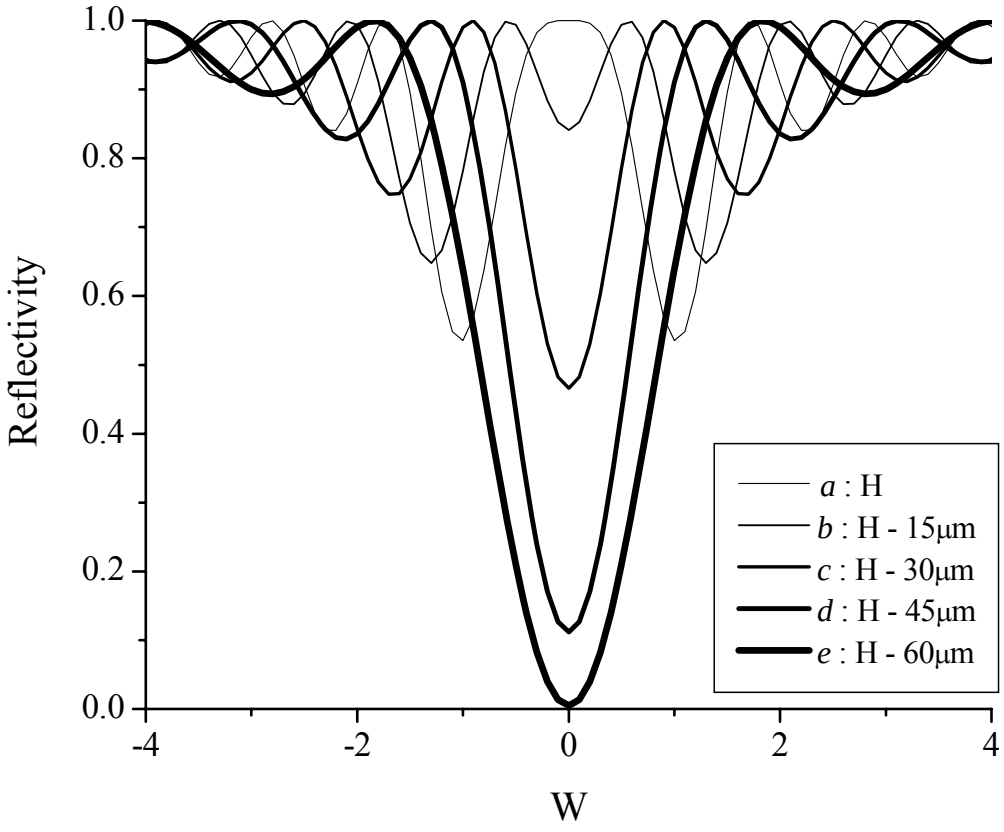

Figure.12. Analyzer thickness H dependency of I_O with H decreased by 15 μm to 60 μm when the incident X-ray energy is fixed.

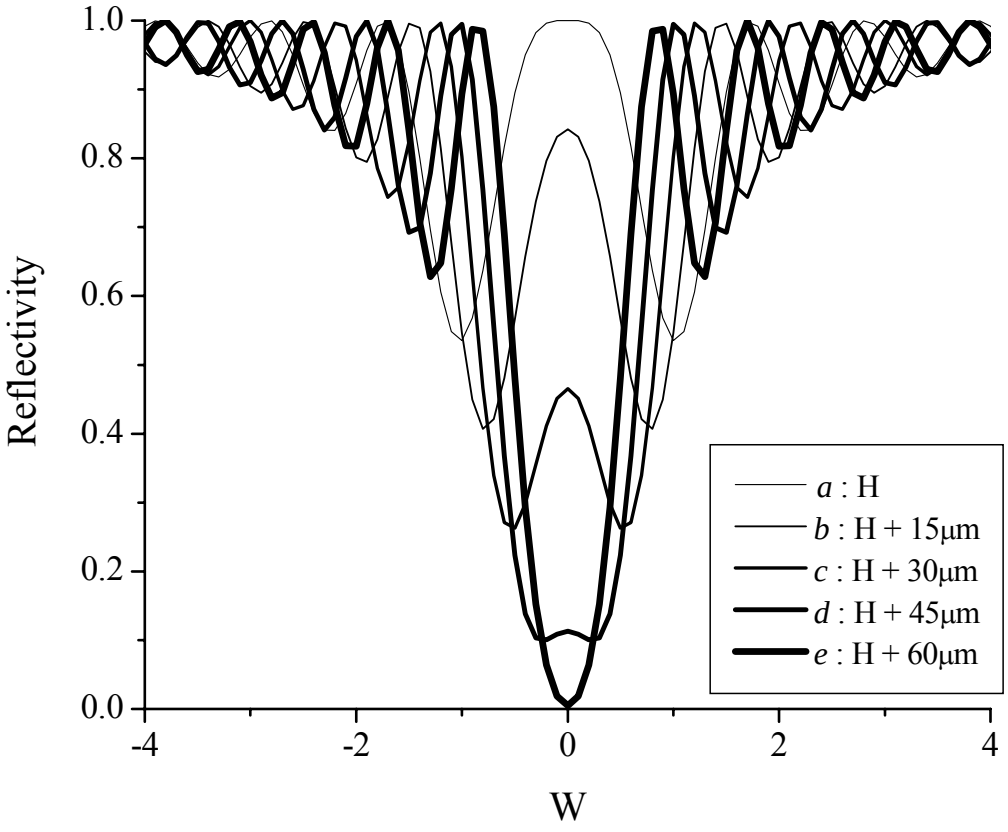

Figure 13. Analyzer thickness H dependency of I_O with H increased by 15 μm to 60 μm when the incident X-ray energy is fixed.

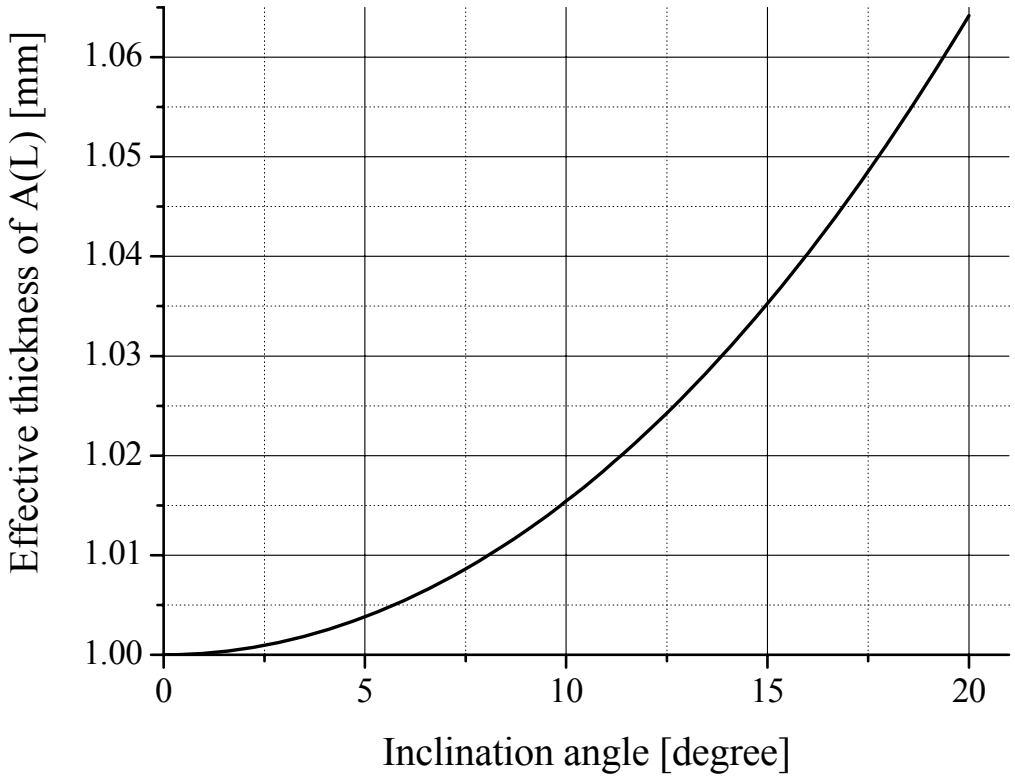

Figure 14. Relationship between inclination angle and effective thickness of 1-mm-thick Laue case analyzer.

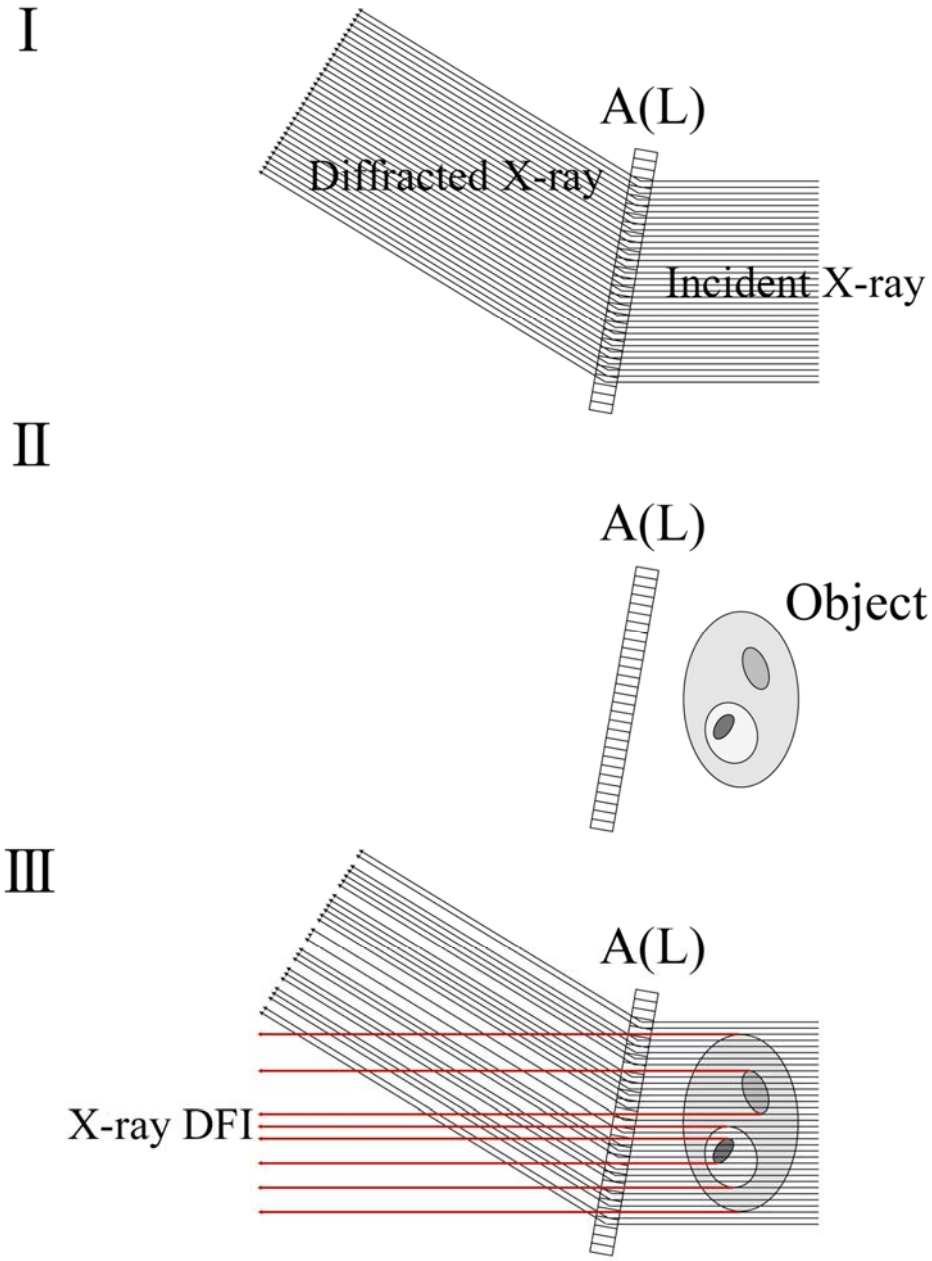

Figure 15. Steps involved in acquiring X-ray DFI.

Chapter 4

Experiment of X-ray DFI for articular cartilage towards clinical application

4.1 Design of experimental setup

An incident X-ray energy of around 35 keV was selected for this experiment to reduce the exposure dose towards clinical use. Note that the incident X-ray energy must be tuned within the range of 2 keV to realize X-ray DFI. The MC and A(L) were both manufactured from perfect silicon crystal. Mechano-chemical polishing was carried out for the MC but not the A(L). Mechano-chemical polishing of the A(L) is desirable to obtain background homogeneity, but is difficult to achieve because the thin wafer is on the base, which was cut monolithically. The photographs of the MC

and A(L) are shown in Figs. 16 and 17, respectively. The selected diffracting planes of the MC and A(L) are Si(440), as the width of the rocking curve under this condition is considered to be a suitable for the refraction angle at soft tissue. The surface of the MC (size 45 mm (V) by 120 mm (H)) was cut at $\alpha = 9.9°$ from the Si (440) diffracting planes. The size of the A(L) was 40 mm (V) by 70 mm (H), and approximately 1.2 mm thick. Under this condition, the incident X-rays are expanded to approximately 40 mm horizontally, and the vertical length is the same as that of the incident X-rays. The experimental setup design is shown in Fig. 18, where a human finger was positioned between the MC and A(L) as an object.

4.2 Simulation of rocking curves for the designed setup to realize X-ray DFI

Absorption of X-rays by the A(L) cannot be disregarded for the case of a prepared A(L) with a thickness of approximately 1.2 mm and incident X-ray energy of around 35 keV. In simulating the rocking curve of forward diffraction and diffraction, X-ray absorption must therefore be taken into account.

The intensities of the forward diffracted and diffracted X-rays for a

Laue case crystal of thickness H, when taking account of absorption, are explained in detail for example in refs. [108] and [109]. According to ref. [109], the intensities are summarized roughly as follows. The forward diffracted and diffracted intensities for σ-polarization $I_O(W,H)$ and $I_G(W,H)$, expressed as functions of W and H, are given by:

$$I_O(W,H) = \frac{\gamma_G}{\gamma_O} \left| D_O(z=H) \right|^2 \tag{21}$$

$$I_G(W,H) = \frac{\gamma_G}{\gamma_O} \left| D_G(z=H) \right|^2 \tag{22}$$

Here, $D_O\ (z = H)$ and $D_G\ (z = H)$ are the amplitudes of the forward diffracted and diffracted X-rays, respectively, and are given by:

$$D_O(z=H) = \frac{1}{\xi^{(1)} - \xi^{(2)}} \left[\xi^{(2)} \exp\left(2\pi i \delta k_z^{(1)} H\right) - \xi^{(1)} \exp\left(2\pi i \delta k_z^{(2)} H\right) \right] \tag{23}$$

$$D_G(z=H) = \frac{\xi^{(1)}\xi^{(2)}}{\xi^{(2)} - \xi^{(1)}} \left[\exp\left(2\pi i \delta k_z^{(1)} H\right) - \exp\left(2\pi i \delta k_z^{(2)} H\right) \right] \tag{24}$$

$\delta k_z^{(j)}$ and $\xi^{(j)}$ can be written as

$$\delta k_z^{j} = -\frac{K\left|\chi_G^{'}\right|}{2\sqrt{\gamma_G \gamma_O}} \left[(W+ig) \pm \sqrt{(W+ig)^2 + (1+ik)^2} \right] - \frac{iK\chi_O^{''}}{2\gamma_O} \tag{25}$$

$$\xi^{(j)} = -\frac{1}{1+ik} \sqrt{\frac{\gamma_O}{\gamma_G}} \left[(W+ig) \pm \sqrt{(W+ig)^2 + (1+ik)^2} \right] \tag{26}$$

where K is the wave number of the incident X-ray in the vacuum and γ_O and γ_G are scalar products of the incident wave unit vector and diffracted wave unit vector with the inner surface normal unit vector, respectively. In

Eqs. (25) and (26), W ,g and k are given by

$$W = \frac{1}{2\left|\chi_G^{'}\right|}\sqrt{\frac{\gamma_O}{\gamma_G}}\left[2(\theta_0 - \theta_B)\sin(2\theta_B) + \chi_O^{'}\left(1 - \frac{\gamma_G}{\gamma_O}\right)\right] \tag{27}$$

$$g = \frac{\chi_O^{''}}{2\left|\chi_G^{'}\right|}\left(\sqrt{\frac{\gamma_O}{\gamma_G}} - \sqrt{\frac{\gamma_G}{\gamma_O}}\right) \tag{28}$$

$$k = \frac{\chi_G^{''}}{\left|\chi_G^{'}\right|} \tag{29}$$

θ_0 is the angle of incidence in the Laue case. $\chi_O^{'}$, $\chi_O^{''}$ and $\chi_G^{'}$, $\chi_G^{''}$ are the real and imaginary components of the electric susceptibility χ_O and χ_G for the forward diffracted and diffracted beams, respectively.

To understand the change in the shapes of the rocking curves, the curves were simulated under the following conditions: the thickness of the A(L) was incrementally varied by a minute amount, while the incident X-ray energy remained constant at 35 keV. XOP 2.1 Beta 3 (X-ray Oriented Programs), which is provided freely by the European Synchrotron Radiation Facility (ESRF), was utilized in the simulation. The results are shown in Figs. 19 (a)-(e).

The results demonstrate that the reflectivity of forward diffracted X-rays at 0 arcsec (deviation from the Bragg angle) shows a period of approximately 120 μm. The condition of Fig. 19 (c) is therefore ideal for X-ray DFI. If the initial shape of the rocking curve approximates that shown in Fig. 19 (b), it is possible to realize the ideal shape for X-ray DFI

by adjusting the effective thickness of A(L). If the initial shape of the rocking curve is close to that shown in Fig. 19 (d), however, the incident X-ray energy has to be tuned to slightly higher. Note that the tuning range for the incident X-ray energy is limited to a few keV because the angle from the diffracting plane of MC, α, is fixed.

4.3 Object and consideration of the best setting of the object to visualize articular cartilage

The object is a human finger amputated from a cadaver at metacarpophalangeal joint (MP joint) and fixed by formalin. Coloured volume-rendered 3D X-ray CT images displayed with various object opacities are shown in Fig. 20. These images were acquired using a conventional X-ray CT device for clinical use (HITACHI MEDICO). The target area is the articular cartilage on the head of the proximal phalanx. To investigate the structure of the proximal interphalangeal joint (PIP joint), volume-rendered 3D X-ray CT images of bones viewed from various angles were acquired using the same 3D CT date set as those in Fig. 20; these are shown in Fig. 21. There are two condyles on the head of the proximal phalanx: the lateral condyle and the medial condyle. Both are covered with articular cartilage. When projection images are observed, the

articular cartilages of both condyle cannot be visualized simultaneously, and they must be selected individually as the target. Slight pronation of the upper limb with slight flexion of the PIP joint is the best position for revealing the articular cartilage on the medial condyle of the proximal phalanx.

4.4 Experiment of X-ray DFI for visualization of articular cartilage

4.4.1 Preliminary experiment of PIP joint imaging by X-ray DFI at Photon Factory BL14B

The preliminary experiment for X-ray DFI, with the aim of imaging articular cartilage, was performed at beamline BL14B. This experiment utilized vertical polarization synchrotron radiation from the 5 Tesla superconducting wave shifter of the Photon Factory, which is in operation with 2.5 GeV and 450 mA, with a lifetime of 3000 min. A Si(111) double crystal monochromator is installed in this beamline and utilized for 10-20 keV X-rays by Si(111), 30-60 keV by Si(333), and 40-80 keV by Si(444) diffracting planes. The incident X-rays were monochromated to 34.8 keV, and a beam size of approximately 15 mm (V) and 3mm (H) was acquired.

The experimental apparatus was the same as that shown in Fig. 18, and the setup is shown in Fig. 22. Once incident X-ray energy was fixed to 34.8 keV, *b* was calculated to 0.04. This condition magnifies the beam size 25-times horizontally and improves its angular divergence by a factor of 0.2 by MC. As a result, the acquired field size was 15 mm (V) and 40 mm (H). For this combination of prepared MC and A(L), an incident X-ray energy of 34.8 keV with 5° inclination of A(L) represents optimum conditions for X-ray DFI. The rocking curves of forward diffraction and diffraction by A(L) without an object were then measured, and representative ones are shown in Fig. 23. The Object was set 200 mm in front of the A(L) in air. DFI and subordinate Bright-Field Image (BFI) on the diffracted X-ray were taken under the just Bragg condition. In addition, pseudo-DFIs and subordinate BFIs were acquired with the A(L) set off the just Bragg condition by approximately 0.05 arcsec to either a higher or lower angular position. The absorption contrast image was also taken with the analyzer set at 5 arcsec lower than the just Bragg condition. All of the images were stored on mammography film (Kodak Min-R 2000) without an intensifying screen to acquire images with high spatial resolution. The exposure time was 90 sec at a ring current of approximately 400 mA.

4.4.2 Further detailed experiment of PIP joint imaging by X-ray DFI at Photon Factory BL14C1

A subsequent, more detailed, experiment with the aim of imaging articular cartilage using X-ray DFI was performed at beamline BL14C1 based on the result of the preliminary experiment **4.4.1**. This beamline is branched off from the same trunk of BL14B. A Si(220) double crystal monochromator is installed in this beamline to utilize 12-66 keV X-rays. The experimental setup was identical to that of **4.4.1**. In this beamline, incident X-rays of 34.8 keV are extracted more stably and with a larger photon flax density than those of BL14B, as fundamental harmonic reflection can be utilized. Additionally, the vertical dimension of the incident X-rays is approximately 30 mm, providing a field size of 30 mm (V) and 40 mm (H). The rocking curves of forward diffraction and diffraction by A(L) without an object were measured and representative ones are shown in Fig. 24.

The results of **4.4.1** reveal that articular cartilage unable to be depicted by X-ray absorption contrast imaging is clearly visualized by X-ray DFI and pseudo-DFIs. To avoid the observed effect of skin wrinkles superimposed over the articular cartilage, which may lead to incorrect diagnosis, the object was immersed in water. From another point of view, there was a strong dependency on the angular position of the A(L) in terms of the appearance of articular cartilage. Thorough research was performed

by taking images with the A(L) offset from the just Bragg condition by 0.04, 0.08, and 0.10 arcsec at both higher and lower angular positions, as well as at the just Bragg condition. Subordinate BFIs on the diffracted X-rays were taken for comparison at the same time. Absorption contrast images were also taken with the analyzer set 5 arcsec lower than the just Bragg condition. The points of the offset angles of the A(L) are shown in Fig. 25. The rocking curve of forward diffraction under these experimental conditions was simulated by the Eq. (30) (see ref. 110). The intensity: $\bar{I}$ is expressed as follows:

$$\bar{I} = \frac{1}{4}\left(1+\frac{W}{\sqrt{W^2+1}}\right)^2 \exp\left\{-\frac{\mu H}{\cos\theta_B}\left(1-\frac{\chi_G''/\chi_O''}{\sqrt{W^2+1}}\right)\right\} + \frac{1}{4}\left(1-\frac{W}{\sqrt{W^2+1}}\right)^2 \exp\left\{-\frac{\mu H}{\cos\theta_B}\left(1+\frac{\chi_G''/\chi_O''}{\sqrt{W^2+1}}\right)\right\} \quad (30)$$

In this equation, the oscillations were averaged over each period because their periods were extremely short. This suits the detectable rocking curve experimentally because of the low precision of detector. All of the images were stored on mammography film (Kodak Min-R 2000) without an intensifying screen to acquire images with high spatial resolution. The exposure time was 90 sec at a ring current of approximately 400 mA. To reveal this dependency, the divergences of X-rays through the soft tissues alone, as well as for both soft tissues and bone, were studied. The method involved measurement of the rocking curves of a 5 mm square X-ray beam

that was transmitted through both only the soft tissues and both soft tissues and bone.

4.4.3 Experiment for the clinical application of X-ray DFI at Photon Factory BL14B

Based on the results of the previous two experiment (**4.4.1** and **4.4.2**), experiments were then performed on exposure dose and depiction ability for a lesion, with a view towards clinical application.

4.4.3.1 Dosimetry in X-ray DFI

The dose evaluation for a clinical radiograph is usually performed by measuring the entrance surface dose for the skin, D_0 [Gy], which is expressed as follows [111]:

$$D_0 = X_{air} \cdot \frac{W}{e} \cdot f \cdot B \cdot \left(\frac{SCD}{SSD} \right)^2 \tag{31}$$

X_{air} : exposure [C/Kg]

W : mean energy to form an ion pair [J]

e : elementary charge [C]

f : ratio of $(\mu en/\rho)_{med}$ to $(\mu en/\rho)_{air}$

B : back scatter coefficient

SCD : source-chamber distance [m]

SSD : source-surface distance [m]

X_{air} is a value measured by the setting shown in Fig. 26, using an ion chamber. The international standard value of 33.97 J/C is used for *W/e*. f is dependent on both material and X-ray energy and is calculated as follows:

$$\frac{(\mu en/\rho)_{med}}{(\mu en/\rho)_{air}} \tag{32}$$

$(\mu en/\rho)_{med}$: mass energy absorption coefficient of a certain medium

$(\mu en/\rho)_{air}$: mass energy absorption coefficient of the air

For example, $(\mu en/\rho)_{med}$ for skin is 8.69×10^{-3} and $(\mu en/\rho)_{air}$ is 9.01×10^{-3} at X-ray energy of 36 keV. f is then calculated to be 0.964. B is dependent on both X-ray energy and the irradiated field size. B is approximately 1.16 at the effective X-ray energy of 36 keV from the X-ray tube for a circular field with a diameter of 32 mm, which is a similar condition to the present experiment [112, 113]. For reference, we generally use 45 kVp X-rays obtained form an X-ray tube and field size of 2×4 cm^2 clinically, under which condition B is 1.13. The difference in B for these varied calculations is only 2.6 %. The last element in Eq. (30), $(SCD/SSD)^2$, corresponds to the inverse square low of distance. If SCD is equal to SSD, this element becomes 1; if the X-ray beam is almost parallel, it is considered to be almost 1. From the calculations above, we can conclude that we have only

to compare the air absorbed dose D_{air} [Gy],

$$D_{air} = \left(\frac{W}{e}\right) \cdot X_{air} \tag{33}$$

of X-ray DFI and conventional clinical imaging to obtain a rough estimation of the required dose. From the above discussion, D_{air} represents the entrance surface dose of the air regardless of the backscatter factor.

For dose estimation, D_{air} was measured by a 6 cm^3 ion chamber, 10X5-6 with a model 9015 monitor (Radcal Corporation) shown in Fig. 27, in each following imaging condition.

4.4.3.2 Imaging of normal PIP and PIP with lesion by non screen and film/screen system

The ability of X-ray DFI to detect lesions of articular cartilage was tested using a different imaging object that contained small lesions on its articular cartilage. An intensifying screen (Kodak Min-R 2000 screen) was introduced to the imaging system to reduce the radiation dose. The spatial resolution of the film/screen system (Kodak Min-R 2000/ Kodak Min-R 2000 screen) was estimated 80 - 90 μm. This system was used to determine whether the ability to depict articular cartilage can be maintained with the introduction of an intensifying screen.

These experiments were performed at beamline BL14B at operating mode with 3 GeV and 200 mA. The experimental apparatus was identical

to that of the previous two experiments, but employed an incident X-ray energy of 36 keV. A slight adjustment of X-ray energy was necessary to obtain a sufficient enlargement rate; this may have resulted from the change in operation mode. *b* was then calculated to be 0.02. In this case, 15° inclination of the A(L) was the optimum condition for X-ray DFI. The representative measured rocking curves of forward diffraction and diffraction by A(L) without an object were shown in Fig. 28. The imaging was performed with the A(L) offset the just Bragg condition by 0.04, 0.08, and 0.12 arcsec to either a higher or lower angular position, in addition to the just Bragg condition. The points of the offset angles of the A(L) are shown in Fig. 29, as in Fig. 25. Subordinate BFIs on the diffracted X-ray were taken at the same time to enable a comparison. Absorption contrast images were also taken with the analyzer set 5 arcsec lower than the just Bragg condition. All of the images were stored on mammography film (Kodak Min-R 2000) with and without an intensifying screen (Kodak Min-R 2000 screen). The exposure times were 150 sec for non-screen imaging and 3 sec for imaging incorporating an intensifying screen at a ring current of approximately 190 mA.

4.4.4 Estimation of spatial resolution for X-ray DFI

A conventional phantom dedicated to absorption contrast images,

such as a rectangle chart with line pairs made of lead, is unsuitable for quantifying spatial resolution in X-ray DFI because image contrast is provided in this case by X-rays refracted at the object. A phantom that is detectable only by refraction contrast is required to measure spatial resolution for X-DFI, however, such a phantom does not exist. There is a need to define the spatial resolution for refraction contrast originally and also to develop the phantom to measure the spatial resolution.

To achieve this, a phantom was made from acryl plate. An optical photograph and photomicrograph of the phantom are shown in Figs. 30 and 31, respectively. Two lines, both with a width of approximately 60-80 μm, are scratched on the surface to intersect at a point. The minimum gap between the two lines is approximately 10 μm, and the gap widens in proportion to the distance from the crossing point. The spatial resolution for X-ray DFI is defined as the minimum gap that can be depicted by X-ray DFI. Note that absorption contrast imaging is unable to detect the two scratched lines.

The experiment was performed at beamline BL14B at operating mode with 2.5 GeV and 450 mA. The experimental apparatus was the same as that for **4.4.3**. Imaging was performed with the A(L) at the just Bragg condition. X-ray DFI and subordinate BFI were stored on mammography film (Kodak Min-R 2000) without an intensifying screen. Exposure times were 70 sec at a ring current of about 400 mA.

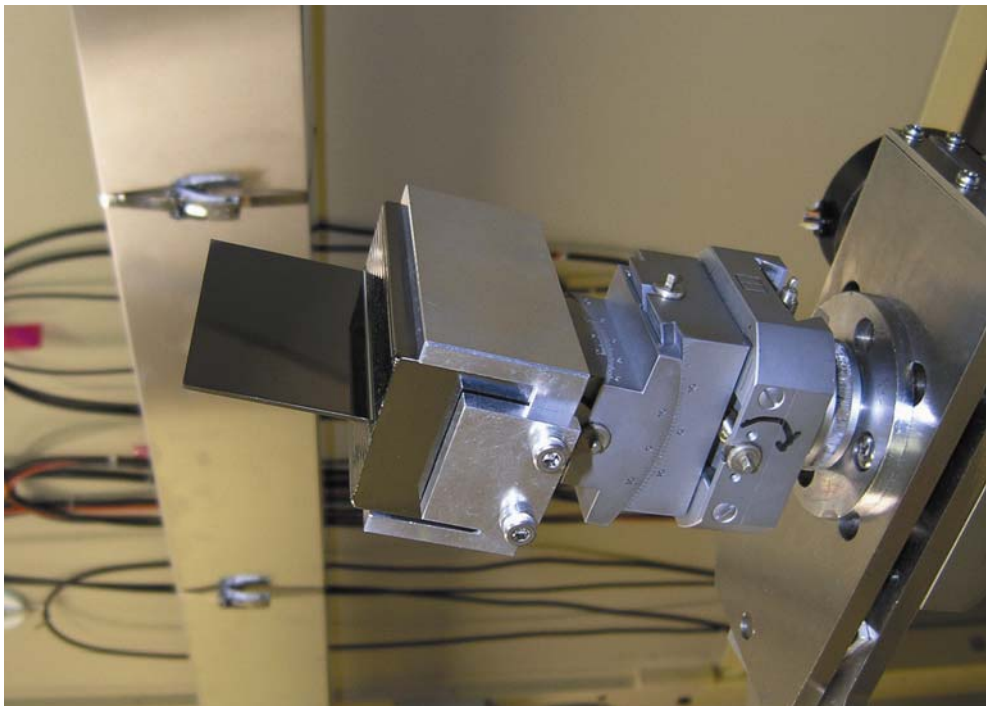

Figure 17. Photograph of A(L).

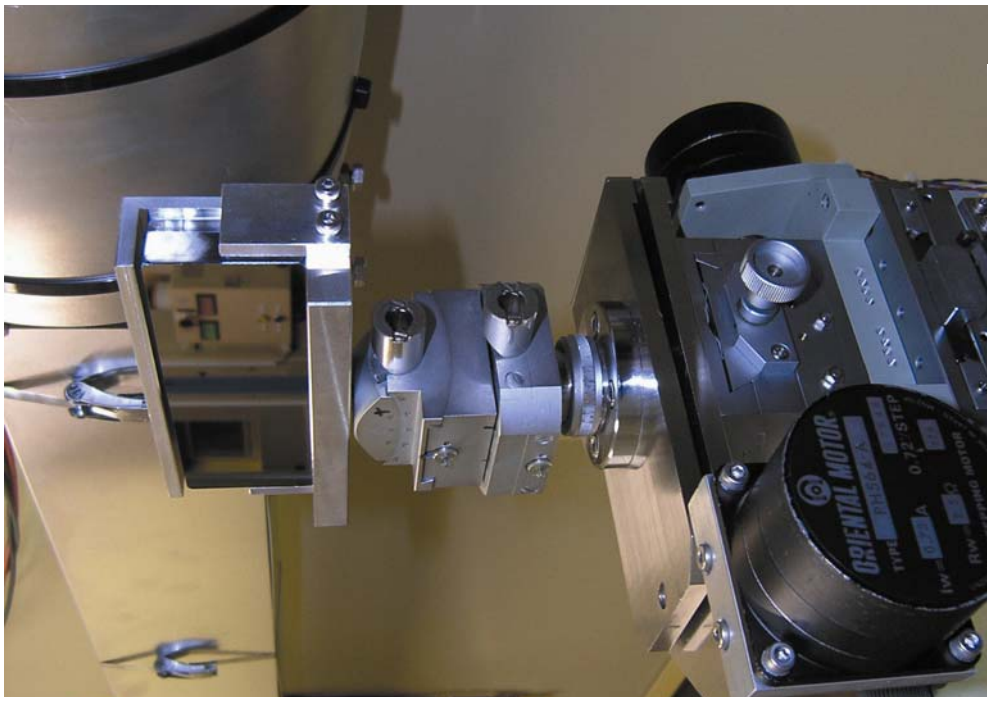

Figure 16. Photograph of MC.

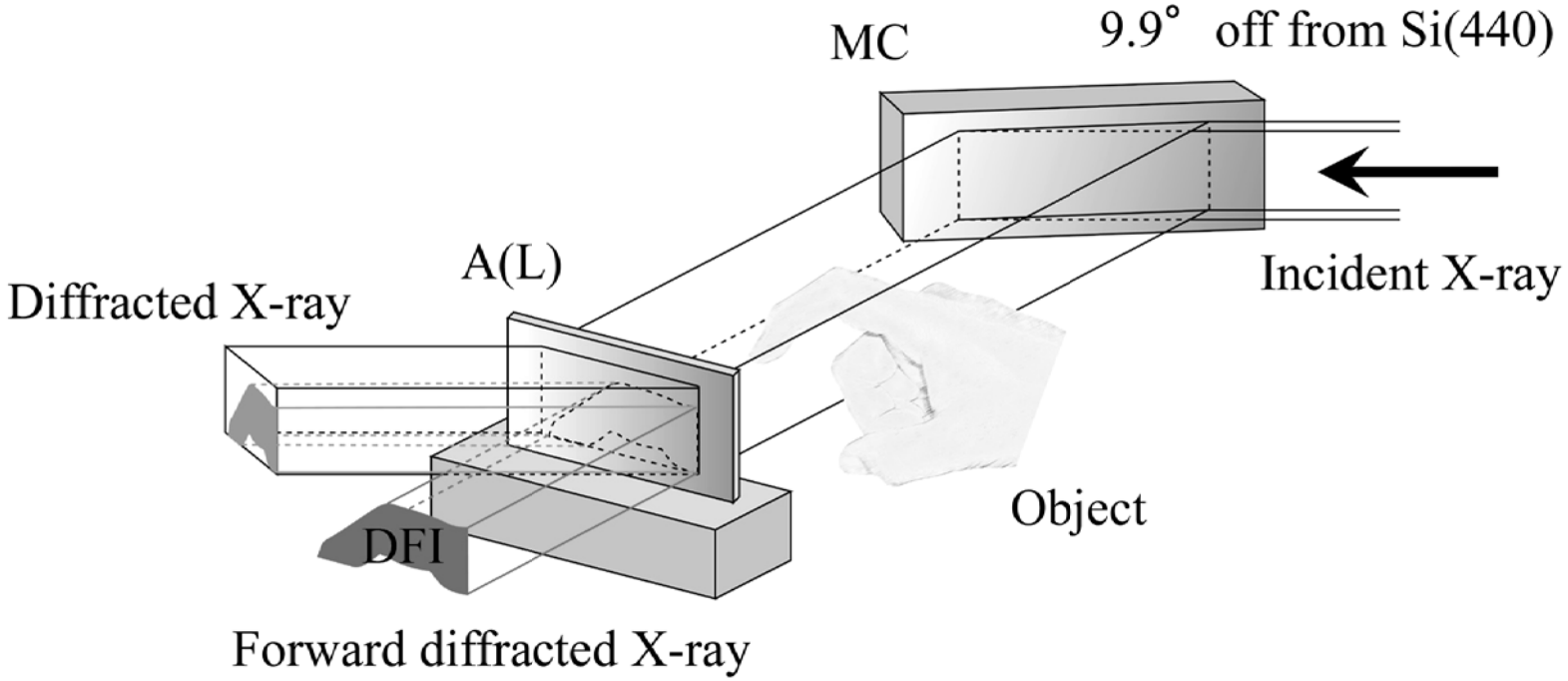

Figure 18. Experimental setup design for 2D single-shot X-ray DFI.

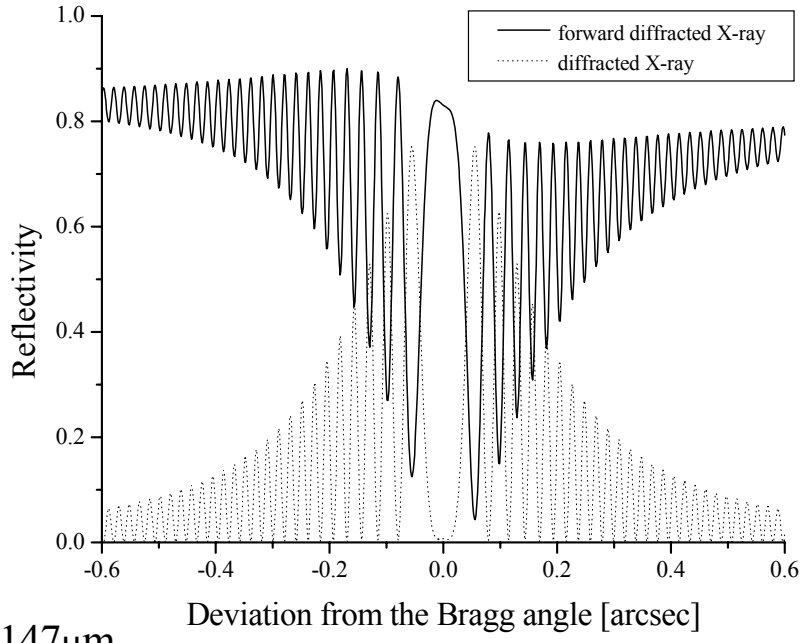

(a) 1147μm

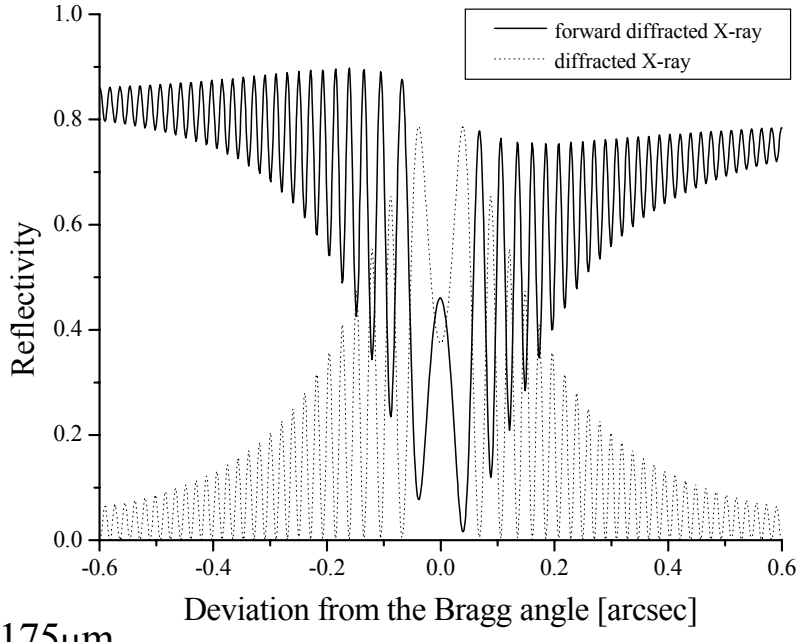

(b) 1175μm

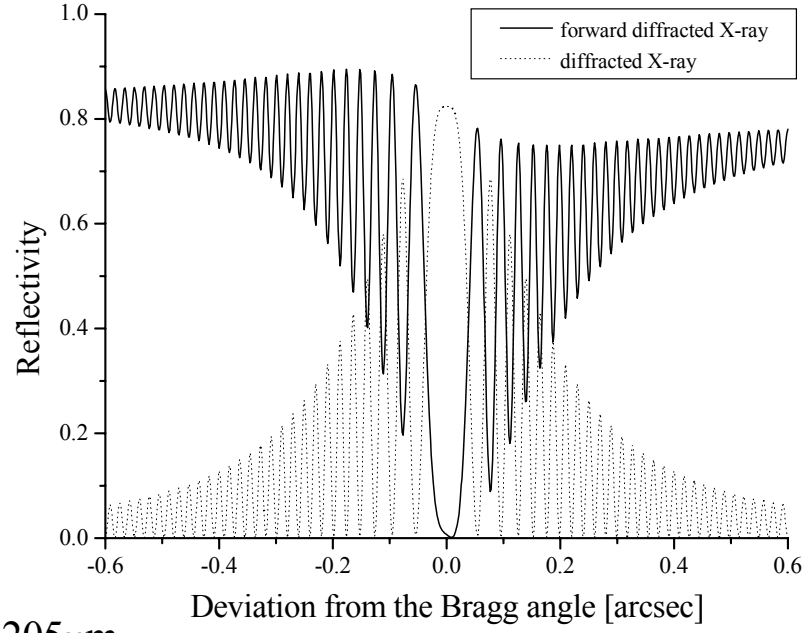

(c) 1205μm

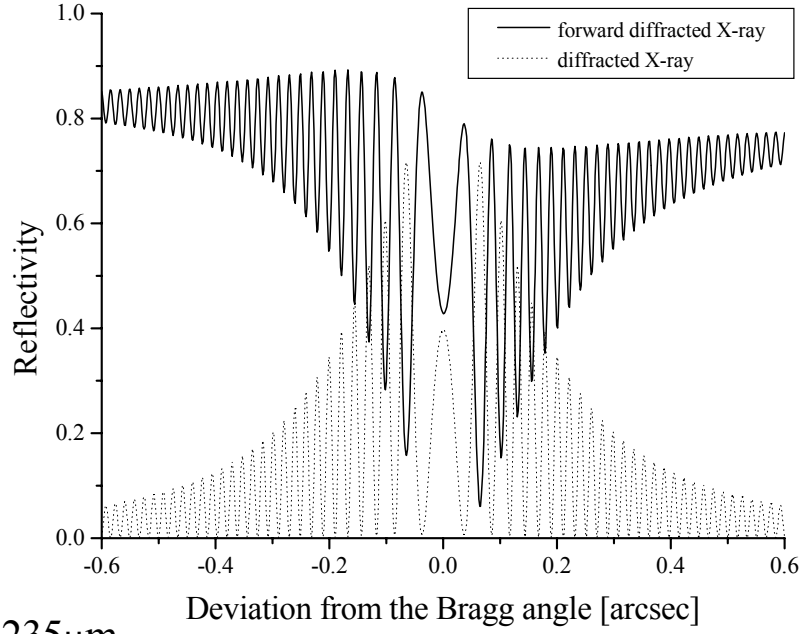

(d) 1235μm

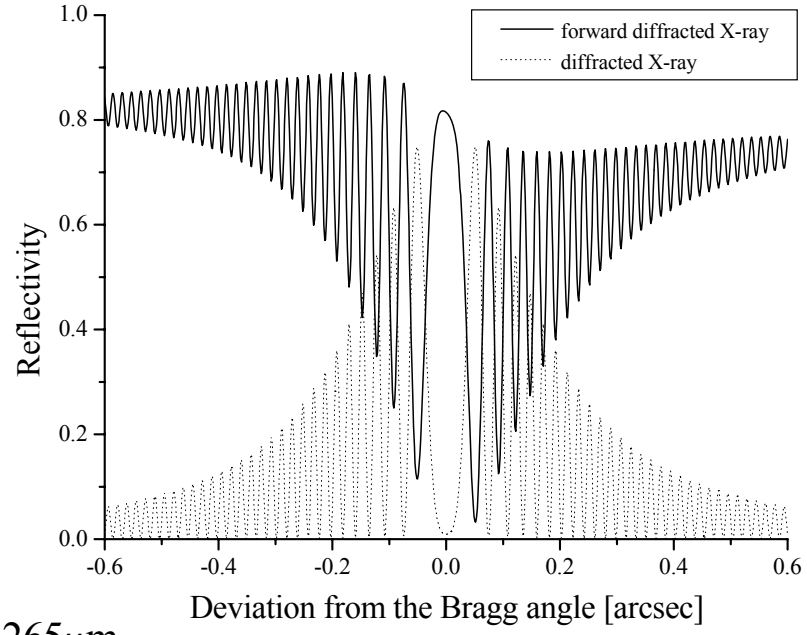

(e) 1265μm

Figure 19. Rocking curves of forward diffracted and diffracted X-ray of A(L) at incident X-ray energy of 35keV when thicknesses are varied by approximately 30 μm. (a) 1147 μm, (b) 1175 μm, (c) 1205 μm, (d) 1235 μm, and (e) 1265 μm.

Figure 20. Coloured volume-rendered 3D X-ray CT images displayed with various opacities.

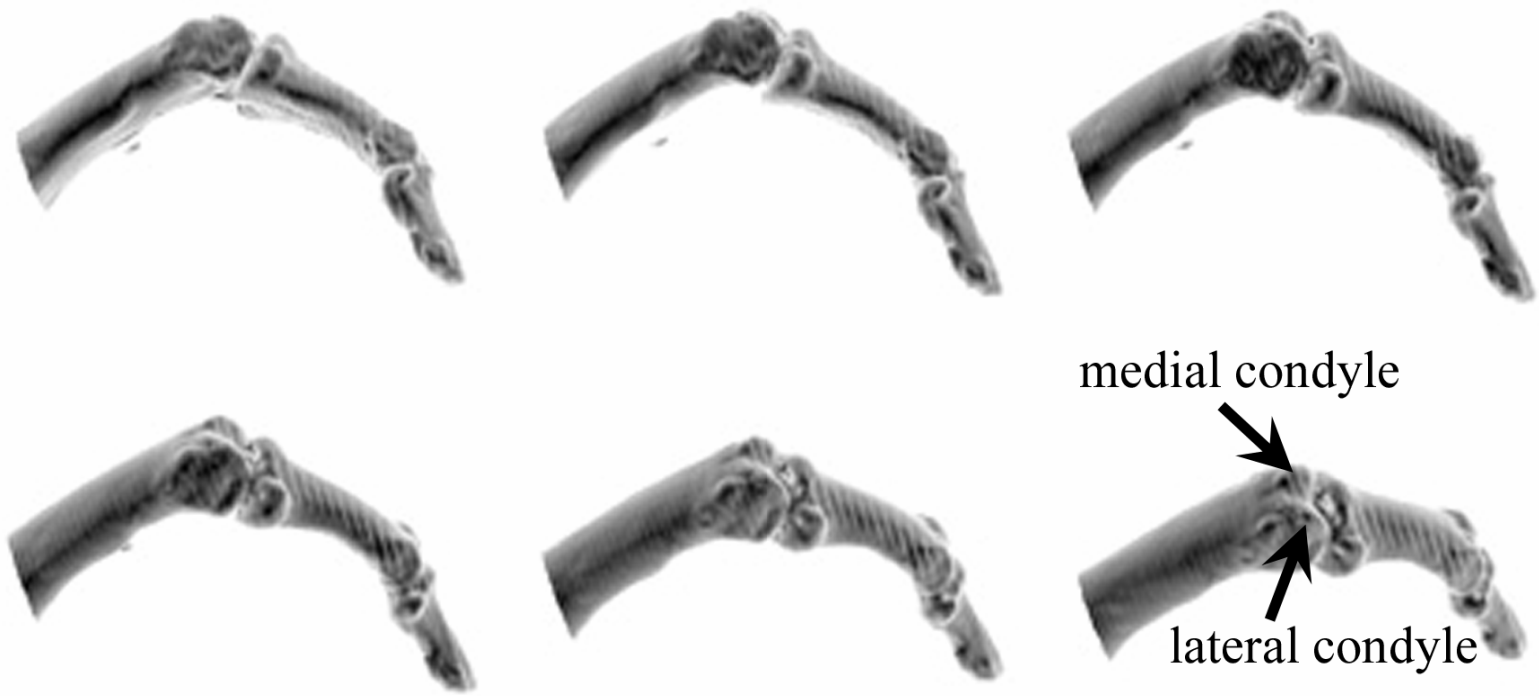

Figure 21. Volume-rendered 3D X-ray CT images of bones viewed from various angles.

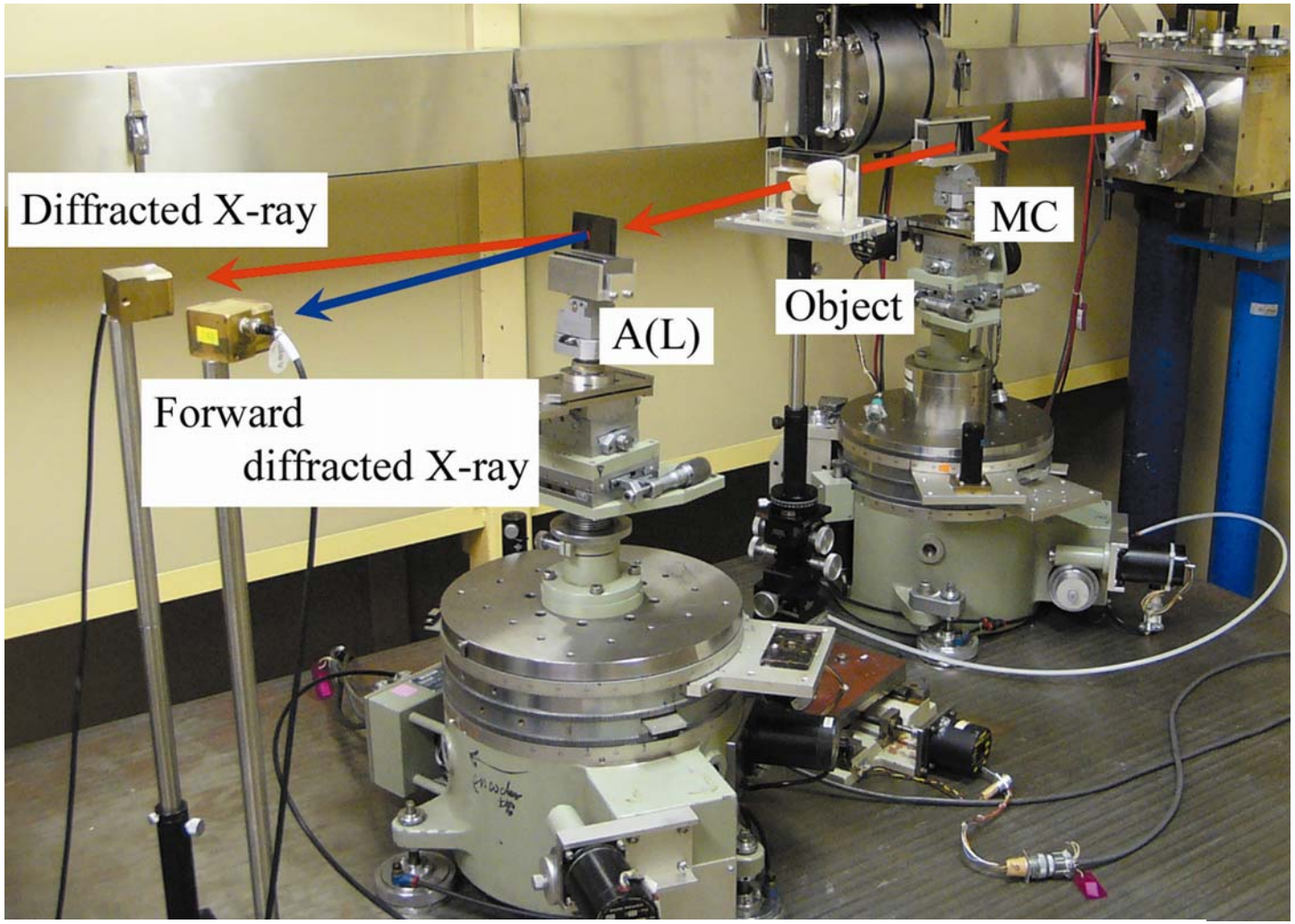

Figure 22. Photograph of the experimental apparatus at BL14B.

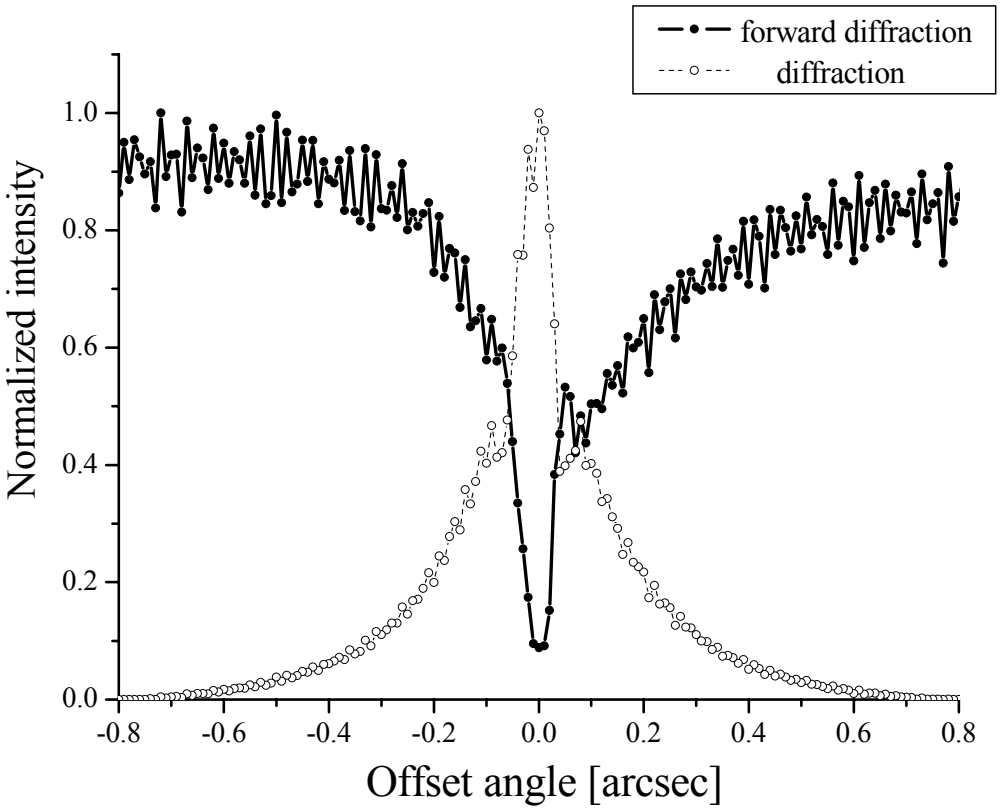

Figure 23. Representative measured rocking curves of forward diffraction and diffraction by A(L) without an object at BL14B.

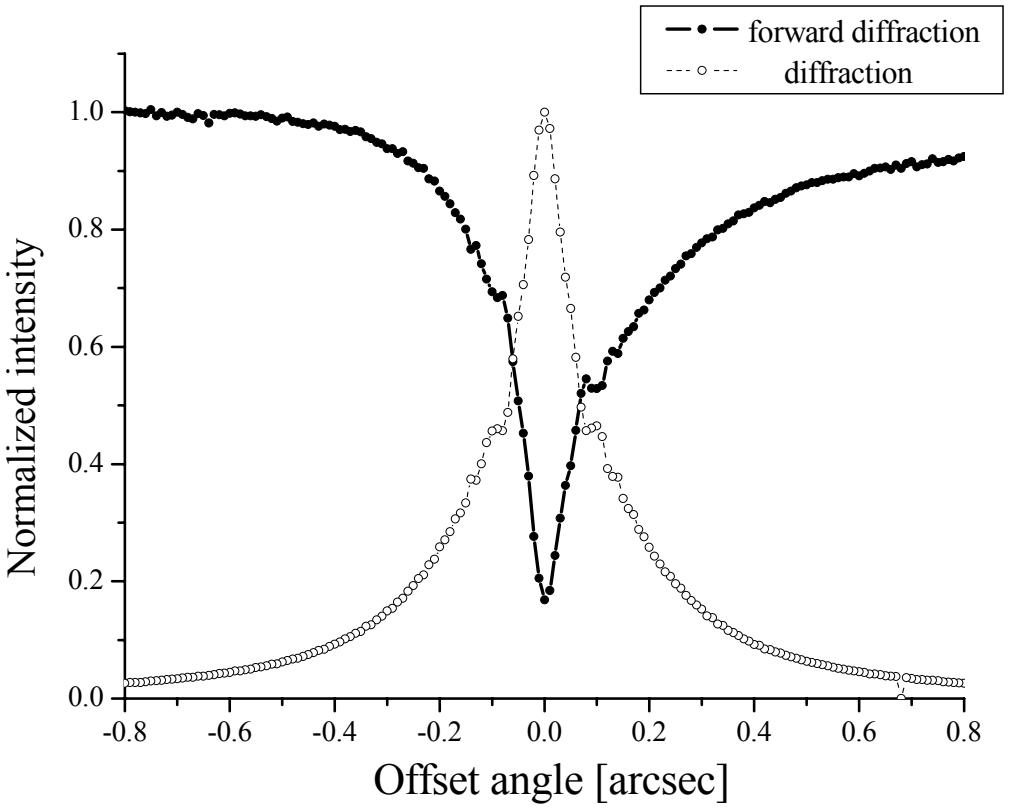

Figure 24. Representative measured rocking curves of forward diffraction and diffraction by A(L) without an object at BL14C1.

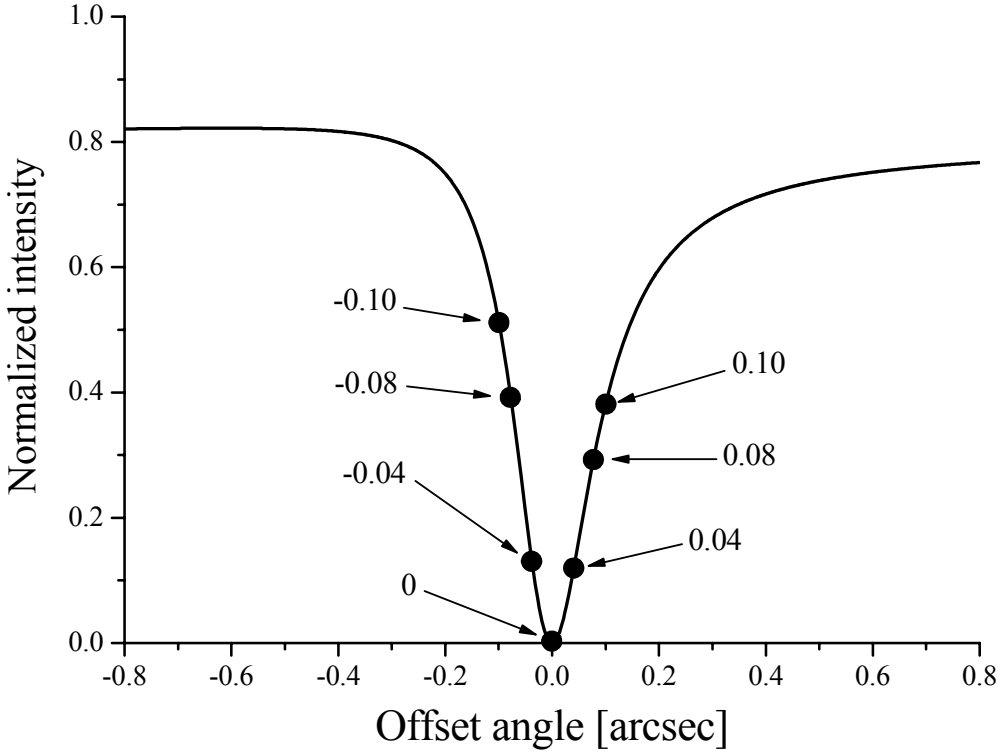

Figure 25. Points of angles of A(L) offset from the just Bragg condition by 0.04, 0.08, and 0.10 arcsec to either higher or lower angular positions.

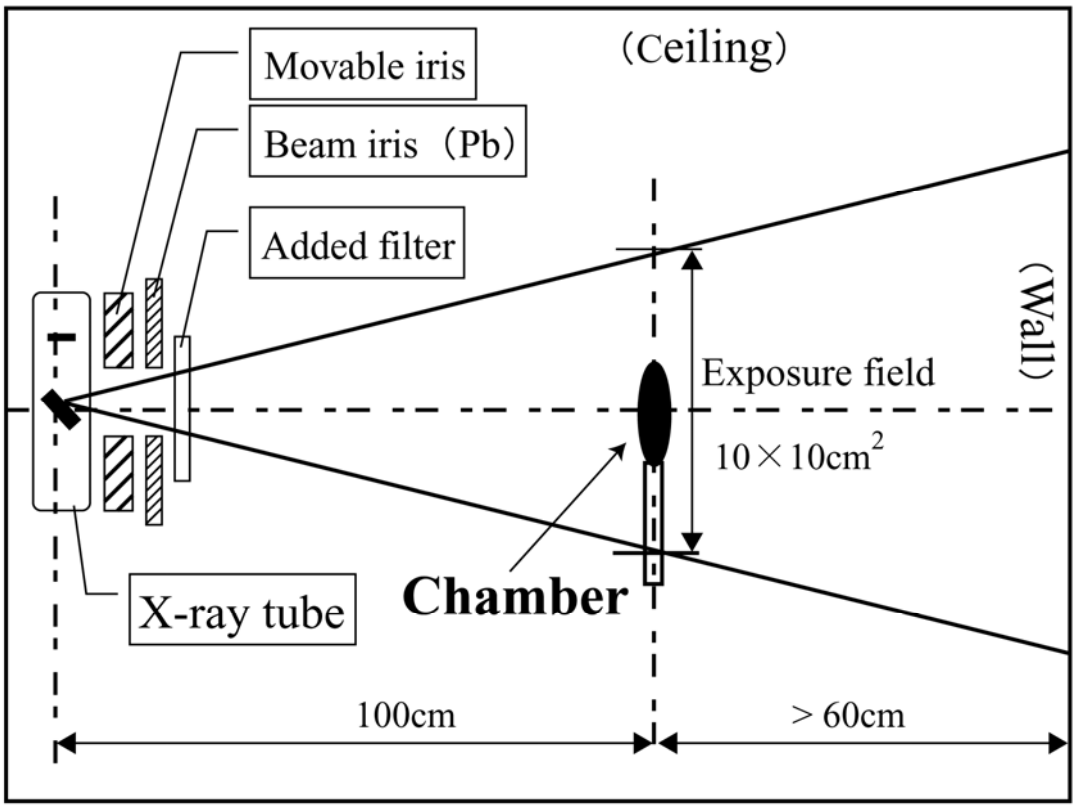

Figure 26. Setup for the measurement of entrance surface dose.

Figure 27. Photograph of 6 cm^3 ion chamber; 10X5-6 with model 9015 monitor (Radcal Corporation).

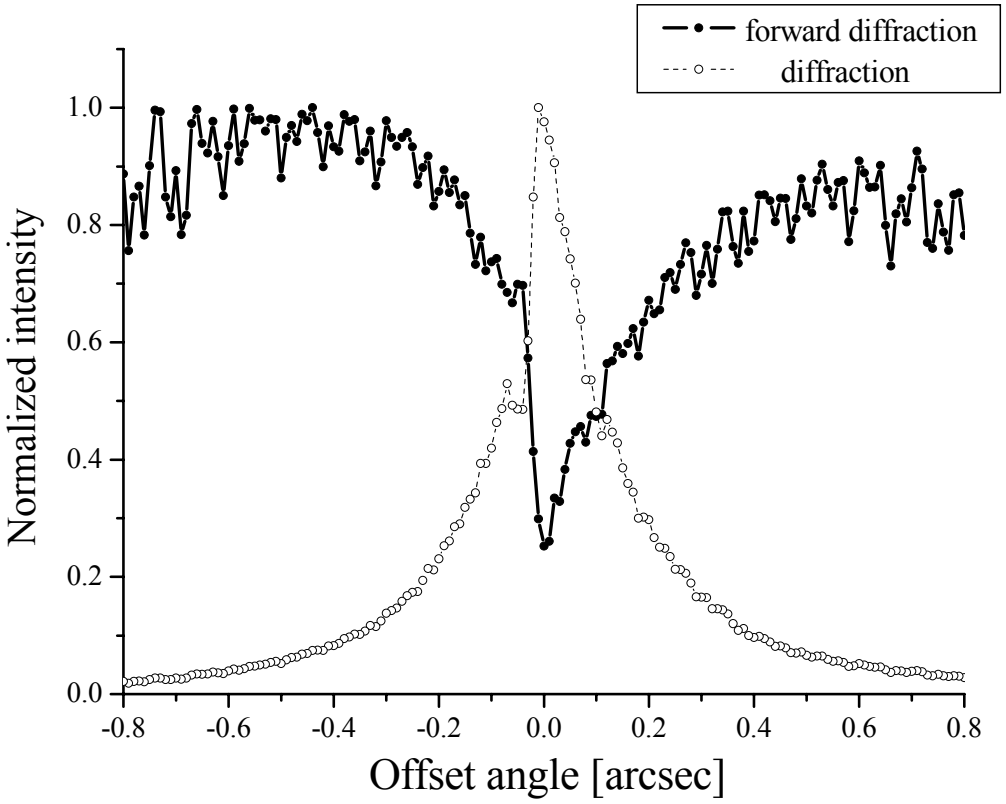

Figure 28. Representative measured rocking curves of forward diffraction and diffraction by A(L) without an object at BL14B at operating mode with 3 GeV and 200 mA.

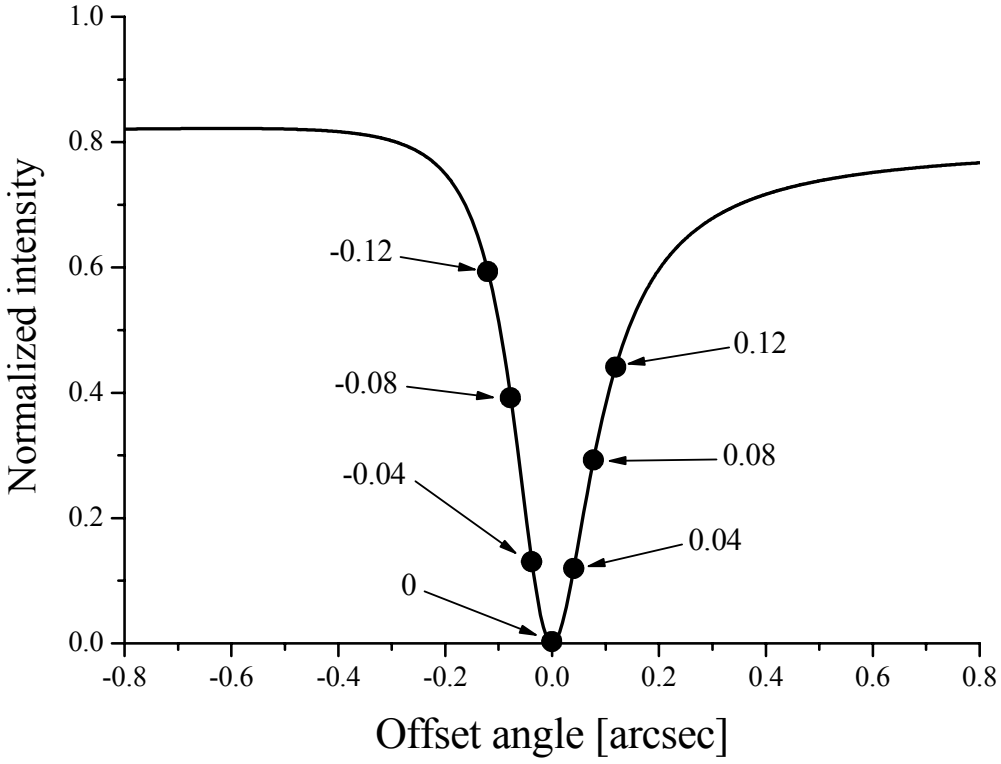

Figure 29. Points of angles of A(L) offset from the just Bragg condition by 0.04, 0.08, and 0.12 arcsec to either higher or lower angular positions.

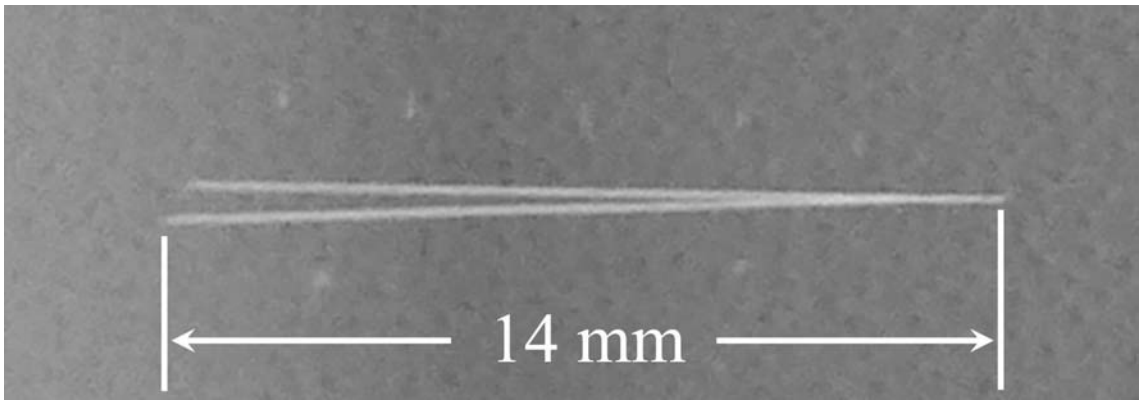

Figure 30. Optical photograph of the phantom used for the measurement of spatial resolution for refraction contrast.

Figure 31. Photomicrograph of the phantom used for the measurement of spatial resolution for refraction contrast.

Chapter 5

Results

5.1 Results of the preliminary experiment of PIP joint imaging by X-ray DFI at Photon Factory BL14B

Figures 32 (a)-(g) show the X-ray images of the PIP joint taken at BL14B as a preliminary experiment. White part corresponds to the area where X-ray intensity is strong. The joint is in the lateral position with a slight oblique tilt in order to demonstrate the articular cartilage on the head of the proximal phalanx, which was discussed in **4.3**. Figure 32 (a) is an absorption contrast image taken with the A(L) set at 5 arcsec lower than the just Bragg position. Only the bone structures and the dim contour of skin are visible. Figure 32 (b) is a pseudo-DFI taken at an A(L) angular position

0.05 arcsec lower than the just Bragg condition, while Fig. 32 (c) shows the subordinate BFI. Figure 32 (d) is a DFI taken at the just Bragg angular position of the analyzer, and Fig. 32 (e) is the subordinate BFI. The top-left area of the image is very dark (no X-ray) in Fig. 32 (d) and very bright (intense X-ray) in Fig. 32 (e), which proves that DFI was achieved perfectly. Figure 32 (f) is the pseudo-DFI taken at an A(L) angular position 0.05 arcsec higher than the just Bragg condition, and Fig. 32 (g) the subordinate BFI.

In Figs. 32 (b)-(g), soft tissues are clearly visible, whereas bone structures are poorly distinguished. Articular cartilage is well visualized in Figs. 32 (b), (d) and (f). It should be noted that the appearance of articular cartilage differs in Figs. 32 (b), (d) and (f). Conversely, all BFIs except Fig. 32 (g) demonstrate a low depiction ability for articular cartilage, which indicates that further research is required regarding the angular dependency of the A(L) on the ability to depict articular cartilage. Wrinkles are clearly observed on the skin surface, particularly in the top-right area of these images. There is a possibility that contrasts of wrinkles may be superimposed upon those of articular cartilage. A hollow observed on the articular cartilage may be due to this effect. Figure 33 (a) is a photograph of the entire object. Figure 33 (b) is a magnified view of the area enclosed by the white rectangle shown in Fig. 33 (a). A hollow can be seen on the skin (white arrow) in the area that corresponds to the hollow seen in Fig. 32; this

may be the cause of this appearance. When a lesion is diagnosed from morphological change, this effect could be a fatal matter.

5.2 Results of the further detailed experiment of PIP joint imaging by X-ray DFI at Photon Factory BL - 14C1

The beam divergences of the X-ray through soft tissues and both soft tissues and bone were examined by measuring their rocking curves of diffraction, and were estimated from each full width half maximum (FWHM) as compared with that of the diffraction beam without an object. Figure 34 shows the 5 mm square incident X-ray areas for measurement of the rocking curves. (A) and (B) in Fig. 34 correspond to the areas for only soft tissues and for both soft tissues and bone, respectively. X-rays propagate in the order of skin, adipose tissues, and skin in the area (A); and skin, adipose tissues, bone, adipose tissues, and skin in the area (B). The normalized rocking curves are shown in Fig. 35. Curve (a) represents the rocking curve of forward diffraction for air, while (b), (A), and (B) represent the curves of diffraction for air, soft tissues and both soft tissues and bone, respectively. The relevant FWHM were approximately 0.14 arcsec for (b), 0.26 arcsec for (A), and 0.65 arcsec for (B).

Figure 36 shows X-ray images of the PIP joint taken at BL14C1 as

a detailed experiment. The object was immersed in water. Figure 36 (a) is the absorption contrast image taken with the A(L) set 5 arcsec lower than the just Bragg position. Only the bone structures are visible; skin contour seen in Fig. 32 (a) has disappeared due to minimal differences in absorption coefficients between water and skin. Figures 36 (b), (d), (f), (h), (j), (l), and (n) are images acquired on the forward diffracted X-rays (left-hand column). Figures 36 (c), (e), (g), (i), (k), (m), and (o) are images acquired on the diffracted X-ray (right-hand column). The angular position of the A(L) for each of these images is shown in the middle column. Figure 36 (h) corresponds to X-ray DFI. Each image in left-hand column depicts articular cartilage clearly, contrast produced from wrinkles is reduced, and the hollow on articular cartilage observed in Figs. 32 (b), (d) and (f) is no longer visible.

5.3 Results of the experiment for clinical application of X-ray DFI at Photon Factory BL14B

With the aim of developing the clinical application of X-ray DFI for the diagnosis of arthropathy, the present study examines whether the depiction ability for articular cartilage is maintained with the introduction of an intensifying screen for dose reduction. This was applied to the normal PIP joint and to a joint containing a lesion. Figures 37 and 38 show images

of a normal PIP joint without and with an intensifying screen, respectively. The layouts of the images are the same as that for Fig. 36. Articular cartilage was visualized with the use of an intensifying screen. The exposure dose D_{es} for non-screen imaging and a film/screen system were estimated to be approximately 3.18 mGy and 0.06 mGy, respectively. This exposure dose with an intensifying screen is comparable to the dose for current clinical X-ray imaging. Figures 39 and 40 show the images of a different PIP joint without and with an intensifying screen, respectively. The layouts of the images are also the same as that in Fig. 36. The small lesion at the articular cartilage on the medial condyle of the proximal phalanx is clearly revealed in Figs. 39 (b), (d), (f), and (h). The discontinuous line of articular cartilage and irregular contour of compact bone beneath this area are identified in these images. These findings refer to the images with an intensifying screen (Figs. 40 (b), (d), (f) and (h)), although the spatial resolution is degraded and the images are blurred.

5.4 Results of the estimation of spatial resolution for X-ray DFI

An X-ray DFI and subordinate BFI of the phantom developed for measuring spatial resolution are shown in Fig. 41. The scratched marks for

orientation and scale are visible on both sides. Each scratched line is visible as a few sharp white lines to the right of the black band in Fig. 41 (a). The lines in Fig. 41 (b) are visible as a black band with white band on either side. These contrasts may cause a decrease in the spatial resolution for X-ray DFI. Even so, X-ray DFI will be of great value in clinical diagnosis because it can depict an object that cannot be visualized by absorption contrast images. The minimum distinguishable spaces between the two scratched lines on the DFI and subordinate BFI were 30 μm and 180 μm, respectively.

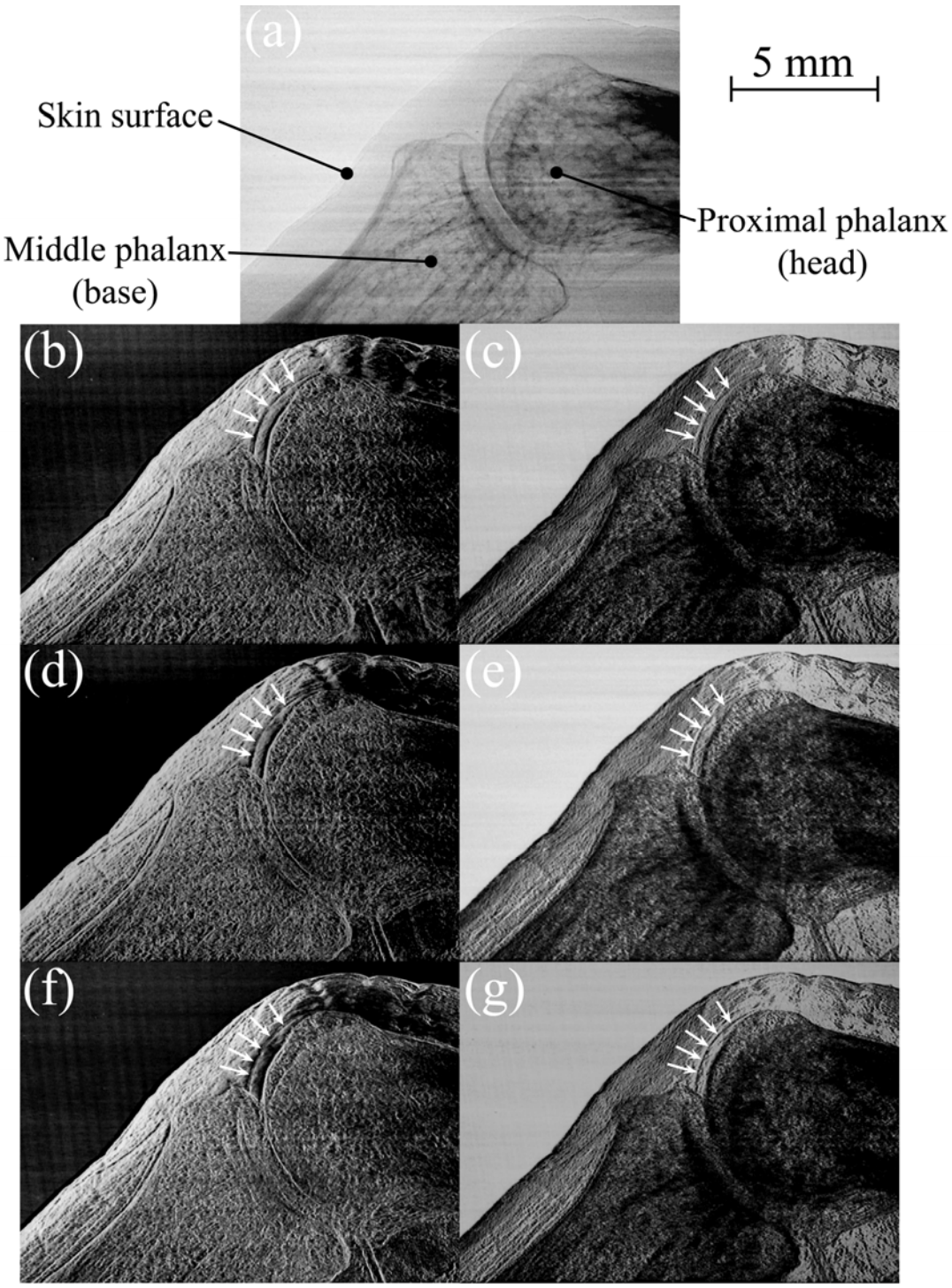

Figure 32. X-ray images of PIP joint taken at BL14B as a preliminary experiment. White arrows indicate articular cartilage on the head of the proximal phalanx.

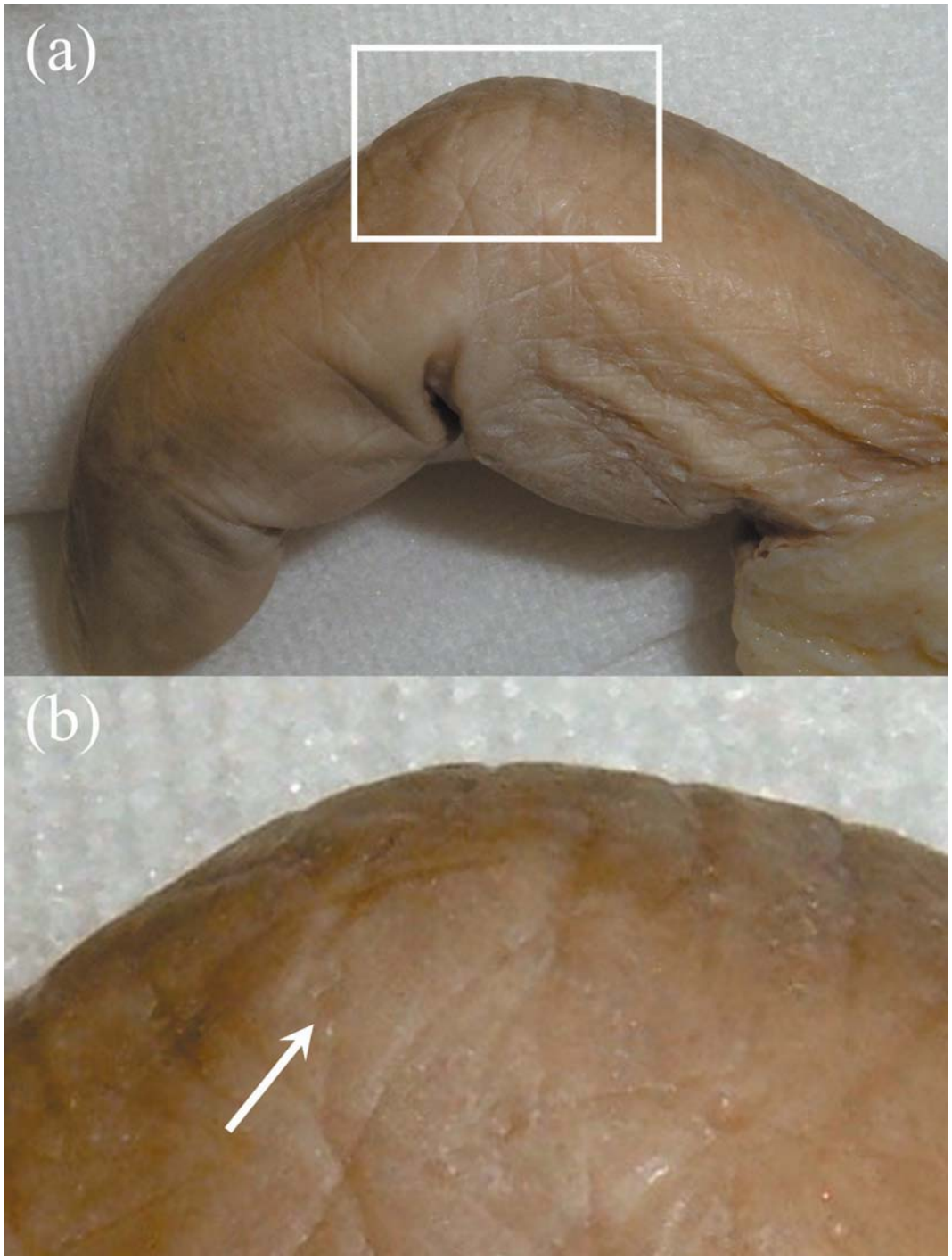

Figure 33. (a): Photograph of the whole object. (b): Magnified view of the area enclosed by the white rectangle in (a).

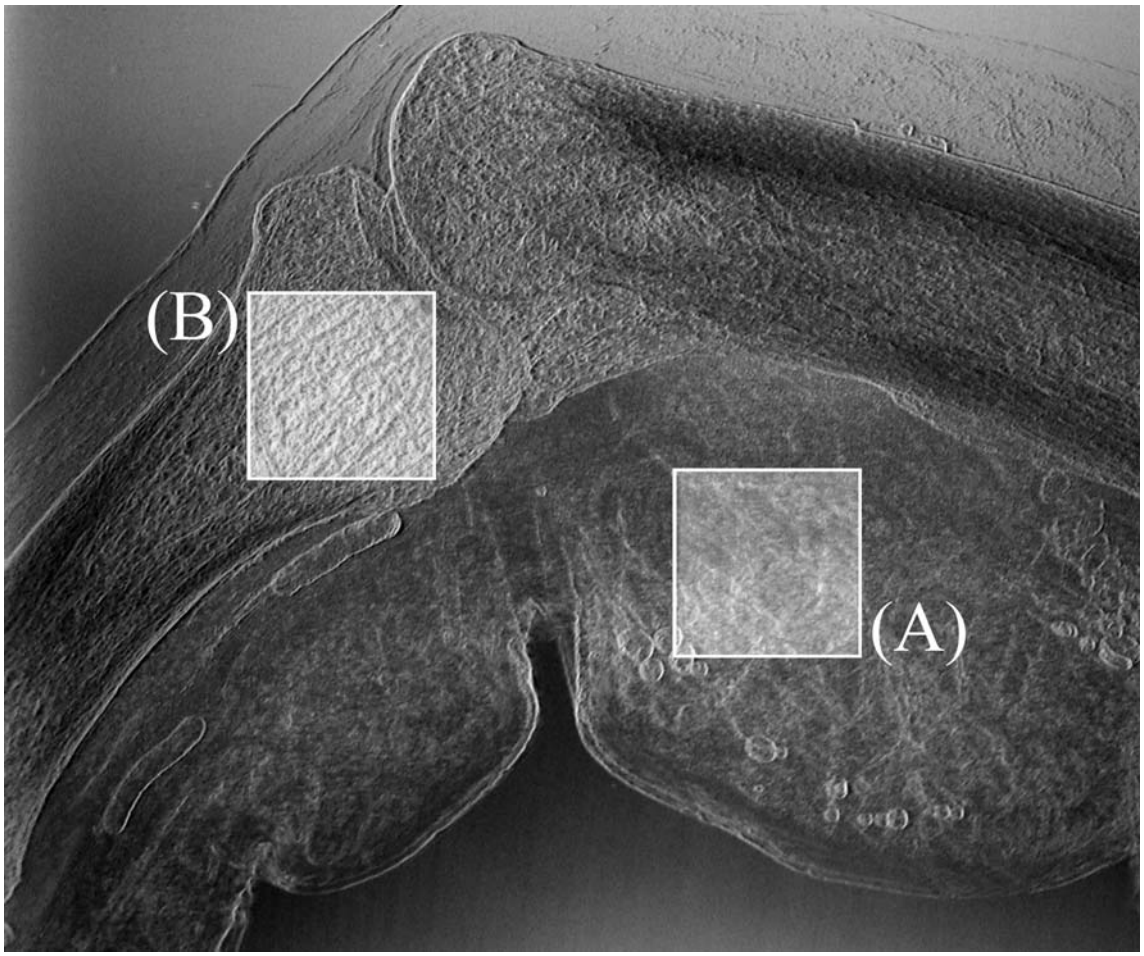

Figure 34. Areas X-rays are incident on for the measurement of rocking curves for soft tissues (A) and bone (B). Areas are both 5 mm square.

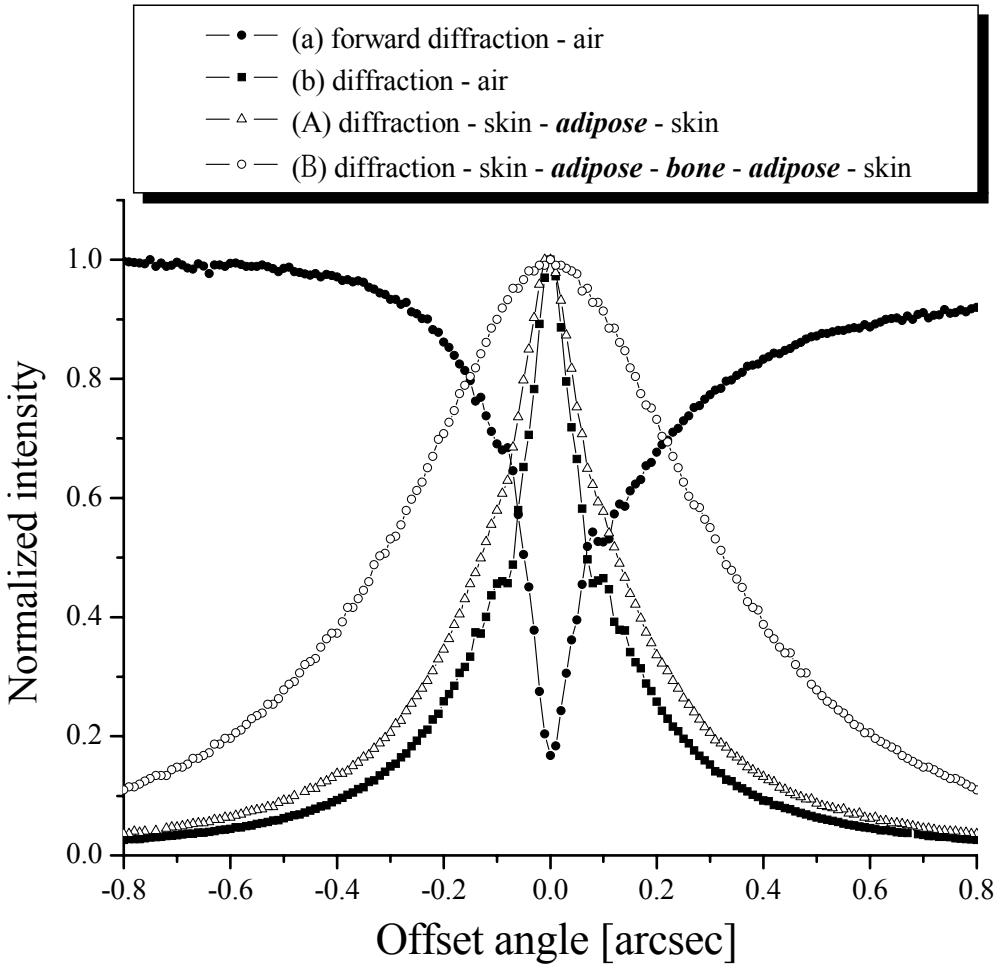

Figure 35. Normalized rocking curves for estimating the X-ray beam divergences.

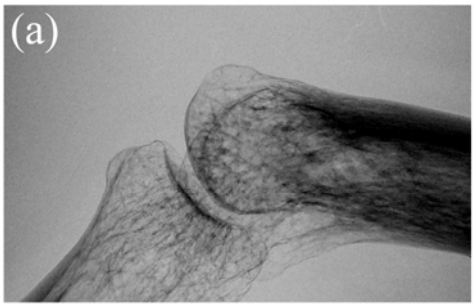

Absorption contrast image

Forward diffraction

Diffraction

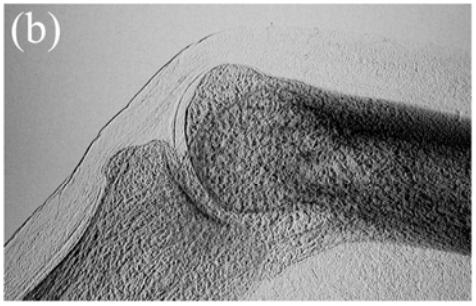

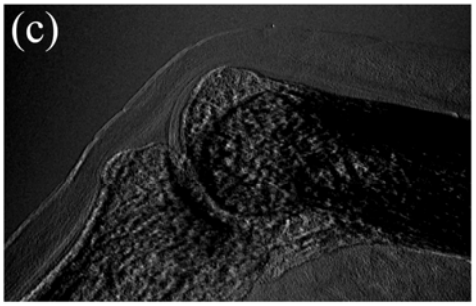

-0.10 arcsec

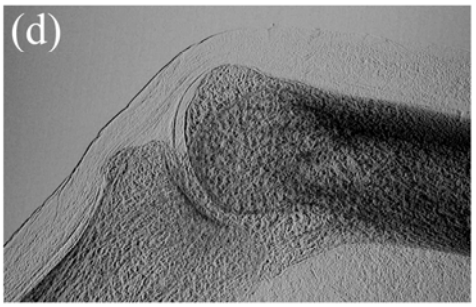

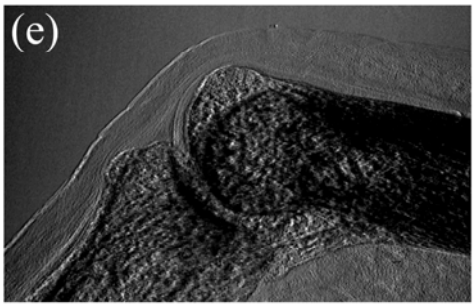

-0.08 arcsec

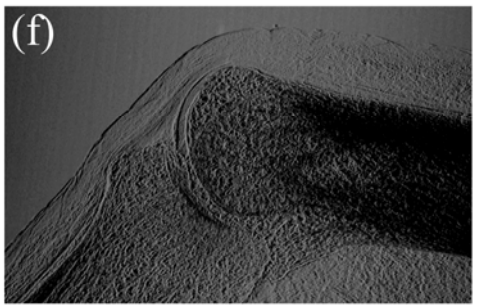

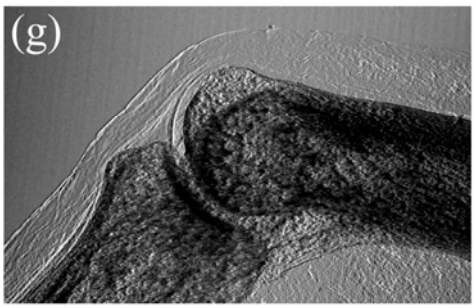

-0.04 arcsec

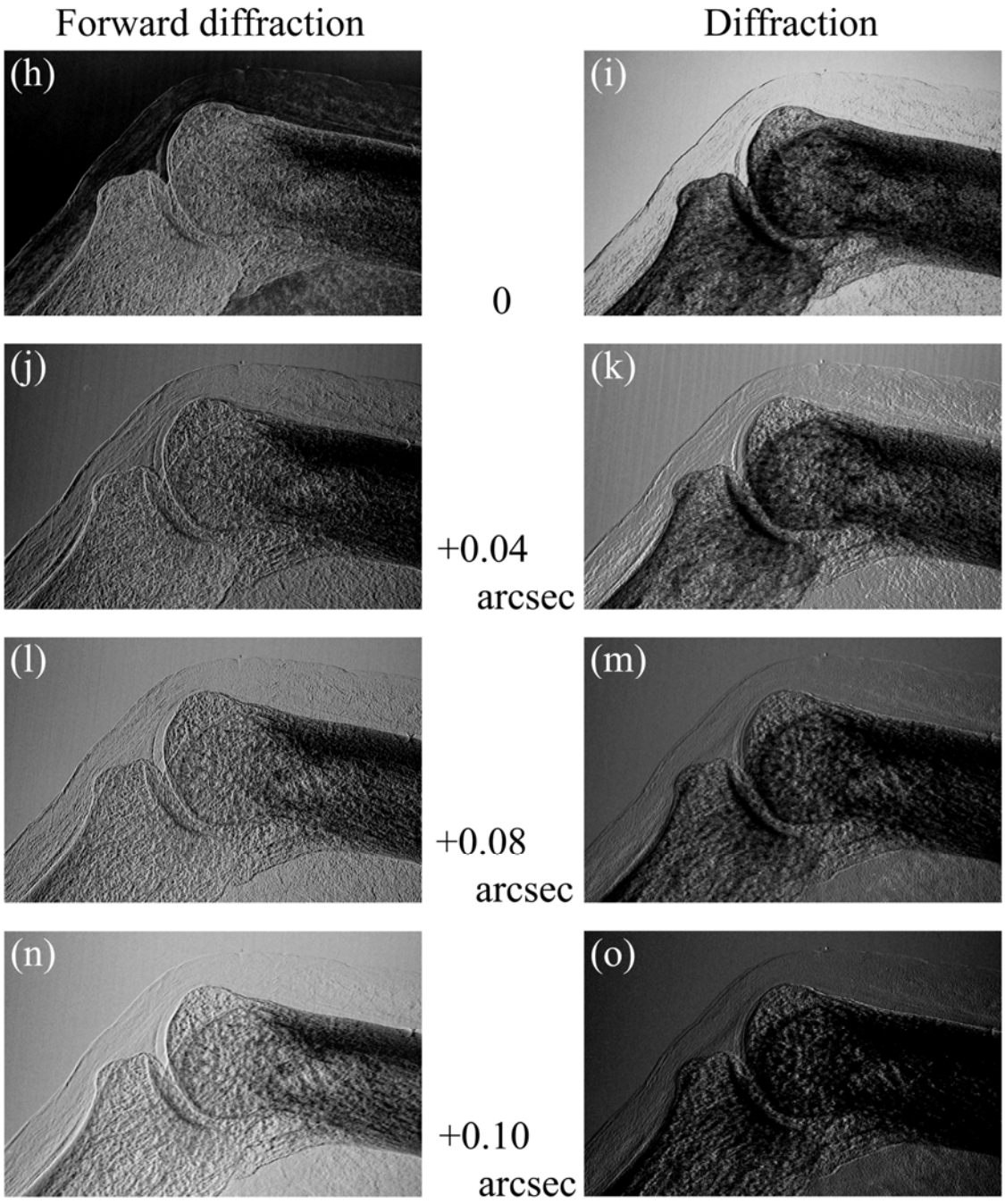

Figure 36. X-ray images of the PIP joint taken at BL14C1 as a detailed experiment.

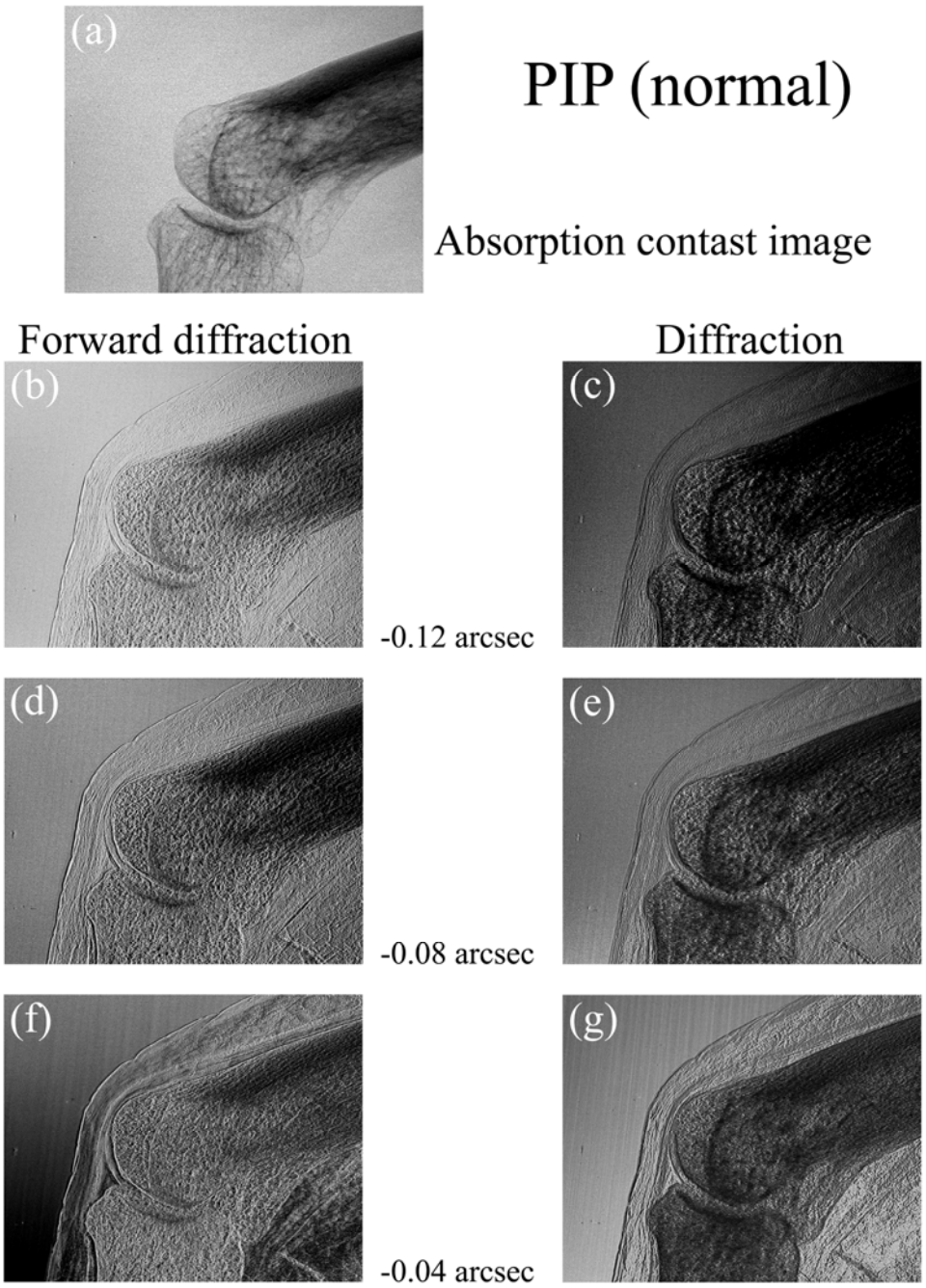
(a)
PIP (normal)
Absorption contast image
Forward diffraction
Diffraction
(b)
(c)
-0.12 arcsec
(d)
(e)
-0.08 arcsec
(f)
(g)
-0.04 arcsec

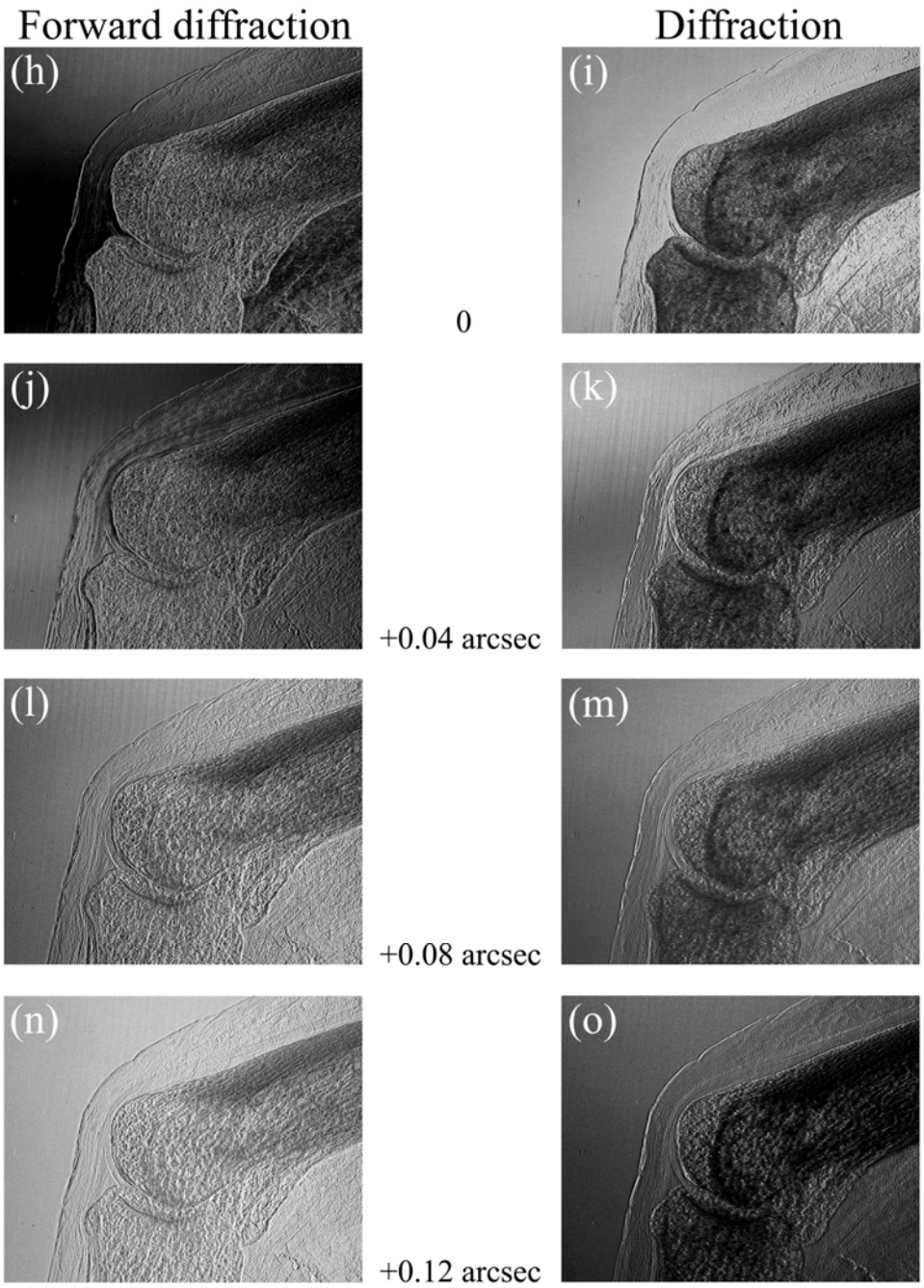

Figure 37. X-ray images of normal PIP joint without an intensifying screen.

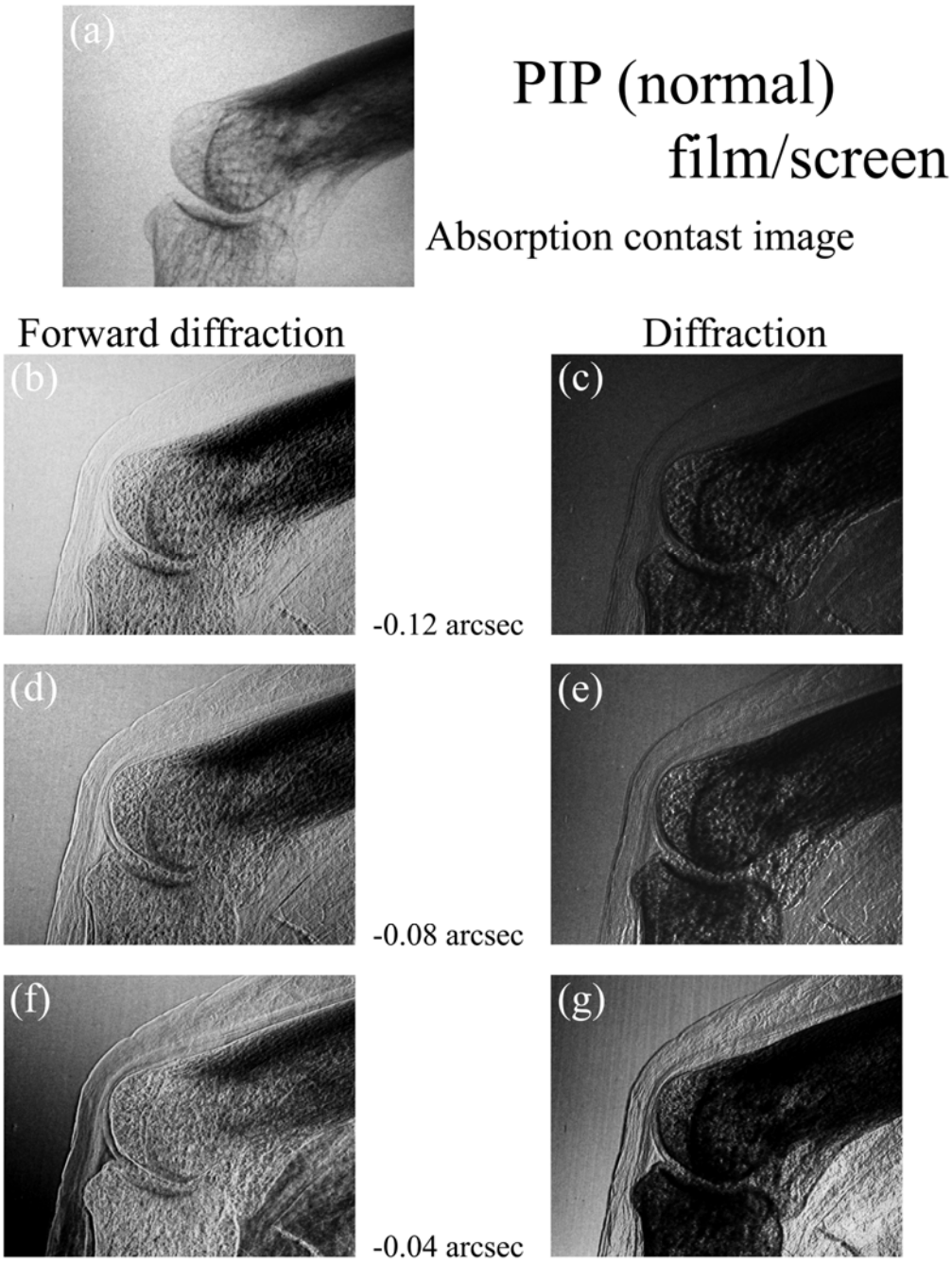
(a)
PIP (normal)
film/screen
Absorption contast image
Forward diffraction
Diffraction
(b)
(c)
-0.12 arcsec
(d)
(e)
-0.08 arcsec
(f)
(g)
-0.04 arcsec

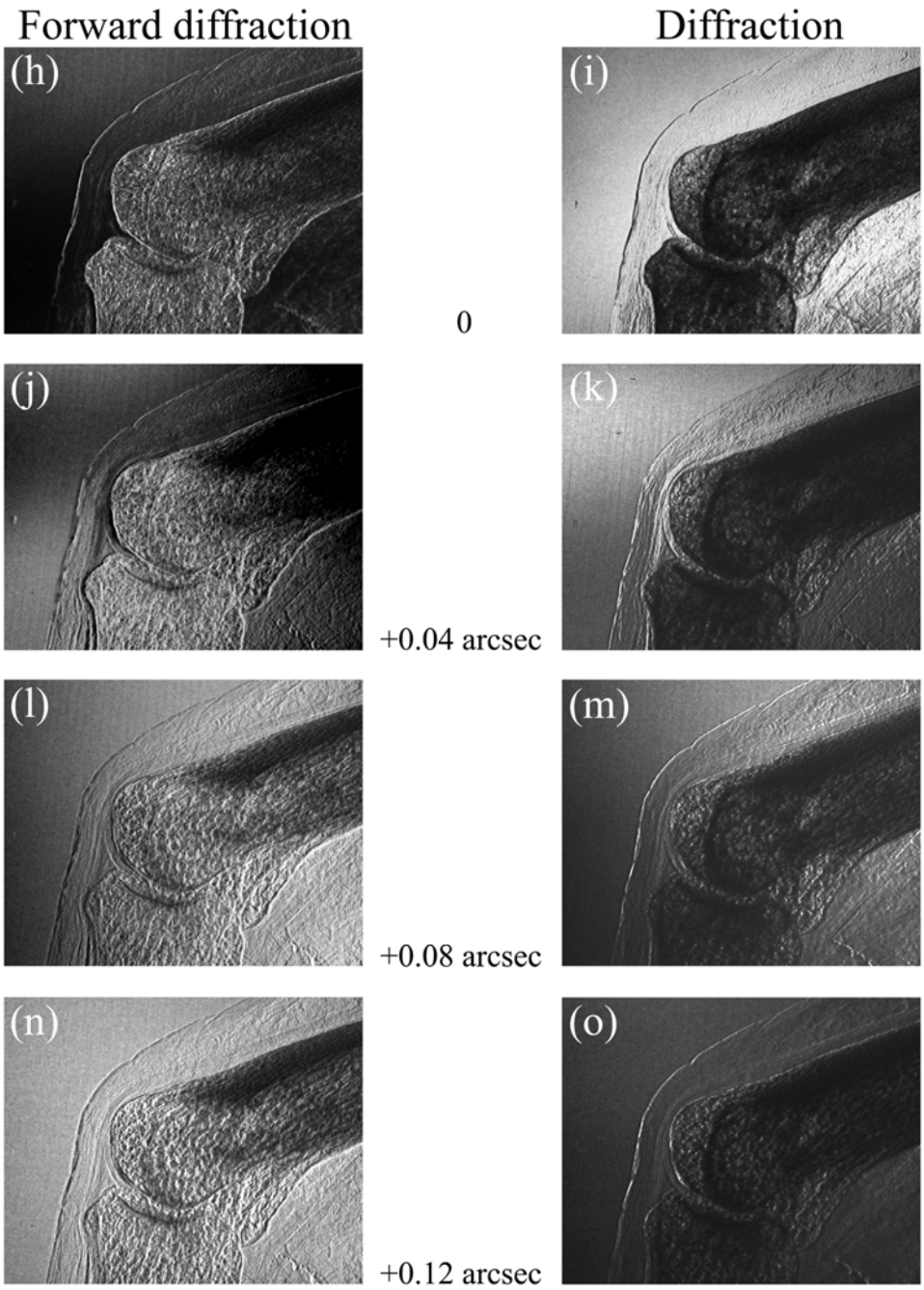

Figure 38. X-ray images of normal PIP joint with an intensifying screen.

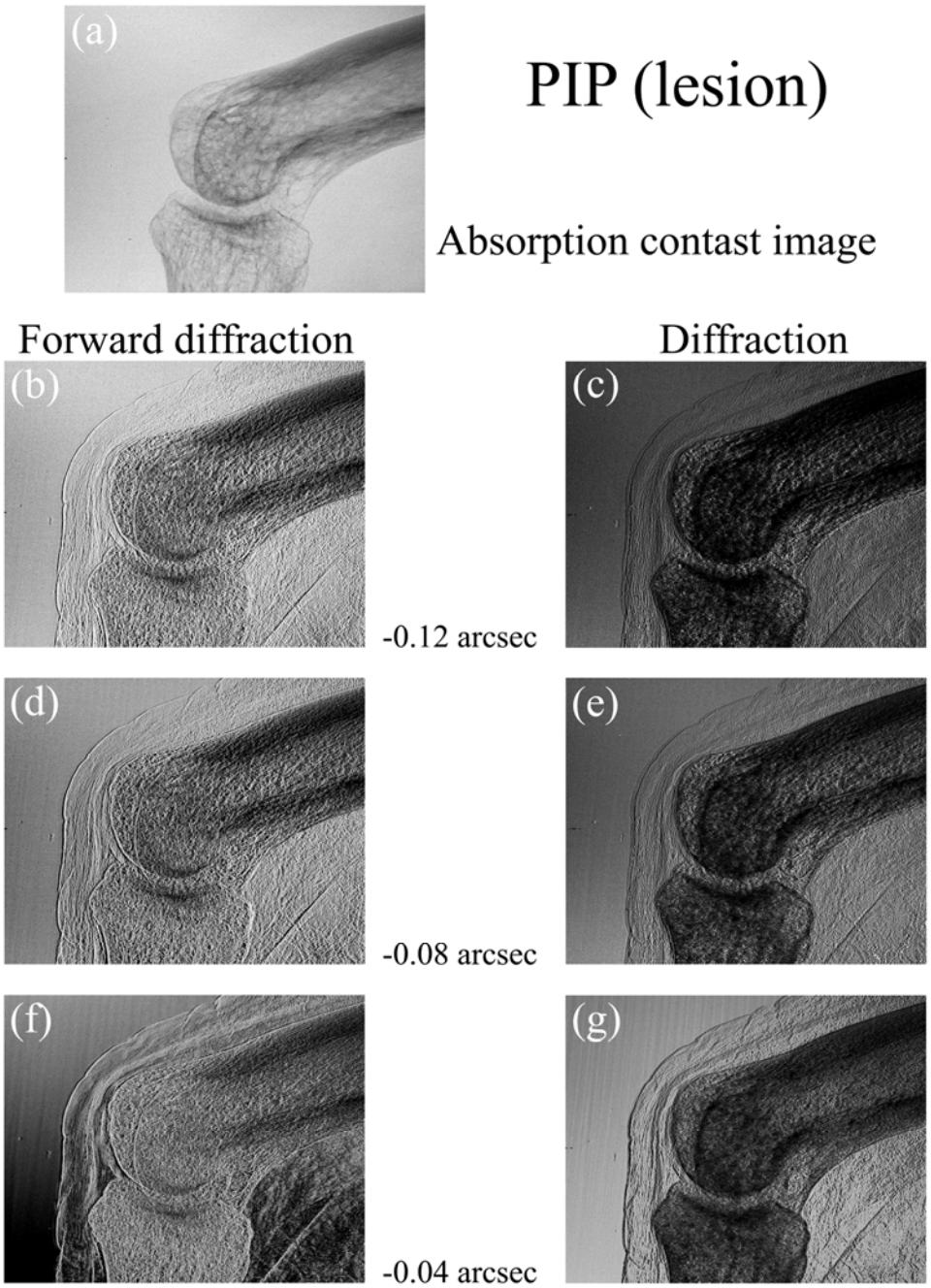
(a)
PIP (lesion)
Absorption contast image
Forward diffraction
Diffraction
(b)
(c)
-0.12 arcsec
(d)
(e)
-0.08 arcsec
(f)
(g)
-0.04 arcsec

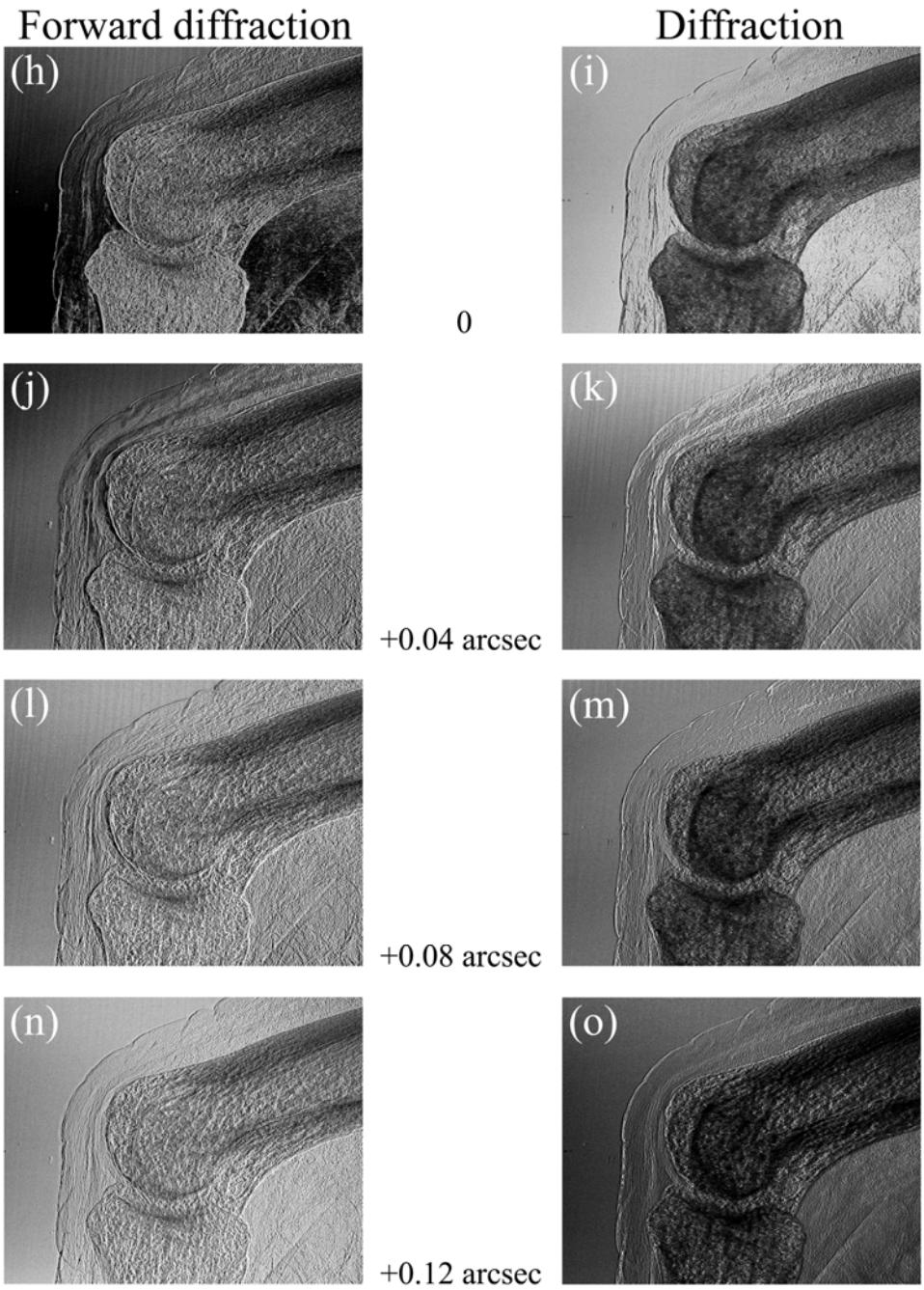

Figure 39. X-ray images of PIP joint with a small lesion without an intensifying screen.

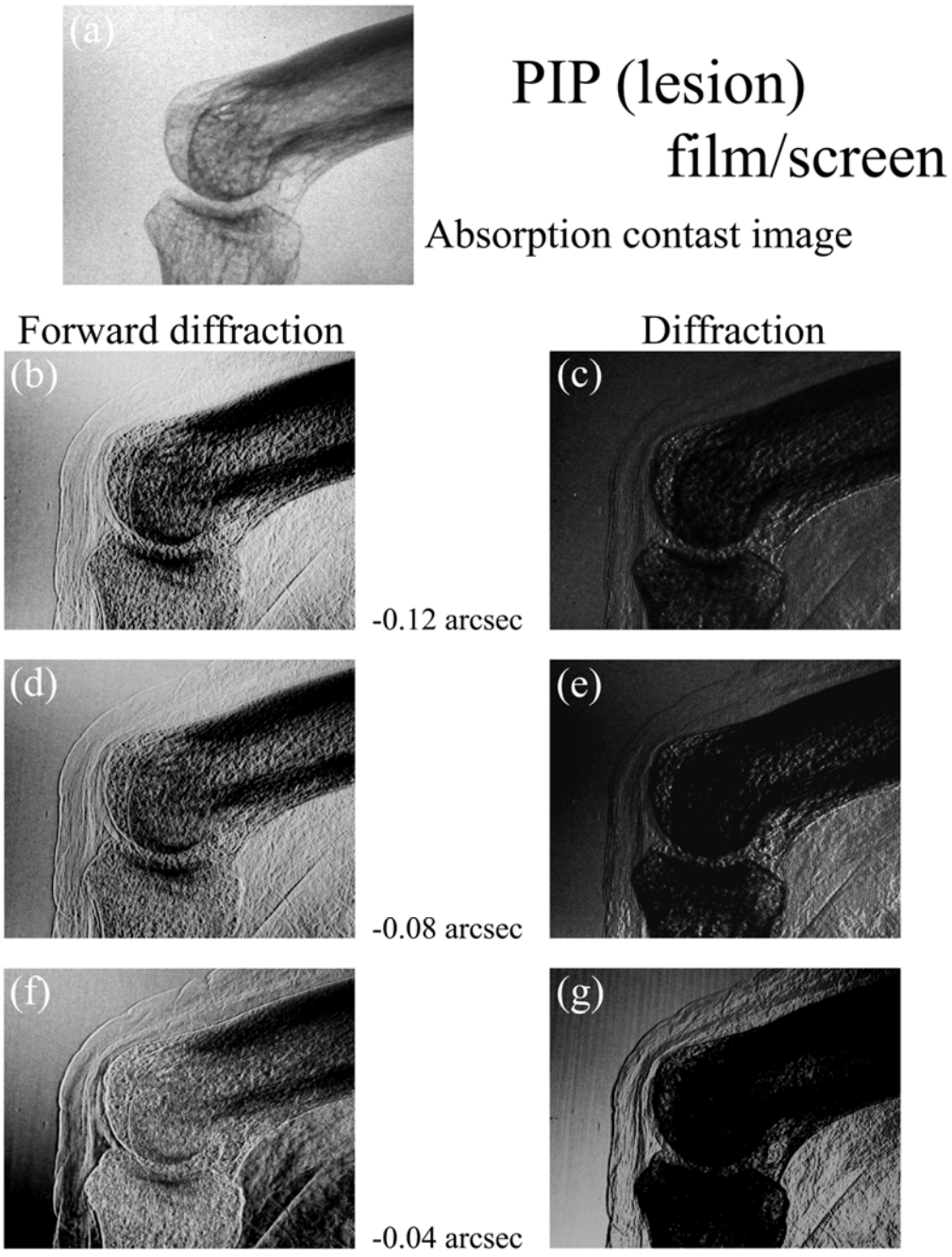
(a)
PIP (lesion)
film/screen
Absorption contast image
Forward diffraction
Diffraction
(b)
(c)
-0.12 arcsec
(d)
(e)
-0.08 arcsec
(f)
(g)
-0.04 arcsec

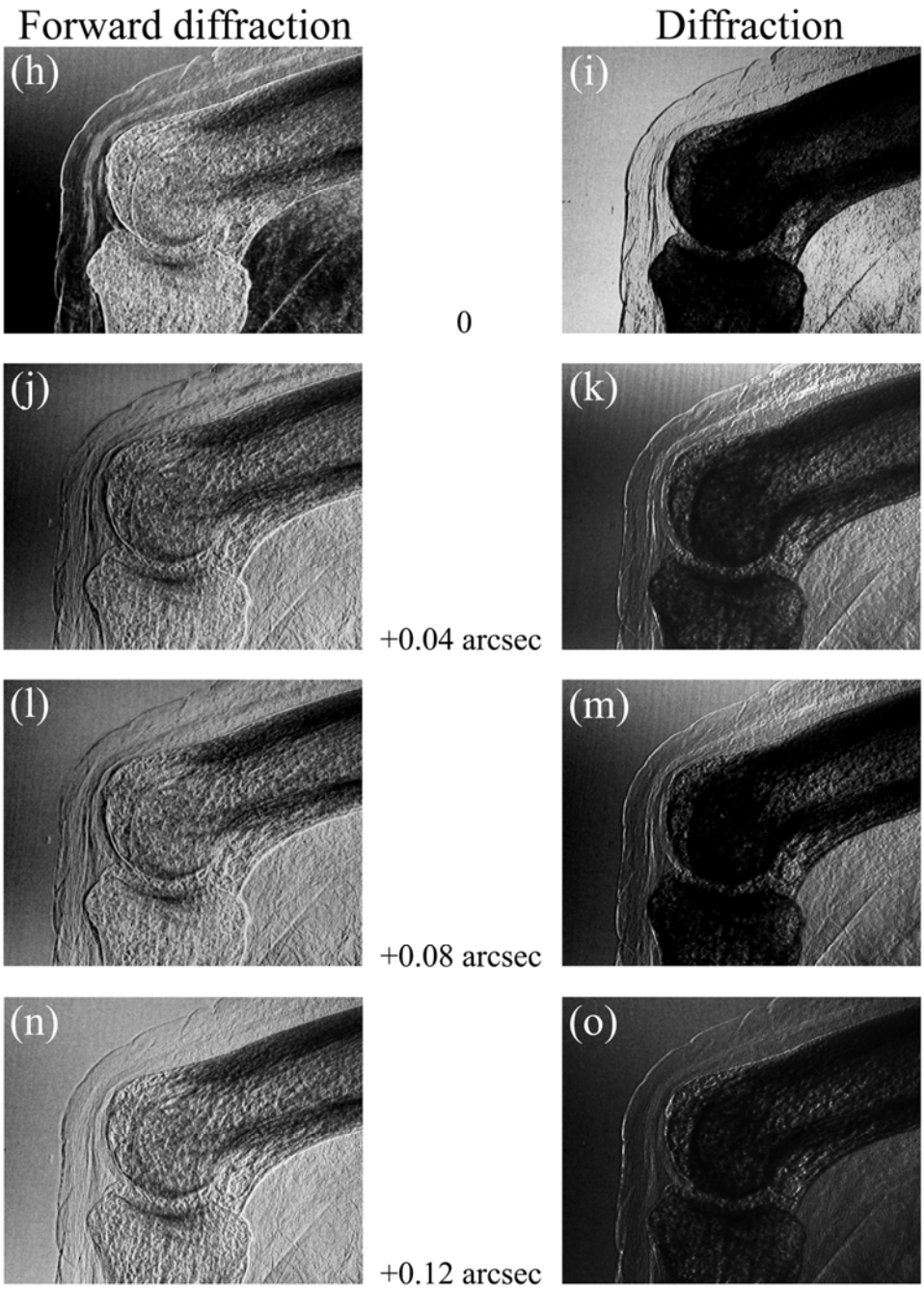

Figure 40. X-ray images of PIP joint with a small lesion with an intensifying screen.

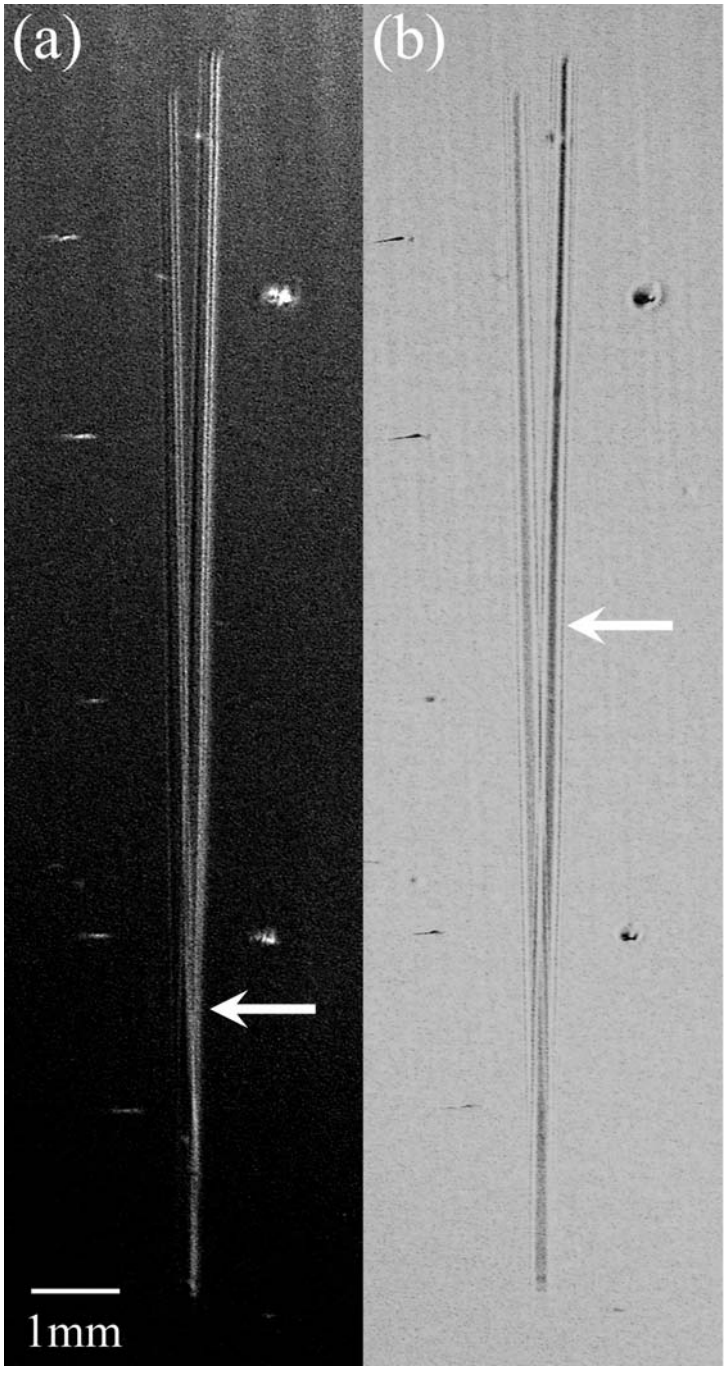

Figure 41. (a): X-ray DFI and (b): X-ray BFI acquired simultaneously using the phantom for measuring spatial resolution. White arrows show the minimum distinguishable points of the two lines.

Chapter 6

Magnetic Resonance Imaging of PIP joint articular cartilage

Among the non-invasive clinical examinations for image diagnosis, magnetic resonance imaging (MRI) is the gold standard for the demonstration of articular cartilage. When considering the application of X-ray DFI to the imaging of articular cartilage, a comparison is made between the depiction abilities of MRI and X-ray DFI. The same normal PIP joint used as the object earlier in this study was initially subjected to MRI scanning (Symphony 1.5T, SIEMENS) with a small loop receiving coil with a diameter of 40 mm. This coil is conventionally used for small objects. The sequences for T1 weighted and T2 weighted images were selected as follows:

T1 weighted image

TR: 845 msec
TE: 21 msec
Slice thickness: 1 mm
Slice gap: 0.2 mm
Echo train length: 3
FOV: 58 mm×40 mm
Average: 5
Matrix: 576×400
Pixel size: 0.10 mm×0.10 mm
Acquisition time: 19 min 30 sec

T2 weighted image

TR: 4000 msec
TE: 89 msec
Slice thickness: 1 mm
Slice gap: 0.2 mm
Echo train length: 11
FOV: 90 mm×63 mm
Average: 5
Matrix: 448×314
Pixel size: 0.20 mm×0.20 mm
Acquisition time: 19 min 18 sec

The resulting T1 and T2 weighted images are shown in Figs. 42 and 43, respectively. Their spatial resolutions are estimated to be 150-250 μm; the articular cartilages of the PIP are barely distinguishable.

MRI was then performed using a specialized 23-mm-diameter microscopic coil (Intera 1.5T, PHILIPS MEDICAL SYSTEMS). This is the smallest receiving coil available, and enables higher spatial resolution for a

small area. T1 weighted and T2 weighted image of a normal PIP and a joint containing a lesion were acquired using the same objects used for the X-ray DFI experiments. The sequences for T1 weighted and T2 weighted images for the normal PIP were selected as follows:

T1 weighted image

TR: 585 msec
TE: 13 msec
Slice thickness: 0.76 mm
Slice gap: 0.076 mm
Echo train length: 3
FOV: 60 mm×60 mm
Average: 4
Matrix: 512×512
Pixel size: 0.12 mm×0.12mm
Acquisition time: 6 min 40 sec

T2 weighted image

TR: 2500 msec
TE: 100 msec
Slice thickness: 0.76 mm
Slice gap: 0.076 mm
Echo train length: 15
FOV: 60 mm×60 mm
Average: 4
Matrix: 512×512
Pixel size: 0.12 mm×0.12 mm
Acquisition time: 5 min 41 sec

The resulting T1 and T2 weighted images of the normal PIP are shown in Figs. 44 and 45, respectively. Spatial resolution is estimated to be

approximately 150 μm, and the articular cartilages of the PIP are poorly distinguished in T1 weighted images. Note that the bone beneath the articular cartilage is not visible because it is composed of compact bone that generates no signal on MRI.

MRI of the PIP containing a lesion was performed under the same condition as above, with slight automatic adjustments by the system. The sequences for T1 weighted and T2 weighted images for the PIP containing a lesion were as follows:

T1 weighted image

TR: 624 msec
TE: 13 msec
Slice thickness: 0.73 mm
Slice gap: 0.073 mm
Echo train length: 3
FOV: 56 mm×56 mm
Average: 4
Matrix: 480×480
Pixel size: 0.12 mm×0.12mm
Acquisition time: 6 min 40 sec

T2 weighted image

TR: 2257 msec
TE: 100 msec
Slice thickness: 0.75 mm
Slice gap: 0.075 mm
Echo train length: 15
FOV: 56 mm×56 mm
Average: 4
Matrix: 480×480

Pixel size: 0.12 mm × 0.12 mm
Acquisition time: 4 min 48 sec

The resulting T1 and T2 weighted images of the PIP with the lesion are shown in Figs. 46 and 47, respectively. The articular cartilages of the PIP are distinguishable on the T1 weighted images, while the lesion is poorly visible as thin area of articular cartilage.

Figure 42. T1 weighted images of the normal PIP joint.

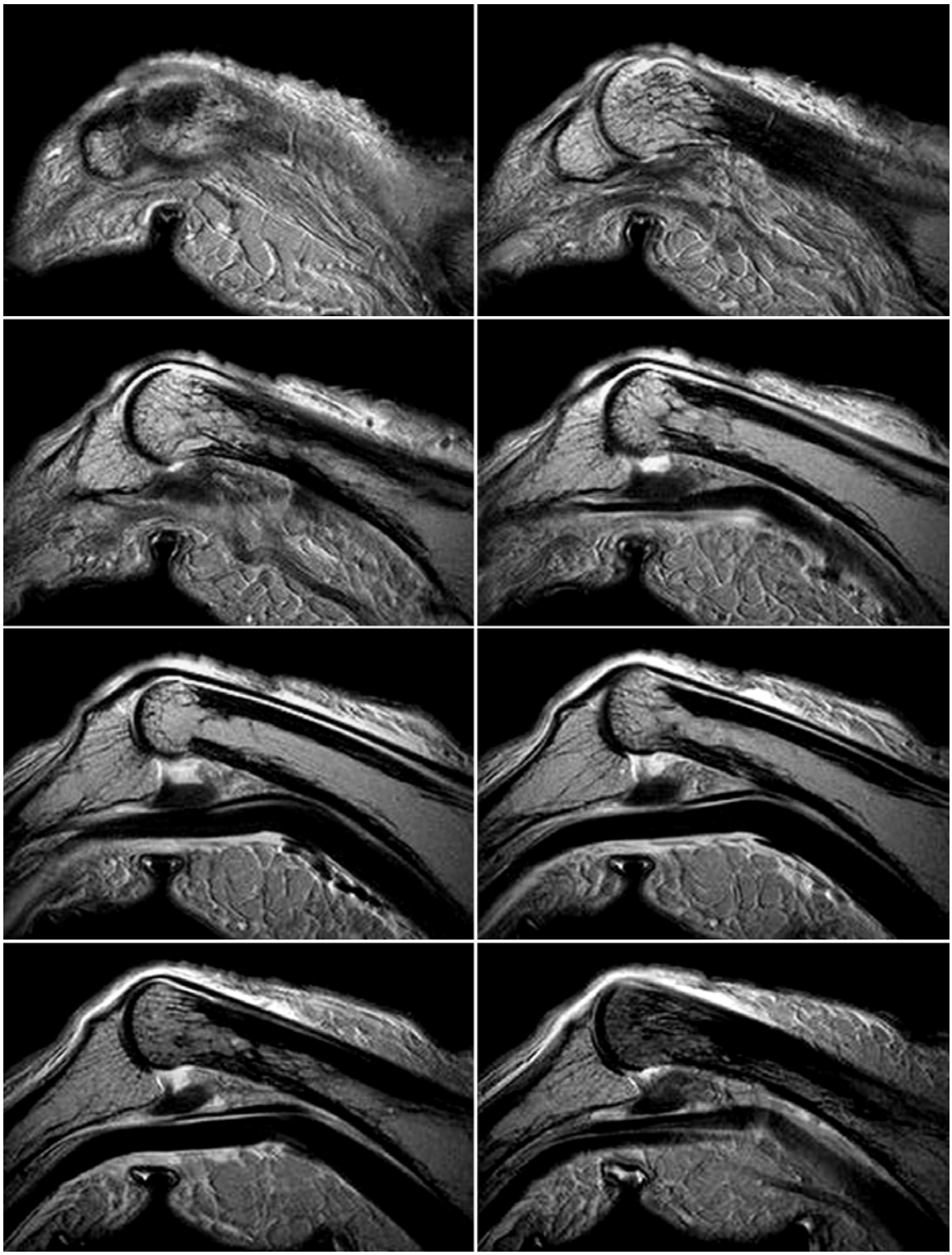

Figure 43. T2 weighted images of the normal PIP joint.

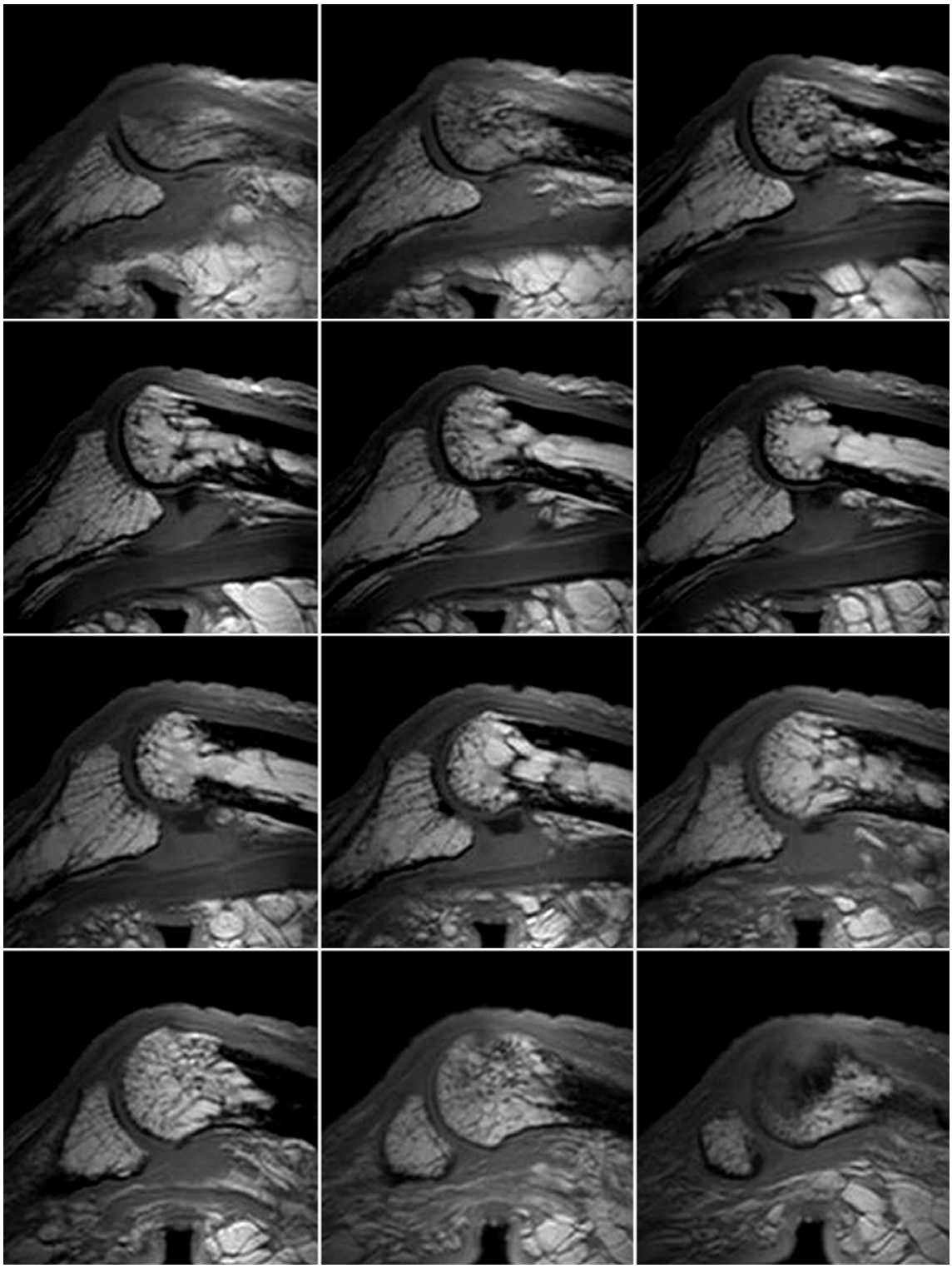

Figure 44. T1 weighted images of the normal PIP joint using microscopic coil.

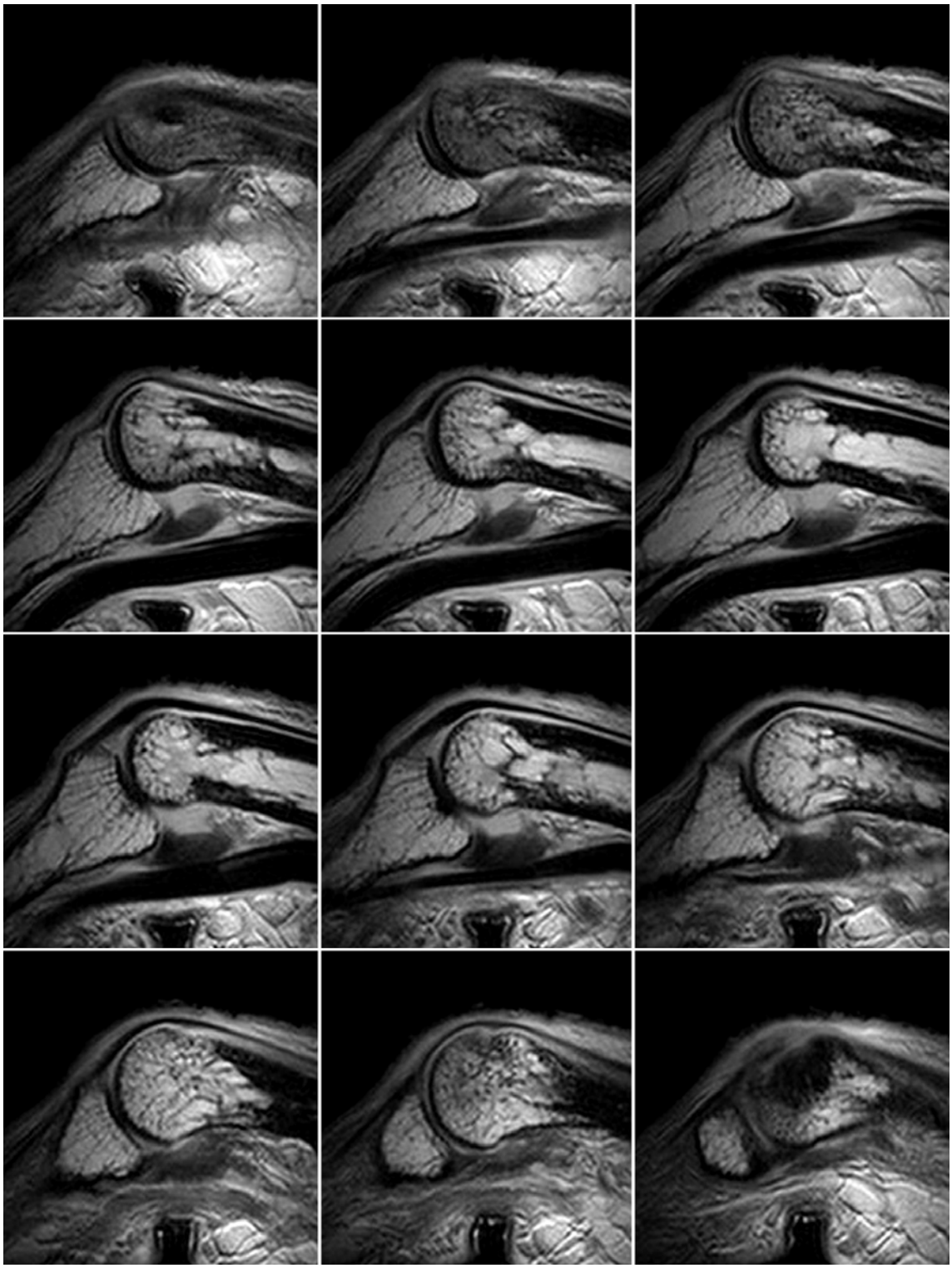

Figure 45. T2 weighted images of the normal PIP joint using microscopic coil.

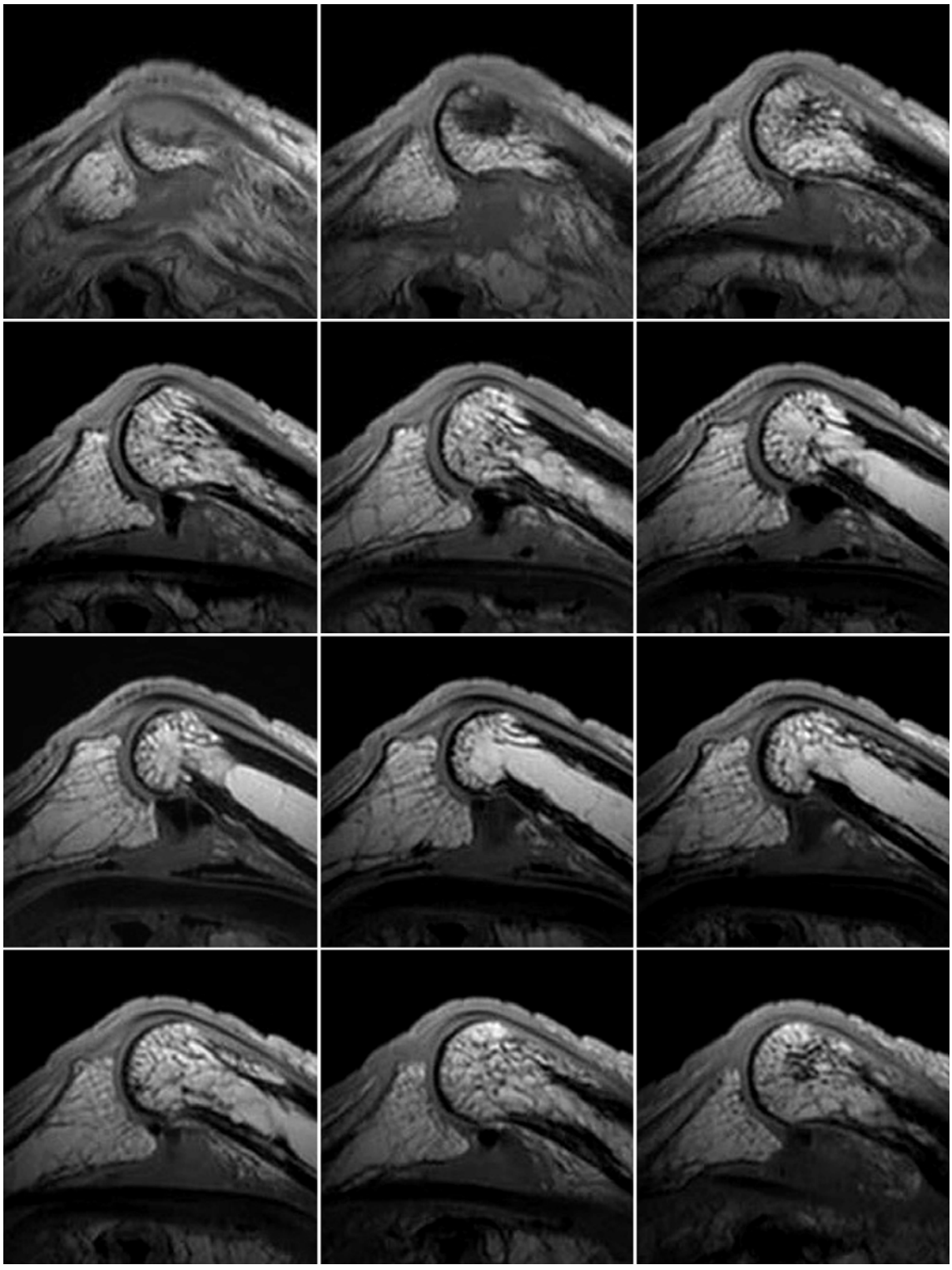

Figure 46. T1 weighted images of the PIP joint with lesion using microscopic coil.

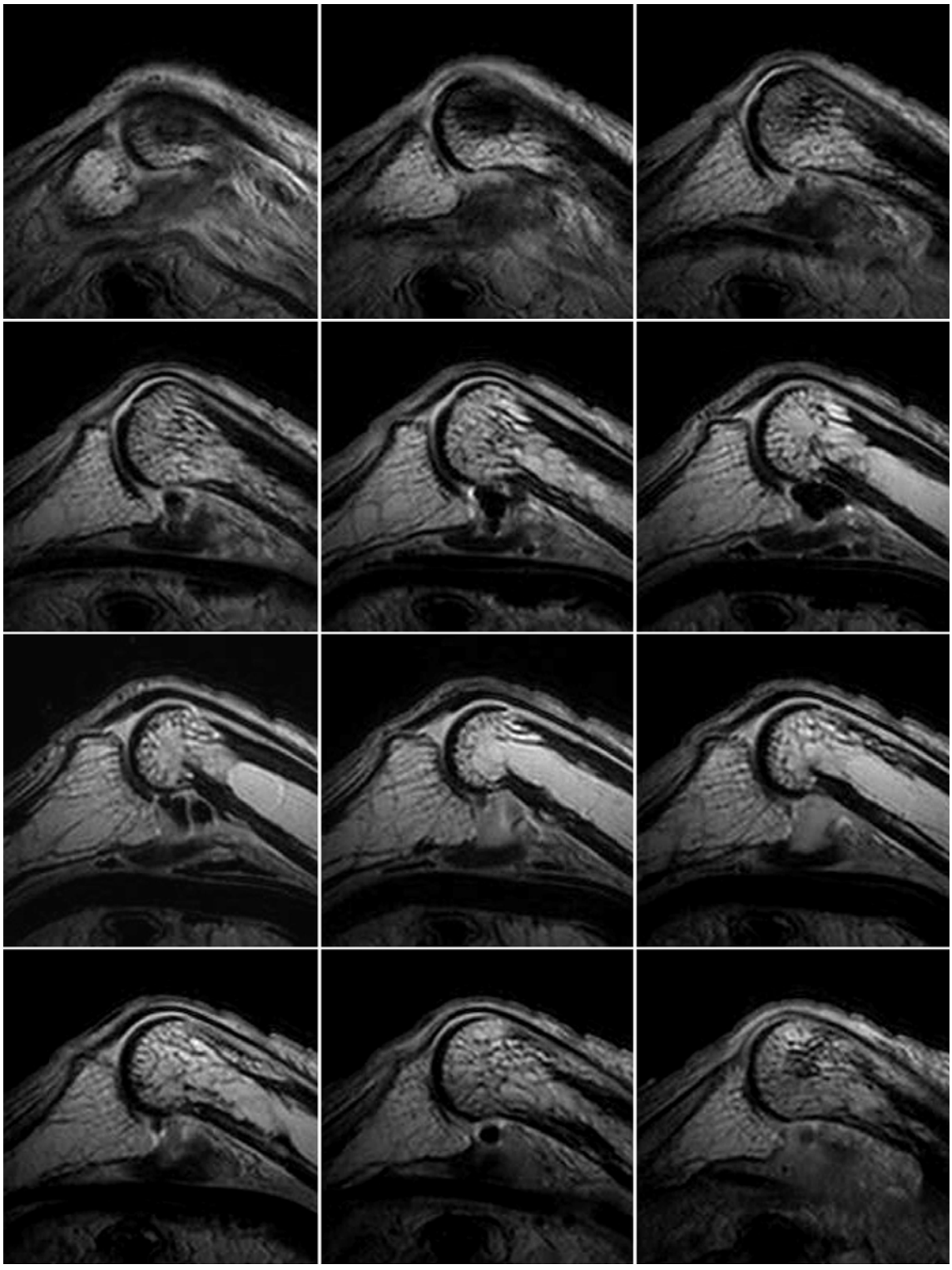

Figure 47. T2 weighted images of the PIP joint with lesion using microscopic coil.

Chapter 7

Discussion

Currently, absorption contrast radiography is mainly used for the detection of joint abnormalities that are accompanied by damages to articular cartilage, such as OA or RA. Cartilage shows little X-ray absorption contrast, however, and diagnosis of joint abnormalities is performed by detecting bone erosion and/or measuring the joint space width on the images [66-75]. This imaging method is sensitive only to advanced cases; early-stage structural abnormalities of cartilage and/or minute bone deformations are not detectable. Therefore, it is essential to develop a technique that can detect substantial cartilage and/or minute bone structure with high spatial resolution. This will then lead to new treatment strategies in early stages of cartilage defects and bone deformation. To this purpose, many researchers have studied the depiction of cartilage using

MRI [76-93], but these methods are still being developed, and there exists a demand for an alternative technique.

In the present study, X-ray DFI was applied to articular cartilage imaging of intact, unsliced objects, without stripping of the skin. The X-ray optics for this method is relatively simple, and imaging is performed using a 2D single-exposure system without line-scanning and/or image processing. This approach enables us to observe the object dynamically under fluoroscopy.

It is appropriate to ask which is better: the image formed on the forward diffracted X-ray or that on the diffracted X-ray. If the spatial resolution of imaging that detects refraction by an object is defined as the minimum distinguishable distance between two structures, then the spatial resolution of X-ray DFI can be estimated as 30 μm, from the result of experiment **4.4.4** (Fig. 41 (a)), using the phantom especially manufactured for this experiment. In comparison, for X-ray BFI, two scratched lines appear completely separated at a distance of approximately 180 μm, as shown in Fig. 41 (b); this is determined from the accompanying white band like contrast on both sides of the line depicted by black band.

Here, let us consider the process of qualitative mechanism of X-ray DFI and BFI at the edge of an object for a simple case. An acrylic plate including an edge structure is assumed, as for the phantom used in experiment **4.4.4**. When the nearly-parallel X-ray beam is incident upon the

object, the beam only deviates significantly at part of the edge and goes out the object. As a result, the beam is deformed to contain a spot composed of locally deviated X-rays. This process is shown schematically in Fig. 48. Provided that the local deviation angle of X-rays in this spot is beyond the Darwin width for an analyzer crystal, and that such X-rays are incident on the crystal, Pendellösung fringe can be observed after the crystal. This process is described as a 'section topograph' by means of a spherical wave of X-rays [114-116]. Because of the low spatial resolution of the detector (X-ray film) used in the present experiment, the X-ray intensity spectrum that forms the fringe is averaged. This process is shown in Fig. 49 schematically. A narrow X-ray beam with a deviation angle beyond the Darwin width for an analyzer crystal is incident on the crystal, as shown in Fig. 49 (a). The beam is diffracted to the forward diffraction and the diffraction directions accompanied by the Borrmann fan. The averaged spatial intensity distributions of forward diffraction and diffraction in the case of $\mu H = 0$ are shown in Figs. 49 (b) and (c), respectively [110]. Note that μH is about 0.2 in the present experimental setup; it is safe to regard μH as being close to 0. Consequently, the images on forward diffraction and diffraction are as shown in Figs. 49 (d) and (e), respectively. The white area corresponds to areas of high X-ray intensity. The white line accompanied by a black band on left side can be seen in the image that shows forward diffraction (Fig. 49 (d)), while a black band accompanied by

a white band on both sides can be seen in that for diffraction (Fig. 49 (e)). The results shown in Fig. 41 are in good agreement with the characteristics obtained from the above discussion. When the image of scratched lines in Fig. 41 (a) is observed in detail, a single scratched line is depicted by two white lines. This phenomenon can be explained as follows. The cross-section of the phantom used in experiment **4.4.4** is enlarged and shown schematically in Fig. 50. Seen in cross-section, the shape of the scratched line forms a V-shape, and is composed of two edges whose distance AB is 60-80 μm, as measured from the photomicrograph. These edges can be detected separately, and are depicted as two sharp white lines, as the spatial resolution of X-ray DFI estimated in section **5.4** is 30 μm. In contrast, the edges cannot be separated in X-ray BFI (Fig. 41 (b)), whose spatial resolution is estimated to be lower than that of X-ray DFI. From the above discussions, X-ray DFI, which provides higher spatial resolution, is better to adopt as clinical imaging. However, we must pay attention to the effect of the black band in X-ray DFI when imaging articular cartilage. If the black band overlaps with the articular cartilage itself, an incorrect diagnosis will be made. As the black band in X-ray DFI appears in the direction of the scattering vector within the Borrmann fan (Fig. 49), it is possible to eliminate this effect. It is important to consider the direction of an object positioned: the object must be positioned such that the black band appears outside the region of articular cartilage of interest. Setting aside the

above consideration, quantitative analysis to investigate the black band contrast that accompanies X-ray DFI is expected in the near future from research that employs computer simulations like refs. [14, 25].

It is appropriate to consider which is better: true X-ray DFI with A(L) set at the just Bragg condition or pseudo X-ray DFI obtained with introducing offset angle to A(L). The optimized offset angle of A(L) will be dependent on the whole shape of the object and the target to be observed. If the argument is narrowed down to articular cartilage at the PIP joint, the different A(L) offset angles provides two different contrasts: 'contour contrast' and 'surface contrast'. Let us assume that X-rays are incident on the boundary of a circular object, as shown in Fig. 8. Equation (14) can be changed to the function of the distance from tangential incident point D. If the conditions are the same as those shown in Fig. 10, the relationship between the deviation angle θ and D is expressed as shown in Fig. 51. Two types of slopes, A and B, exist with an approximate border around D of 25 μm. Slope A has a sudden change of more than 0.1 arcsec of deviation angle θ. Conversely, B has a gentle change of less than 0.1 arcsec of θ. 'Contour contrast' may result from the slope of A and 'surface contrast' from that of B, respectively. These two kinds of contrasts can be observed in Figs. 37-40; the areas of the head of the proximal phalanx in Figs. 37 (a), (b), (f), and (h) are enlarged and shown in Figs. 52 (a), (b), (f) and (h), respectively. Articular cartilage is depicted by 'contour contrast' in Figs. 52

(b) and (h) while by ‘surface contrast’ in Fig. 52 (f). Articular cartilage contours are revealed clearly, and the change of their boundary will be able to be estimated if exists in Figs. 52 (b) and (h). Its surface is depicted clearly and the changes of substance articular cartilage such as erosion or deficit may be observed if exist in Fig. 52 (f). The photograph in Fig. 53 depicts the object with lesions that was used in experiment **4.4.3.2,** and demonstrates the lesions following dissection of the joint. Two defects of articular cartilage can be observed. A and B indicate the two areas of deficit. Figures 39 (a), (b), (f) and (h) are enlarged as in Fig. 52, and are presented in Figs. 54 (a), (b), (f) and (h), respectively. Figures 54 (b) and (h) contain sufficient contrast to reveal the deficits in articular cartilage for areas A and B, shown by a discontinuous line of articular cartilage. Figure 54 (f) in particular reveals the deficits of articular cartilage themselves at areas A and B. Note that the irregular contour of compact bone beneath this area, that is, subchondral bone is also revealed clearly; this findings cannot be detected by MRI even with the use of microscopic coil because no signal can be generated from compact bone. This finding may be a symptom of early-stage arthropathy. Using Fig. 54 (f), surviving articular cartilage and the irregular contour of subchondral bone were painted blue and red, respectively (Fig. 55). In X-ray DFI, there are many interfering fringes superimposed on the central area of bone, inside which there are complicated trabecular bone structures. This prevents depiction of the true

state of bone. So depiction of the bone itself is beyond the scope of this study.

In considering the application of X-ray DFI to the clinical diagnosis of arthropathy, its depiction ability must be compared with that of existing modalities such as X-ray CT, MRI, and ultrasound (US). X-ray CT images are based on absorption contrast and are unable to detect articular cartilage. US has low spatial resolution of approximately 0.5-1.0 mm and is unsuitable for depicting minute structures. MRI is the only candidate that can be compared with X-ray DFI for this purpose. MRI is currently employed for the diagnosis of arthropathy in almost all joints, as articular cartilage of joints such as the knee, hip, ankle, shoulder, and elbow can be clearly depicted. Difficulties exist, however, in depicting the thin articular cartilage of the fingers because of insufficient spatial resolution. Additionally, the finger is difficult to immobilize during scanning and the resulting images often suffer from motion artefact. Imaging times of 3-5 min also contribute to this problem. Furthermore, the fact that MRI cannot detect compact bone may be a fatal flaw in its use as a method for observing the relationship between articular cartilage and subchondral bone for early diagnosis of arthropathy. A photograph of a sliced finger [117] and MRI of a finger (T1 and T2 weighted images) are shown in Figs 56 (a)-(c), respectively. Articular cartilage at the PIP is poorly visible in the T1 weighted image, but there is no signal from compact bone and

subchondral bone in either of the MRI images. High magnetic field MRI systems under development that aim for higher spatial and temporal resolution cannot overcome the lack of signal from bone in MRI. A compact MRI [118] has been developed that is dedicated to imaging the extremities, yet the character of MRI is not changed. These trends may in fact support the significance of the present study.

Let us compare the ability of X-ray DFI to depict the lesion on the articular cartilage on the head of the proximal phalanx with that of T1 weighted MRI image acquired with the microscopic coil in Figs. 57 (a) and (b). In X-ray DFI, both lesions on the articular cartilage (indicated as A and B in Fig. 53) are clearly visible, while only B is visible on MRI; lesion A cannot be identified in other T1 weighted MRI slices. The irregular contour of the subchondral bone can be observed in X-ray DFI but not on MRI. The irregularities may be a feature of early-stage OA or RA. These findings could lead to a new diagnosis strategy for RA.

The exposure dose required for X-ray DFI must be evaluated when considering its clinical application. It is important to compare the dose with that of clinical X-ray imaging, as the X-ray dose to humans in clinical imaging has proved to be historically safe. Table 2 shows the representative entrance surface doses per diagnostic radiograph for each part of the body, as measured in a general hospital in Japan, and guidance levels for medical exposure issued by the International Atomic Energy Agency (IAEA) [119].

Table 3 shows the representative entrance surface doses per examination for fluoroscopy in a general hospital in Japan, and the dose rate guidance levels for fluoroscopy issued by the IAEA [119]. The entrance surface dose is defined as the absorbed dose at the skin surface per unit mass; this enables the values of the examination to be compared. The dose was 0.06 mGy after introduction of an intensifying screen during X-ray DFI of the PIP joint. This value is the entrance surface dose of air. The value of 0.06 mGy must be multiplied by both *f* and *B* (see **4.4.3.1**) when it is compared directly to the values in Table 2 and 3. In the present study, *f* is 0.964 and *B* is 1.16. Finally, the required entrance surface dose for X-ray DFI of the PIP joint is 0.067 mGy. This value may be acceptable for clinical application considering the dose for other examinations, although it delivers more than twice the dose received in conventional imaging of the finger.

Difficulties in obtaining an X-ray source for this imaging must be overcome in order to consider the clinical application of X-ray DFI. Currently this method is only feasible with the use of synchrotron X-rays because the intensity of parallel monochromatic X-rays extracted from a laboratory-based X-ray source is too weak to enable image acquisition within a reasonable exposure time. We consider that synchrotron X-rays are indispensable to X-ray DFI, and await development of a compact synchrotron ring dedicated to clinical use that is under way. If X-ray DFI utilizing synchrotron radiation is realized, it will enable the diagnosis of

early arthropathy. Visualization of minute changes in articular cartilage and/or the irregular surface of subchondral bone will lead to the differential diagnosis of early-stage OA and RA. In the case of RA, early definite diagnosis will enable pharmacotherapy using a biologic agent, such as a cytokine inhibitor, before irreversible damage has occurred. As a result, we would expect a reduction in the number of patients suffering from advanced RA.

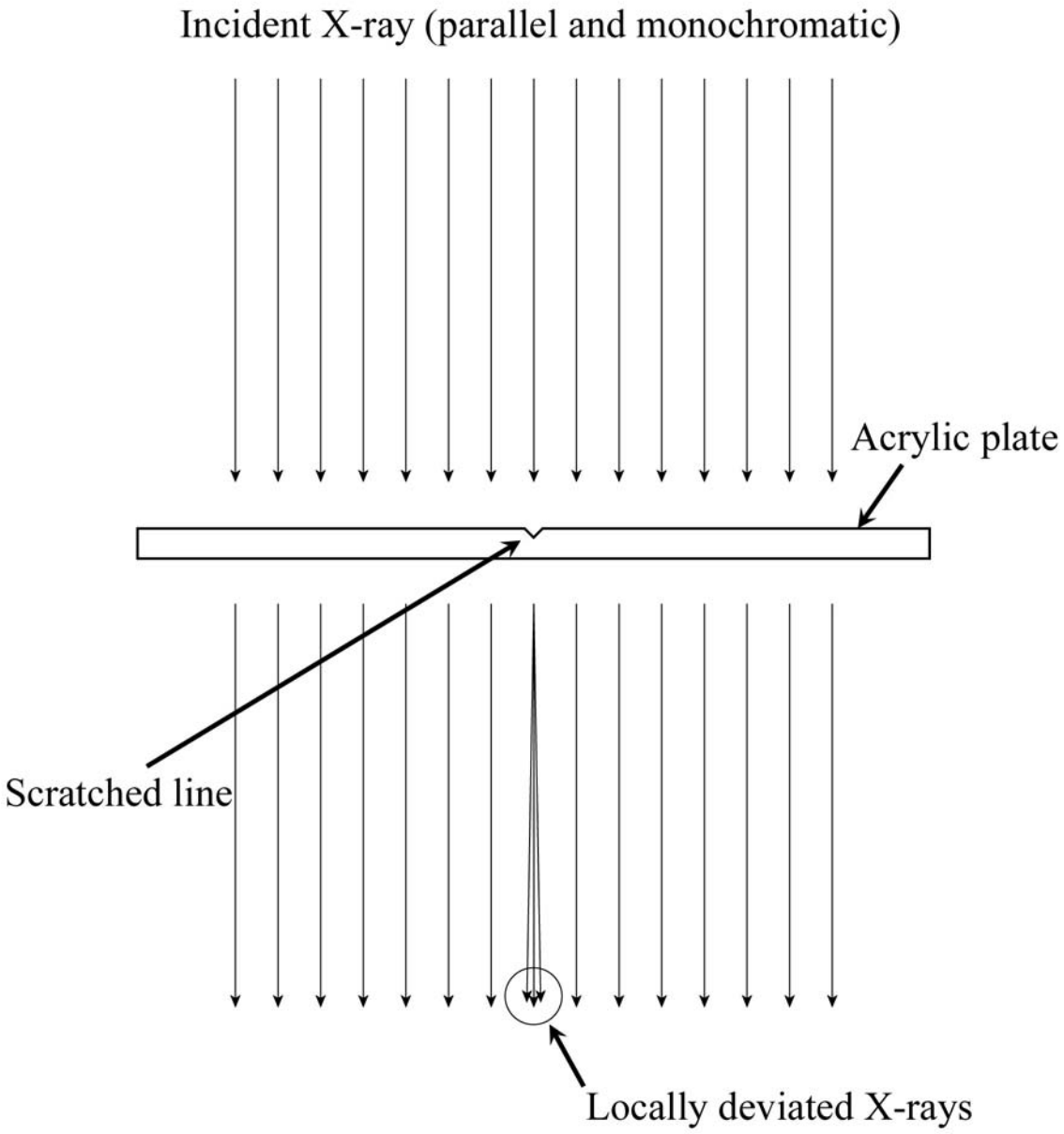

Figure 48. Cross-section of an acrylic plate with scratched line showing the process of beam deformation producing a spot that is composed of locally deviated X-rays.

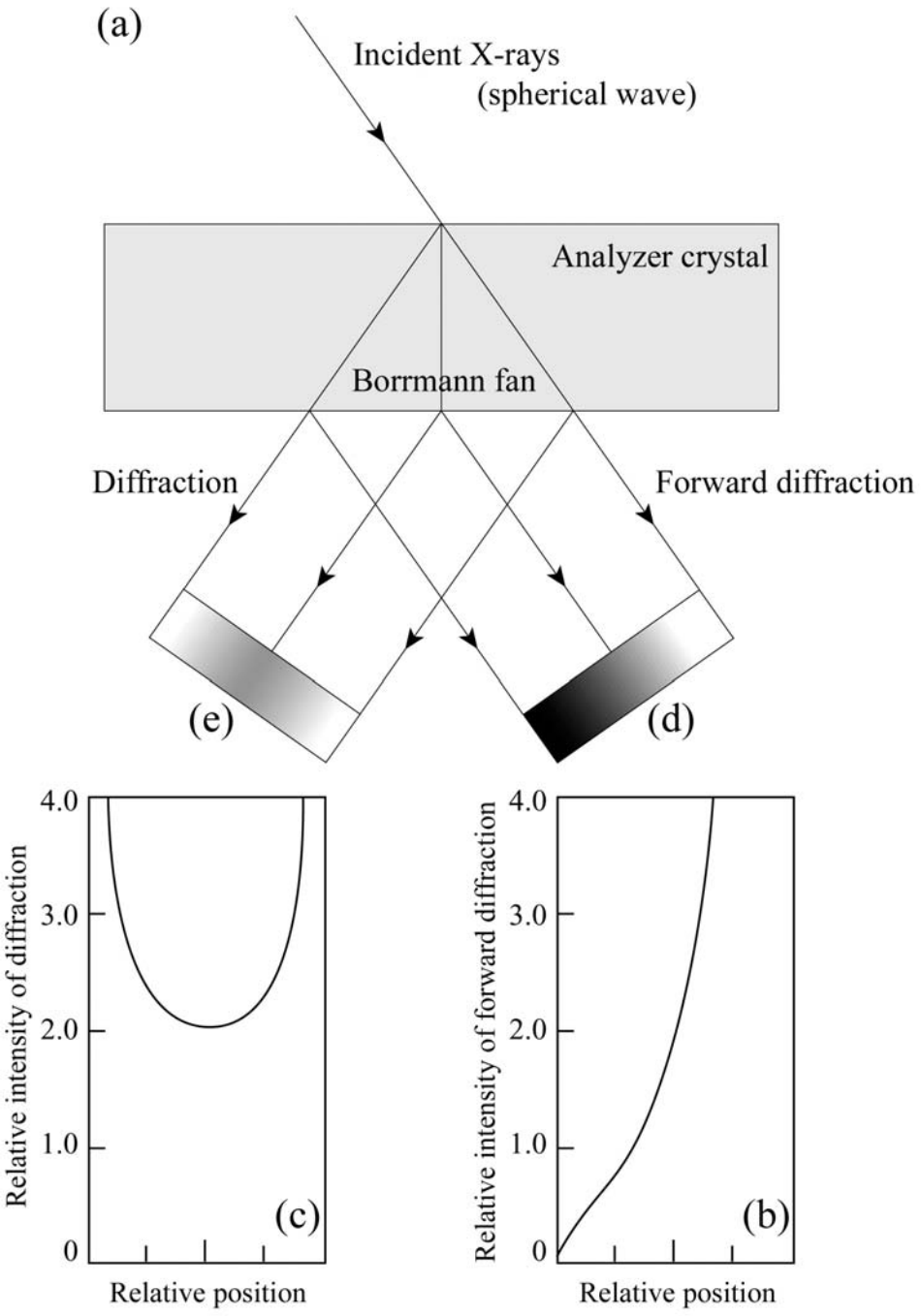

Figure 49. (a): Process of beam (spherical wave) diffraction in the forward diffraction and diffraction directions accompanied by Borrmann fan. (b): Relative intensity profile of forward diffraction. (c): Relative intensity profile of diffraction. (d): Image formed on forward diffraction. (e): Image formed on diffraction.

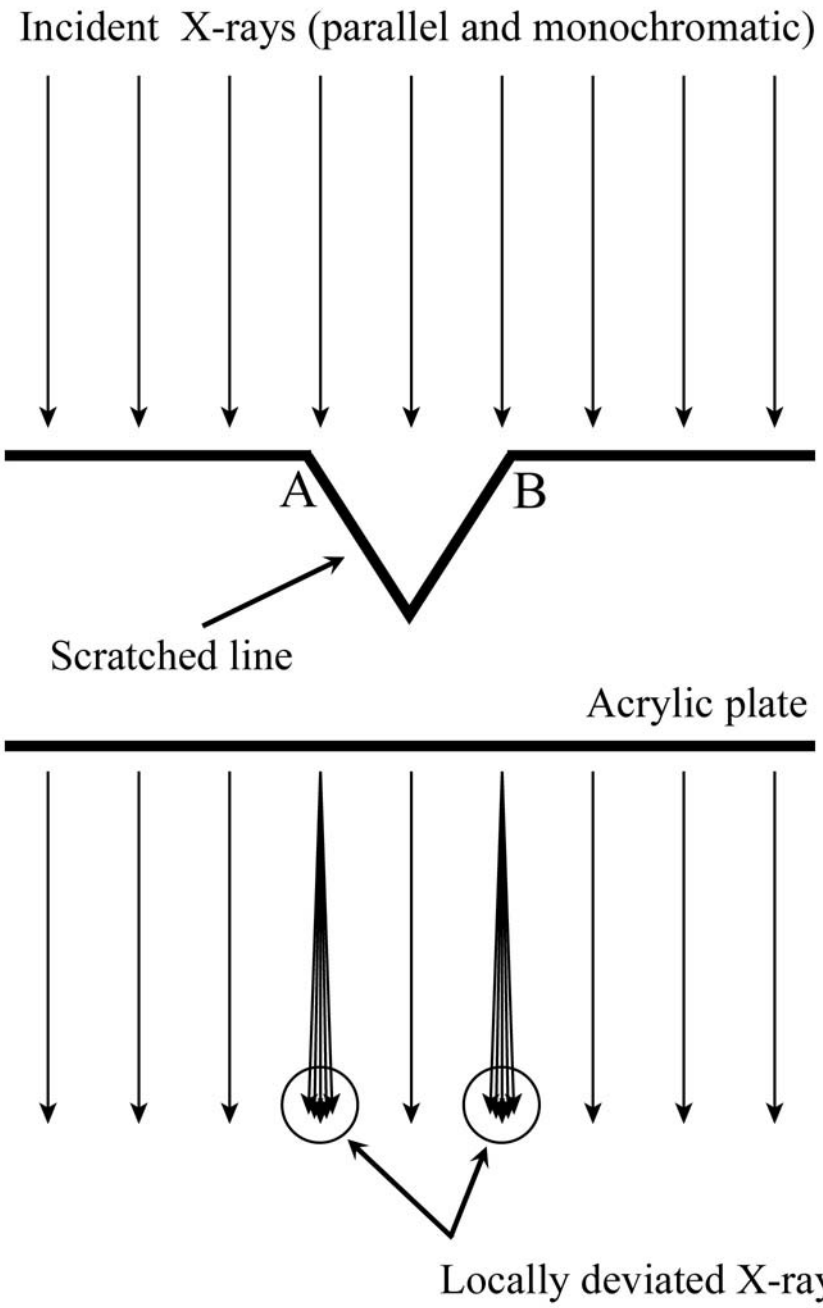

Figure 50. Enlarged cross-section of an acrylic plate with scratched line. Parallel and monochromatic incident X-rays are locally deviated at the edge A and B. The distance between A and B is 60-80 μm.

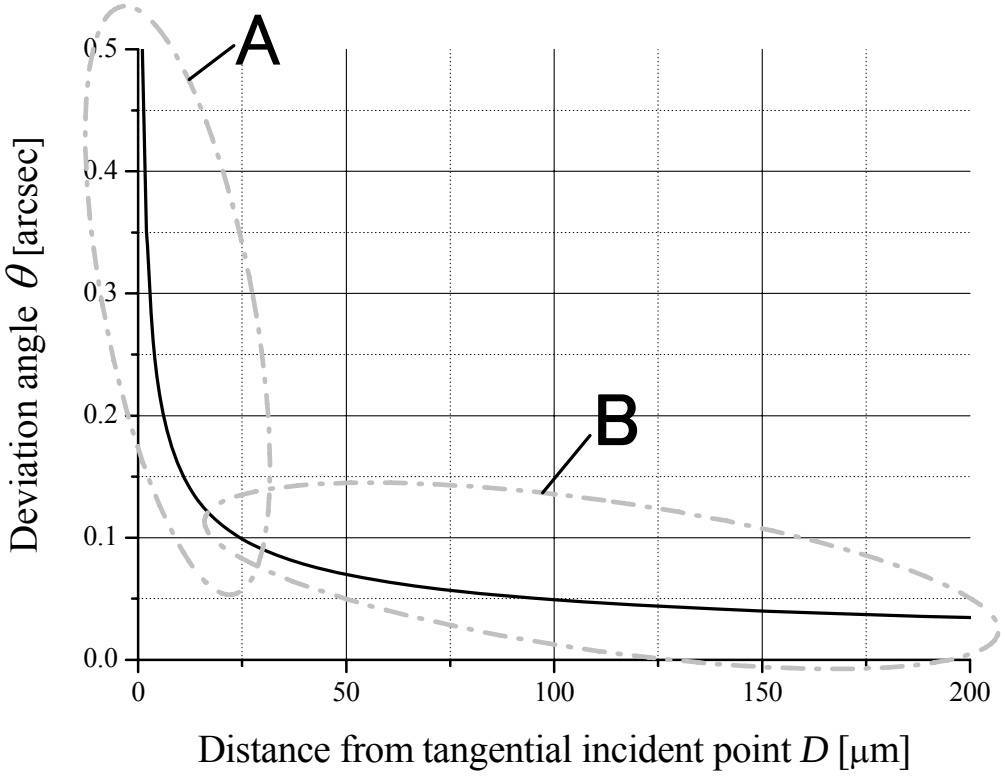

Figure 51. Relationship between deviation angle θ and distance from tangential incident point D.

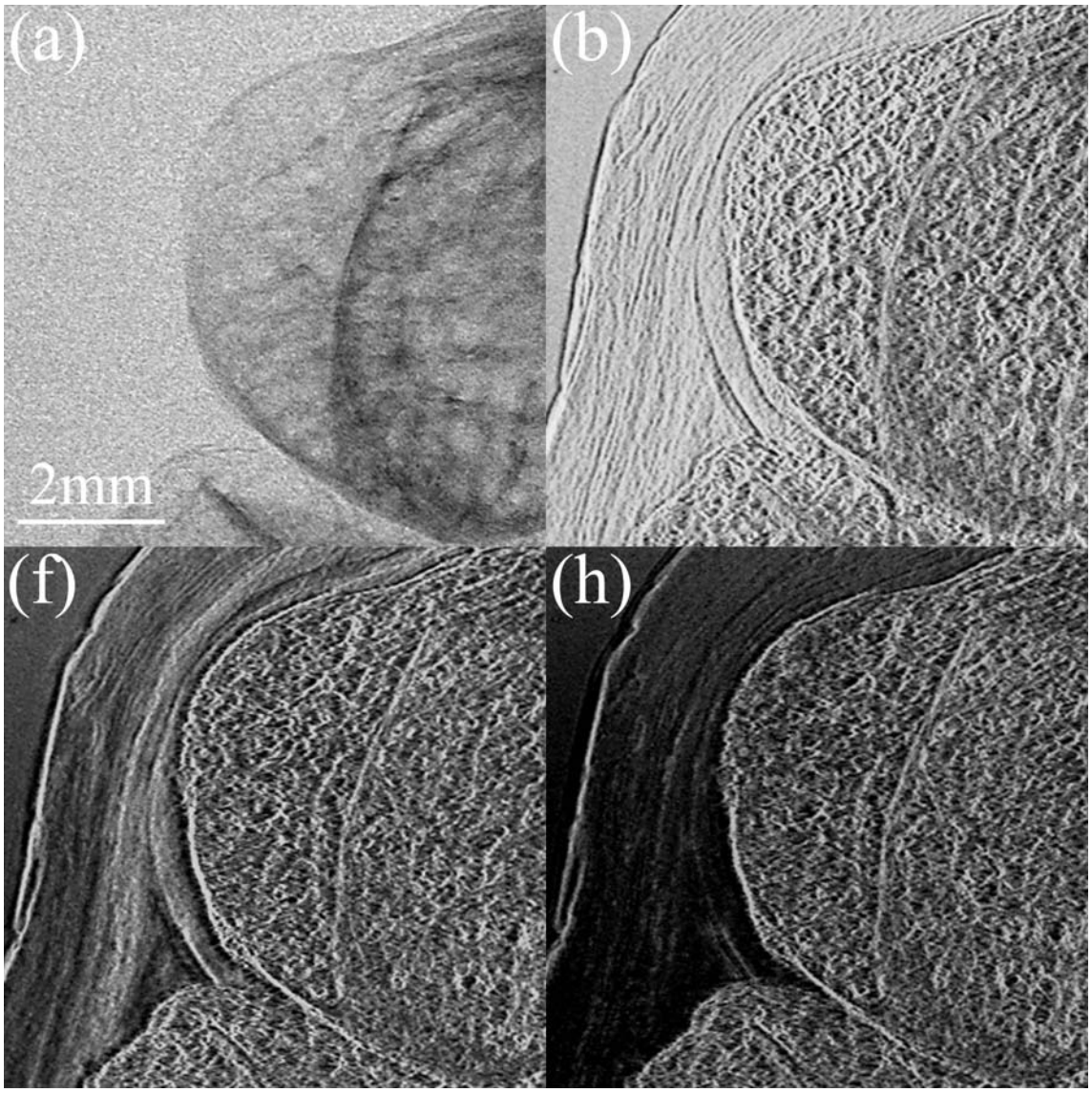

Figure 52. Magnified views of the head of the proximal phalanx shown in Figs. 32 (a), (b), (f), and (h).

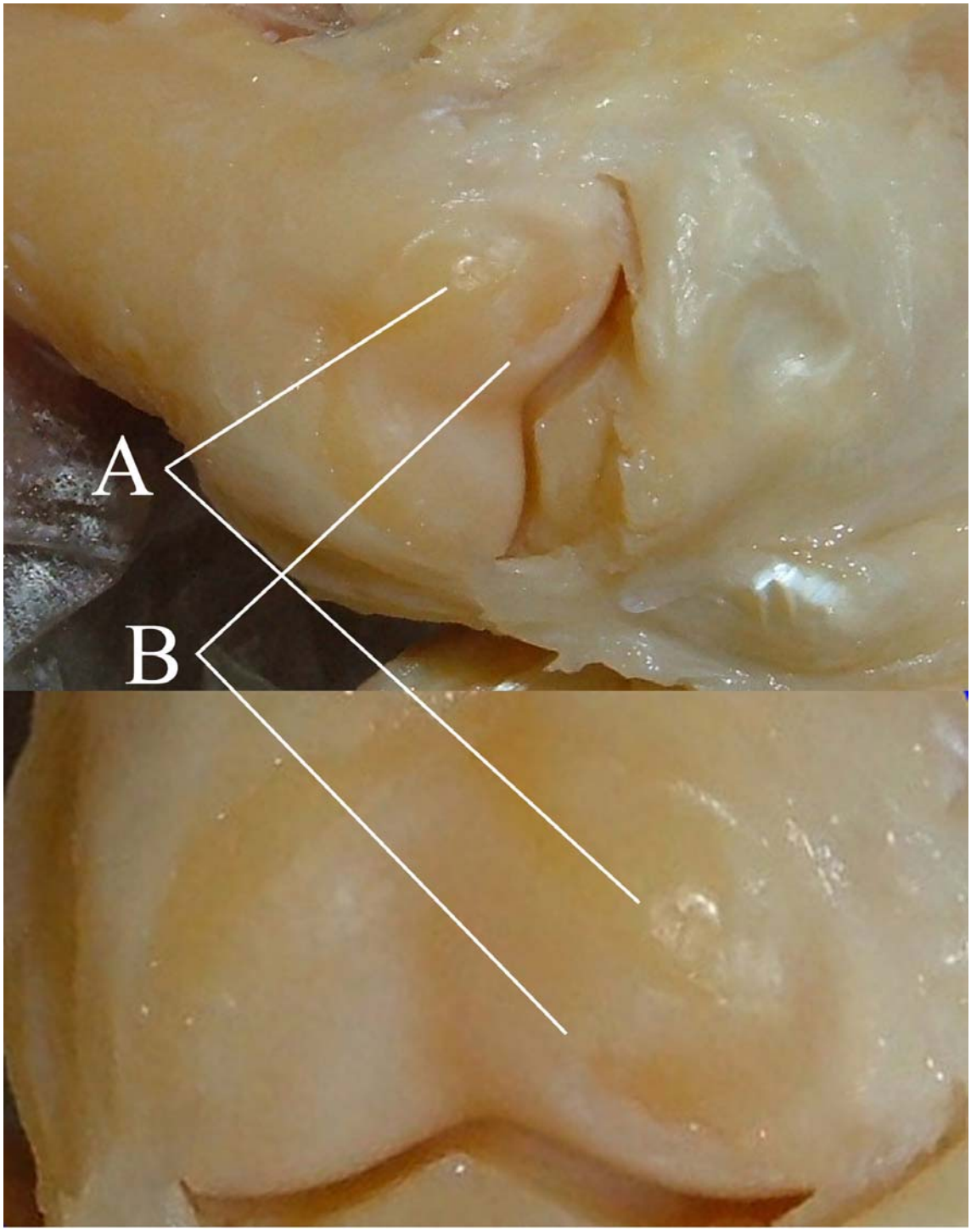

Figure 53. Photographs of the object with lesion used in experiment **4.4.3.2** following dissection.

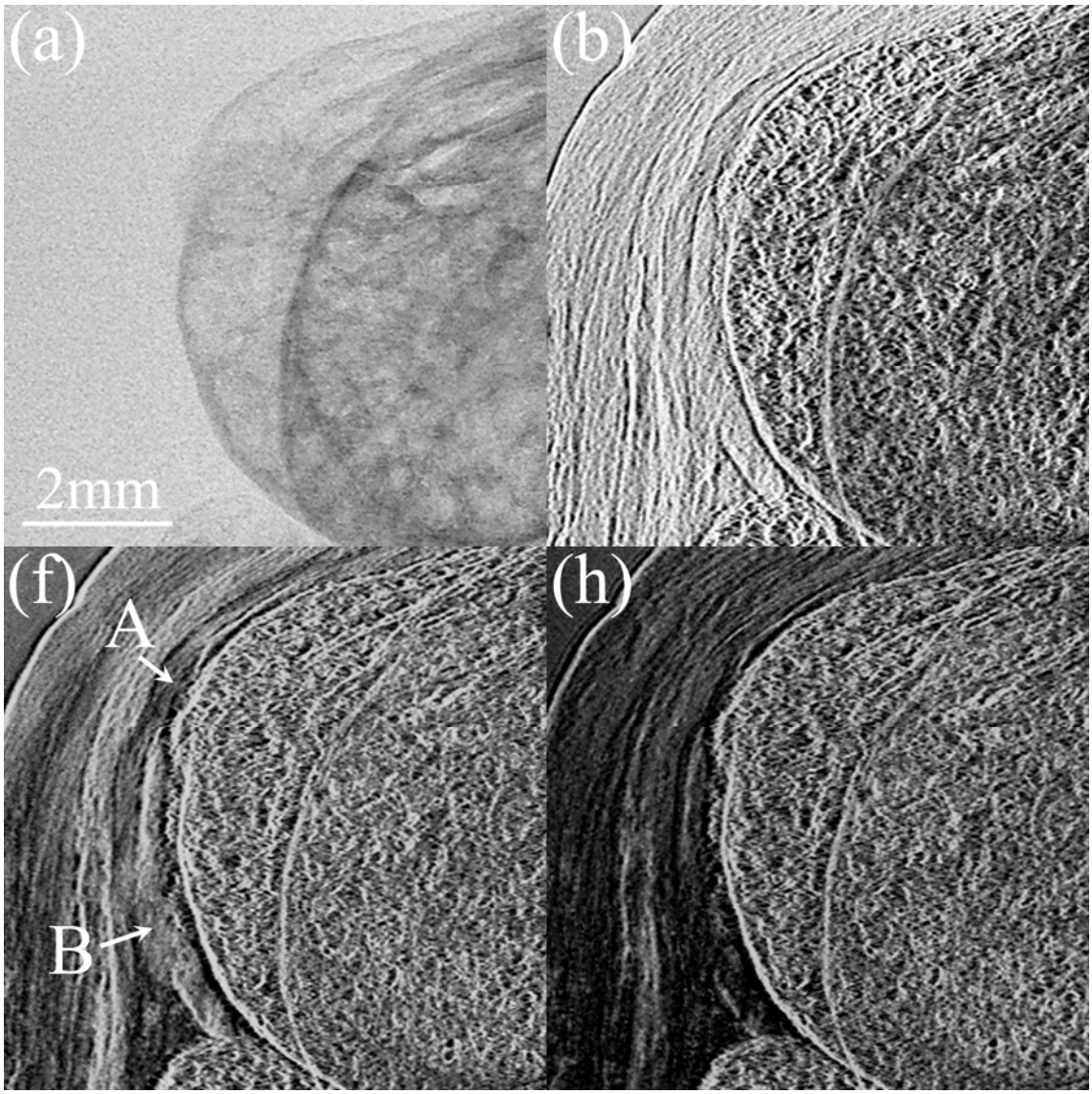

Figure 54. Magnified views of the head of the proximal phalanx shown in Figs. 39 (a), (b), (f), and (h). White arrows A and B correspond to the lesions indicated in Fig. 53.

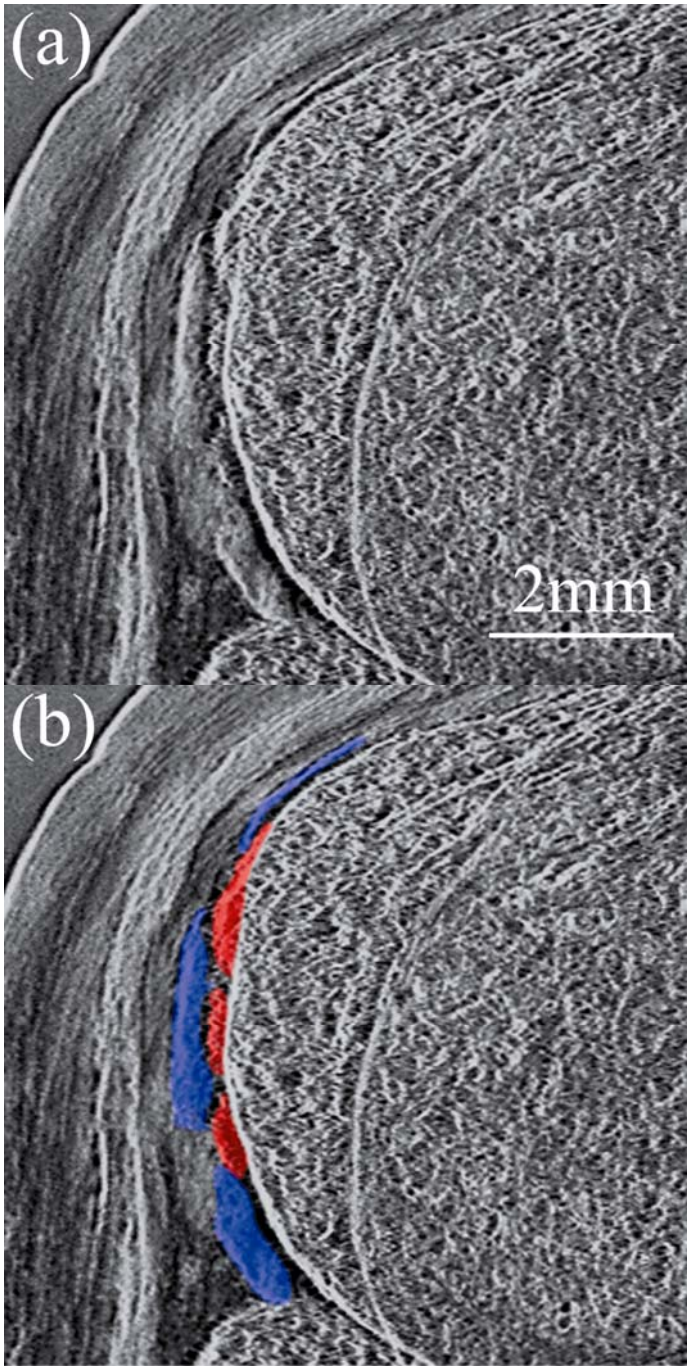

Figure 55. Images with surviving articular cartilage and irregular contour of subchondral bone painted blue and red, respectively: (b). (a) accompanies (b) for the purpose of comparison.

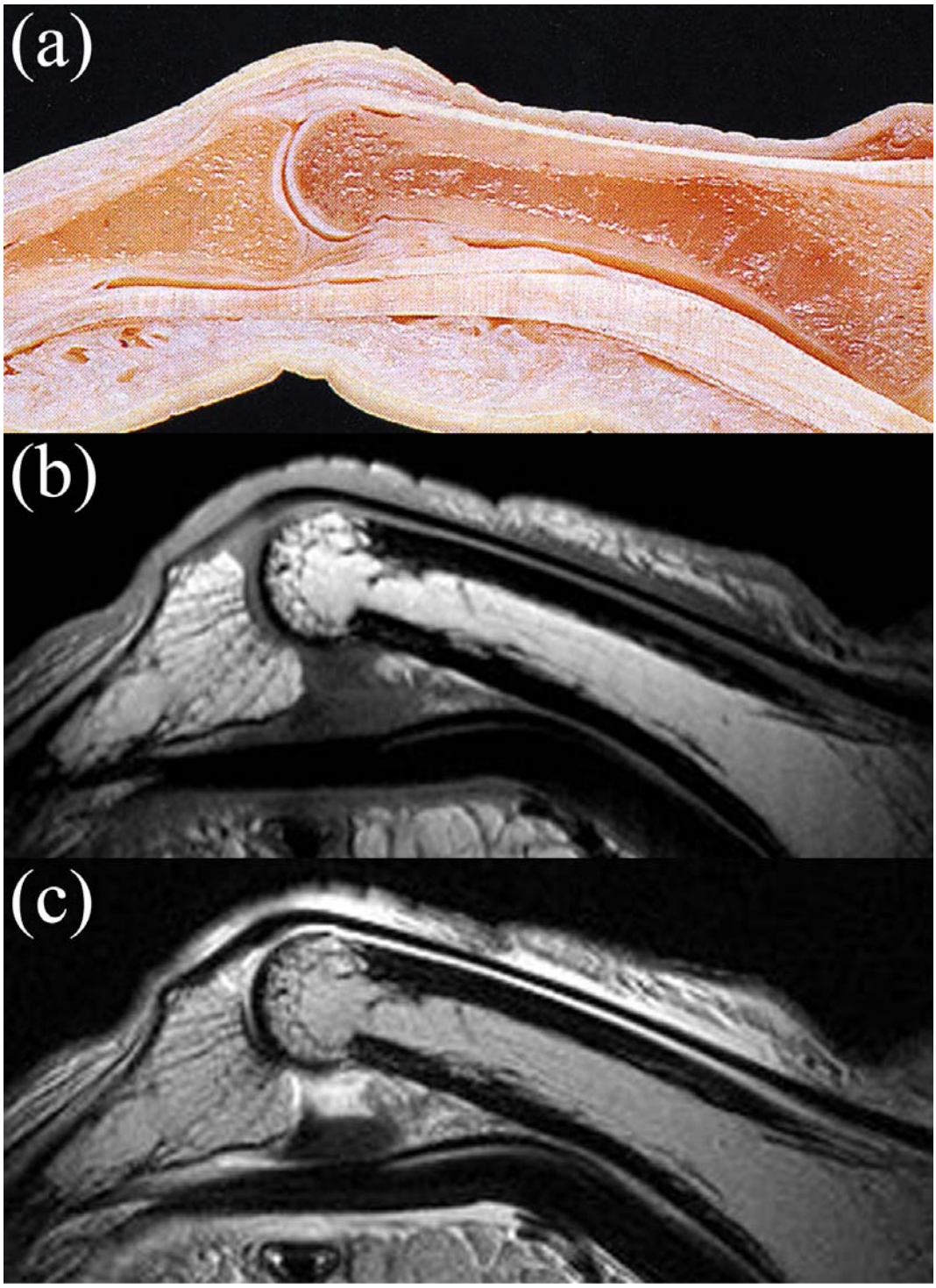

Figure 56. (a): Photograph of a sliced finger. (b): T1 and (c): T2 weighted MRI of finger.

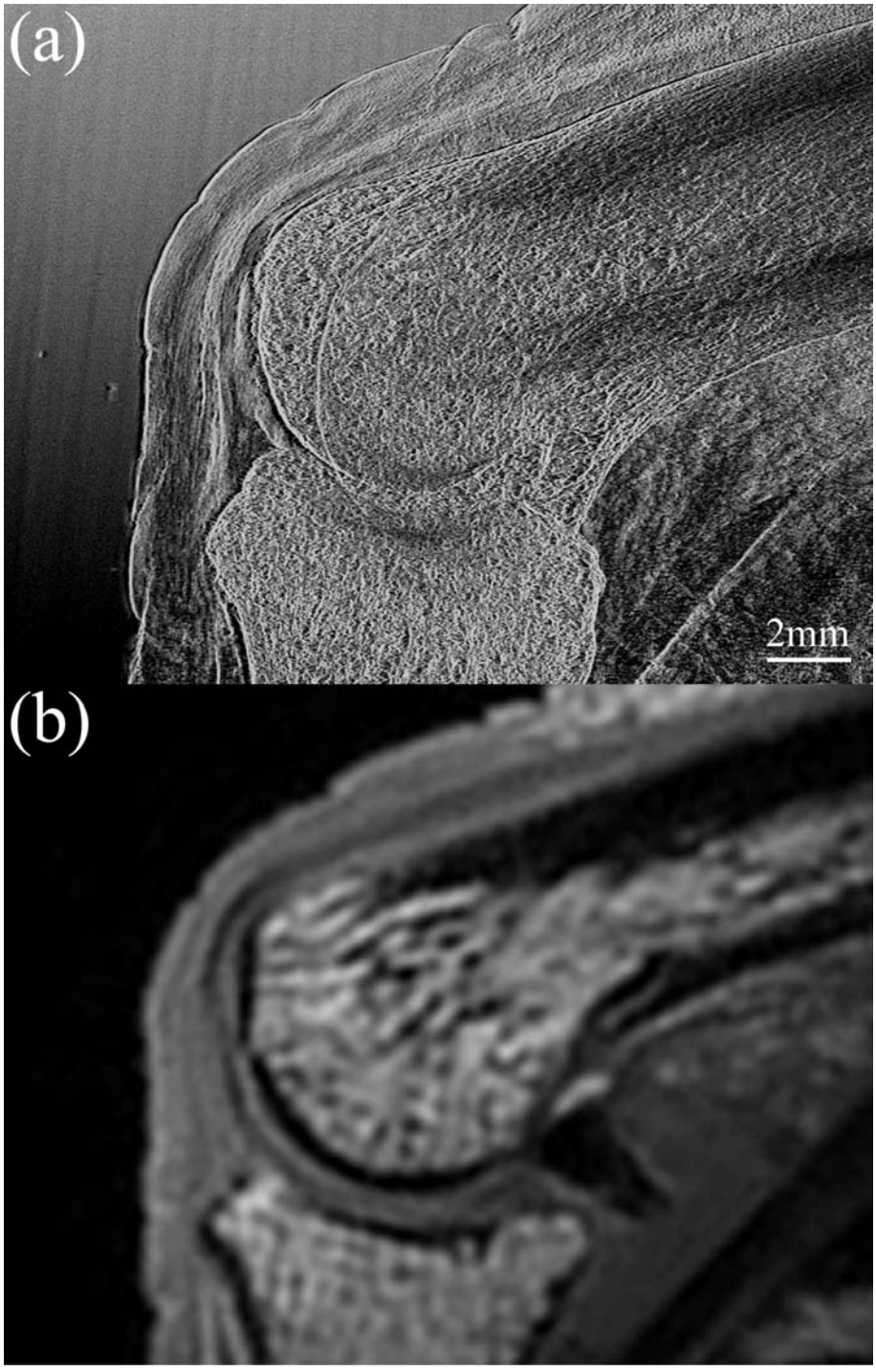

Figure 57. Comparison of (a): X-ray DFI with (b): T1 weighted MRI taken using microscopic coil with regard to the depiction ability for the articular cartilage lesion of the PIP joint.

Examination	Entrance surface Dose per radiograph [mGy] (general hospital in Japan)	IAEA's guidance level of Entrance surface Dose per radiograph [mGy]
Skull	1.18	5
Cervical spine	0.4	
Thoracic spine	2.09	7
Lumber spine	2.09 – 3.93	10
Shoulder	0.47	-
Humerus	0.33	-
Elbow	0.14*	-
Forearm	0.11*	-
Wrist	0.07*	-
Finger, Hand	0.03*	-
Hip joint	1.30 – 2.83	10
Femur	0.82	-
Knee	0.23*	-
Leg	0.23*	-
Ankle	0.17*	-
Foot	0.05*	-
Chest	0.13	0.4
Abdomen	0.92	10

Table 2. Representative entrance surface dose per diagnostic radiographic examination for each part of the body, as from a general hospital in Japan, and guidance levels for medical exposure issued by the International Atomic Energy Agency (IAEA).

Examination	Entrance surface Dose per examination [mGy] (general hospital in Japan)	IAEA's guidance level of Entrance surface Dose rate [mGy/min]
Upper GI series	0.21 – 8.38	(Normal operation mode) 25 (High level operation mode) 100
Contrast enema	1.05 – 8.38	
Cerebral angiography	6.24 – 28.3	
Coronary angiography	14.3 – 21.2	

Table 3. Representative entrance surface dose for fluoroscopy from a general hospital in Japan, and dose rate guidance levels for fluoroscopy issued by the IAEA.

Chapter 8

Concluding Remarks

The early diagnosis and treatment of RA is desired because RA tends to disseminate to joints throughout the entire body and reduces the QOL of patients as it progresses. Currently, X-ray absorption contrast radiography is mainly utilized in the image diagnosis of RA. This imaging method can depict only the bone structure, and RA is diagnosed from obvious bone erosion and/or joint space narrowing that are indirect markers of articular cartilage degeneration: abnormalities are detected only after they have progressed. In the current study, X-ray DFI was applied to arthropathy as a new imaging method for the detection of minute changes in articular cartilage and the subchondral bone surface. Human fingers were selected as imaging objects because they are one of the most common locations of RA. Synchrotron X-rays of around 35 keV were used to study

the potential of X-ray DFI for clinical application.

The main findings of this study are as follows:

(1) X-ray DFI can successfully depict articular cartilage located in an intact object; this is invisible on X-ray absorption contrast radiography.

(2) The object must be immersed in water for X-ray DFI to eliminate contrast from skin wrinkles that is superimposed on contrast from inner structures.

(3) The spatial resolution of X-ray DFI is approximately 30 μm, which is higher than that of X-ray BFI. The resolution was measured using a phantom prepared especially for this study.

(4) The effect of the black band-like contrast accompanied by main contrast tends to reduce the spatial resolution of X-ray DFI, and must be taken into account when positioning an object. There exists the possibility that this effect will result in an incorrect diagnosis.

(5) It is estimated that X-ray beam divergences by soft tissue and bone are 0.1 arcsec and 0.5 arcsec, respectively, under the conditions of this study.

(6) There are two kinds of image contrast: ‘contour contrast’ and ‘surface contrast’. ‘Contour contrast’ is acquired by true X-ray DFI and pseudo X-ray DFIs with the introduction of offset angles to higher and relatively large offset angles to lower angular positions of the A(L).

‘Surface contrast’ is acquired by pseudo X-ray DFI with the introduction of a slight offset angle to a lower angular position of the A(L).

(7) ‘Surface contrast’ is suitable for observing articular cartilage itself. It will be necessary to observe the image of an object under 2D fluoroscopy in order to grasp the best offset angle of the A(L) for the demonstration of ‘surface contrast’. Contrast depends on the internal structure of an object and differences in refractive index within the object.

(8) Defects in the articular cartilage in an object can be depicted clearly by pseudo X-ray DFI that utilizes ‘surface contrast’. Minute irregular surface of subchondral bone is also depicted clearly using this method.

(9) The exposure dose is reduced to 0.06 mGy (exposure time: 3 sec) by the introduction of a film/screen system that provides the same findings as that of a non-screen system, with a reduction in spatial resolution to 80-90 μm. This dose is comparable to the dose received in current clinical X-ray imaging.

(10) Minute irregular contours of subchondral bone can be observed on X-ray DFI, whereas no signal can be detected from subchondral bone on MRI. This finding may indicate an aspect of early-stage arthropathy that is previously unknown.

(11) X-ray DFI will be a powerful tool for the diagnosis of arthropathy, as

minute changes in articular cartilage and/or irregularities of subchondral bone may be features of the early stage of the disease. This finding may enable a new strategy for diagnosis.

In conclusion, X-ray DFI is useful for the early detection of abnormalities associated with arthropathy. In practice, it is necessary to monitor the images by rocking the A(L) around the just Bragg condition under fluoroscopy to obtain the best image for observing articular cartilage, as there exist individual variations in the form of the PIP joint. This technique is similar to that employed for upper GI series, contrast enema, and ultrasonographic scanning. The present study indicates that X-ray DFI with a slight offset angle introduced to the A(L) produces a superior image for the observation of lesions on articular cartilage, although it is difficult to predict the ideal angular position of the A(L). These depiction abilities may enable us to clarify the changes in articular cartilage that occur in the early stages of OA and RA. If early degenerative changes can be detected before the point of irreversible damage, it will be possible to reduce the number of patients who suffer from joint disease.

Acknowledgements

During the completion of this doctoral thesis, I received a lot of scientific and personal help from different people around me. If it had not been for their help, this work would never have been completed. Here I would like to express my thanks to those people.

Scientific thanks

First of all, I would like to say many thanks to my academic supervisor Prof. **Masami ANDO**. His wise supervision during the three years spent on this work enable me to accomplish the research for this thesis. At the same time, he helped me to acquire an international way of thinking, giving me the opportunity to present my results of this work at international conferences and lectures abroad. The number of these international trips totaled 5 (San Francisco, USA; Trieste, Italy; San Diego, USA; Hsinchu, Taiwan; Shanghai, China). These experiences surely served

as a stimulus to progress with my research.

Another person who helped me very mush was Dr. **Hiroshi SUGIYAMA**, an expert on X-ray optics. The experimental data presented in this work wouldn't have been acquired without his perfect support. I would like to express my thanks to him for his many bright ideas and helpful techniques that helped me to accomplish the experiments.

Precious samples were provided by Dr. **Toshiyuki KUNISADA**. Had it not been for his understanding toward this pioneering work, I wouldn't have acquired clinically useful data. Here, I would like to express my thanks to him.

I would also like to express my thanks to Dr. **Kazuyuki HYODO** (Head of beamline BL14C1) and Dr. **Keiichi HIRANO** (Head of beamline BL14B) for assistance in performing the experiments. I am also grateful to Dr. **Xiaowei ZHANG** and Prof. **Koichi MORI** for many useful opinions concerning the experimental results.

Personal thanks

Here, I would like to acknowledge my wife **Takako SHIMAO**. Her tolerance and understanding were of great importance to the continuation and completion of this work. I would also like to express my appreciation, from my bottom of my heart, for her mental and economic support during the completion of this thesis.

References

1) Bonse U. and Hart M. An X-ray Interferometer. *Applied Physics Letters.* 6: 155-156, 1965.

2) Bonse U. and Hart M. An X-ray Interferometer with Long Separated Interfering Beam Paths. *Applied Physics Letters.* 7: 99-100, 1965.

3) Ando M. and Hosoya S. An Attempt at X-ray Phase-Contrast Microscopy. *Proceedings of 6th International Conference on X-ray Optics & Microanalysis.* 63-68, 1972.

4) Davis TJ., Gao D., Gureyev TE., Stevenson AW. and Wilkins SW. Phase-contrast imaging of weakly absorbing materials using hard X-rays. *Nature.* 373: 595-598, 1995.

5) Davis TJ., Gureyev TE., Gao D., Stevenson AW. and Wilkins SW. X-ray Image Contrast from a Simple Phase Object. *Physical Review Letters.* 74: 3173-3176, 1995.

6) Ingal VN. and Beliaevskaya EA.. X-ray plane-wave topography observation of the phase contrast from a non-crystalline object. *Journal of Physics D: Applied Physics.* 28: 2314-2317, 1995.

7) Snigirev A., Snigireva I., Kohn V., Kuznetsov S. and Schelokov I. On the possibilities of x-ray phase contrast microimaging by coherent high-energy synchrotron radiation. *Review of Scientific Instruments.* 66: 5486-5492, 1995.

8) Cloetens P., Barrett R., Baruchel J., Guigay JP. and Schlenker M. Phase objects in synchrotron radiation hard x-ray imaging. *Journal of Physics D: Applied Physics.* 29: 133-146, 1996.

9) Raven C., Snigirev A., Snigireva I., Spanne P., Souvorov A. and Kohn V. Phase-contrast microtomography with coherent high-energy synchrotron x rays. *Applied Physics Letters.* 69: 1826-1828, 1996.

10) Wilkins SW., Gureyev TE., Gao D., Pogany A. and Stevenson AW. Phase-contrast imaging using polychromatic hard X-rays. *Nature.* 384: 335-338, 1996.

11) Pogany A., Gao D. and Wilkins SW. Contrast and resolution in imaging with a microfocus x-ray source. *Review of Scientific Instruments.* 68: 2774-2782, 1997.

12) Chapman D., Thomlinson W., Johnston RE., Washburn D., Pisano E., Gmur N., Zhong Z., Menk R., Arfelli F. and Sayers D. Diffraction enhanced x-ray imaging. *Physics in Medicine and Biology.* 42: 2015-2025, 1997.

13) Gureyev TE. and Wilkins SW. On X-ray phase retrieval from polychromatic images. *Optics Communications.* 147: 229-232, 1998.

14) Margaritondo G. and Tromba G. Coherence-based edge diffraction sharpening of x-ray images: A simple model. *Journal of Applied Physics.* 85: 3406-3408, 1999.

15) Hwu Y., Hsieh HH., Lu MJ., Tsai WL., Lin HM., Goh WC., Lai B., Je JH., Kim CK., Noh DY., Youn HS., Tromba G. and Margaritondo G. Coherence-enhanced synchrotron radiology: Refraction versus diffraction mechanisms. *Journal of Applied Physics.* 86: 4613-4618, 1999.

16) Momose A., Takeda T. and Itai Y. Phase-contrast X-ray computed tomography for biological imaging. *Proceedings of SPIE.* 3149: 120-129, 1997.

17) Hirano K. and Momose A. Development of an X-ray Interferometer for High-Resolution Phase-Contrast X-ray Imaging. *Japanese Journal of Applied Physics.* 38: L1556-L1558, 1999.

18) Ando M., Chen J., Hyodo K., Mori K., Sugiyama H., Xian D. and Zhang X. Nondestructive Visual Search for Fossils in Rock Using X-ray Interferometry Imaging. *Japanese Journal of Applied Physics.* 39: L1009-L1011, 2000.

19) Wang Y., Xiao T. and Xu H. Effect of surface roughness on the spatial coherence of X-ray beams from third-generation synchrotron radiation sources. *Journal of Synchrotron Radiation.* 7: 209-214, 2000.

20) Ishisaka A., Ohara H. and Honda C. A New Method of Analyzing Edge Effect in Phase Contrast Imaging with Incoherent X-rays. *Optical Review.* 7: 566-572, 2000.

21) Ando M., Sugiyama H., Maksimenko A., Pattanasiriwisawa W., Hyodo K. and Zhang X. A new optics for Dark-field imaging in X-ray region ‘Owl’. *Japanese Journal of Applied Physics.* 40: L844-L846, 2001.

22) Ando M. and Sugiyama H. X-ray trichromator ‘Trinity’ and X-ray

dark field camera ‘Owl’. *The Rigaku-Denki Journal.* 32: 16-27, 2001.

23) Ando M., Hyodo K., Sugiyama H., Maksimenko A., Pattanasiriwisawa W., Mori K., Roberson J., Rubenstein E., Tanaka Y., Chen J., Xian D. and Zhang X. X-ray optics ‘Owl’ and ‘Trinity’. *Japanese Journal of Applied Physics.* 41: 4742-4749, 2002.

24) Hirano K., Maksimenko A., Sugiyama H. and Ando M. X-ray Optics for Observing Dark-Field and Bright-Field Refraction-Contrast Images. *Japanese Journal of Applied Physics.* 41: L595-L598, 2002.

25) Kiss MZ., Sayers DE. and Zhong Z. Measurement of image contrast using diffraction enhanced imaging. *Physics in Medicine and Biology.* 48: 325-340, 2003.

26) Hirano K. Angle-resolved x-ray imaging using a resolution-tunable double-crystal analyzer. *Journal of Physics D: Applied Physics.* 36: 1469-1472, 2003.

27) Oltulu O., Zhong Z., Hasnah M., Wernick MN. and Chapman D. Extraction of extinction, refraction and absorption properties in diffraction enhanced imaging. *Journal of Physics D: Applied Physics.* 36: 2152-2156, 2003.

28) Maksimenko A., Ando M., Sugiyama H., Pattanasiriwisawa W. and Hyodo K. A Test of an X-ray Quatrochrome Interferometer for Simultaneous Observation of Images Due to Dark- and Bright-Field, Phase-Interference and Absorption Contrasts. *Japanese Journal of Applied Physics.* 42: L1096-L1099, 2003.

29) Maksimenko A., Sugiyama H., Hirano K., Yuasa T. and Ando M. Dark-field imaging using an asymmetric Bragg case transmission analyzer. *Measurement Science & Technology.* 15: 1251-1254, 2004.

30) Takeda T., Momose A., Itai Y., Wu J. and Hirano K. Phase-Contrast Imaging with Synchrotron X-ray for Detecting Cancer Lesions. *Academic Radiology.* 2: 799-803, 1995.

31) Ingal VN., Beliaevskaya EA., Brianskaya AP. and Merkurieva RD. Phase mammography – a new technique for breast investigation. *Physics in Medicine and Biology.* 43: 2555-2567, 1998.

32) Spanne P., Raven., Snigireva I. and Snigirev A. In-line holography and phase-contrast microtomography with high energy x-rays. *Physics in Medicine and Biology.* 44: 741-749, 1999.

33) Mori K., Hyodo K., Shikano N. and Ando M. First Observation of Small Fractures on a Human Dried Proximal Phalanx by Synchrotron X-ray Interference Radiography. *Japanese Journal of Applied Physics.* 38: L1339-L1341, 1999.

34) Arfelli F., Bonvicini V., Bravin A., Cantatore G., Castelli E., Palma LD., Di Michiel M., Fabrizioli M., Longo R., Menk RH., Olivo A., Pani S., Pontoni D., Poropat P., Prest M., Rashevsky A., Ratti M., Rigon L., Tromba G., Vacchi A., Vallazza E and Zanconati F. Mammography with Synchrotron Radiation: Phase-Detection Techniques. *Radiology*. 215: 286-293, 2000.

35) Momose A., Takeda T. and Itai Y. Blood Vessels: Depiction at Phase-Contrast X-ray Imaging without Contrast Agents in the Mouse and Rat – Feasibility Study. *Radiology.* 217: 593-596, 2000.

36) Takeda K., Momose A., Yu Q., Wu J., Hirano K. and Itai Y. Phase-contrast X-ray imaging with a large monolithic X-ray interferometer. *Journal of Synchrotron Radiation.* 7: 280-282, 2000.

37) Mori K., Sato H., Sekine N., Shikano N., Sato M., Shimao D., Igarashi T., Shiwaku H. and Hyodo K. Development of Phase

Contrast Radiography for Bone Imaging Using Synchrotron Radiation. *Analytical sciences 2001 Supplement.* 17: i1427-i1430, 2001.

38) Zhong Z., Chapman D., Connor D., Dilmanian A., Gmur N., Hasnah M., Johnston RE., Kiss MZ., Li J., Muehleman C., Oltulu O., Parham C., Pisano E., Rigon L., Sayers D., Thomlinson W., Yaffe M. and Zhong H. Diffraction Enhanced Imaging of Soft Tissue. *Synchrotron Radiation News.* 15: 27-34, 2002.

39) Mollenhauer J., Aurich ME., Zhong Z., Muehleman C., Cole AA., Hasnah M., Oltulu O., Kuettner KE., Margulis A., Chapman LD. Diffraction-enhanced X-ray imaging of articular cartilage. *Osteoarthritis and Cartilage.* 10: 163-171, 2002.

40) Momose A. Phase-contrast X-ray imaging based on interferometry. *Journal of Synchrotron Radiation.* 9: 136-142, 2002.

41) Mori K., Sekine N., Sato H., Shimao D., Shiwaku H., Hyodo K., Sugiyama H., Ando M., Ohashi K., Koyama M. and Nakajima Y. Application of synchrotron X-ray imaging to phase objects in orthopedics. *Journal of Synchrotron Radiation.* 9: 143-147, 2002.

42) Suzuki Y., Yagi N. and Uesugi K. X-ray refraction-enhanced imaging and a method for phase retrieval for a simple object. *Journal of Synchrotron Radiation.* 9: 160-165, 2002.

43) Mori K., Sekine N., Sato H., Shikano N., Shimao D., Shiwaku H., Hyodo K. and Ohashi K. First Observation of a Wooden Foreign Body in Soft Palate by Means of Synchrotron X-Ray Refraction Contrast. *Japanese Journal of Applied Physics.* 41: 5490-5491, 2002.

44) Li J., Zhong Z., Lidtke R., Kuettner E., Peterfy C., Aliyeva E. and Muehleman C. Radiography of soft tissue of the foot and ankle with diffraction enhanced imaging. *Journal of Anatomy.* 202: 463-470,

2003.

45) Shimao D., Mori K., Sugiyama H. and Hyodo K. Imaging of Ligament and Articular Cartilage Due to Refraction-Contrast Using a Laue Geometry Analyzer Crystal. *Japanese Journal of Applied physics.* 42: 5874-5875, 2003.

46) Lewis RA., Hall CJ., Hufton AP., Evans S., Menk RH., Arfelli F., Rigon L., Tromba G., Dance DR., Ellis IO., Evans A., Jacobs E., Pinder SE. and Rogers KD. X-ray refraction effects: application to the imaging of biological tissues. *The British Journal of Radiology.* 76: 301-308, 2003.

47) Shimao D., Mori K., Hyodo K., Sugiyama H. and Ando M. Application of X-ray Refraction-Contrast to Medical Joint Imaging. *Proceedings of SRI 2003.* 1324-1327, 2004.

48) Ando M., Sugiyama H., Maksimenko A., Rubenstein E., Roberson J., Shimao D., Hashimoto E. and Mori K. X-ray dark-field imaging and its application to medicine. *Radiation Physics and Chemistry.* 71: 899-904, 2004.

49) Ando M., Hashimoto E., Hashizume H., Hyodo K., Inoue H., Ishikawa T., Kunisada T., Maksimenko A., Pattanasiriwisawa W., Rubenstein E., Roberson J., Shimao D., Sugiyama H., Takeda K., Ueno E. and Wada H. Development of X-ray dark-field imaging towards clinical application. *Nuclear Sciences and Techniques.* 15: 129-139, 2004.

50) Ando M, Sugiyama H., Kunisada T., Shimao D., Takeda K., Hashizume H. and Inoue H. Construction of X-ray Dark-Field Imaging with a View Size of 80 mm Square and First Visualization of Human Articular Cartilage of Femoral Head under a Nearly Clinical Condition. *Japanese Journal of Applied physics.* 43: L1175-L1177,

2004.

51) Shimao D., Mori K., Sugiyama H. and Hyodo K. Refraction-Contrast Articular Cartilage Image: Comparison of Depiction Abilities between In-Line Holographic Method and a Laue Type Analyzer Method. *Japanese Journal of Applied physics.* 44: 450-451, 2005.

52) Ando M., Yamasaki K., Toyofuku F., Sugiyama H., Ohbayashi C., Li G., Pan L., Jiang X., Pattanasiriwisawa W., Shimao D., Hashimoto E., Kimura T., Tsuneyoshi M., Ueno E., Tokumori K., Maksimenko A., Higashida Y. and Hirano M. Attempt at Visualizing Breast Cancer with X-ray Dark Field Imaging. *Japanese Journal of Applied Physics.* 44: L528-L531, 2005.

53) Keyrilainen J., Fernandez M., Fiedler S., Bravin A., Karjalainen-Lindsberg ML., Virkkunen P., Elo EM., Tenhunen M., Suortti P. and Thomlinson W. Visualisation of calcifications and thin collagen strands in human breast tumor specimens by the diffraction-enhanced imaging technique: a comparison with conventional mammography and histology. *European Journal of Radiology.* 53: 226-237, 2005.

54) Shimao D., Sugiyama H., Kunisada T., Maksimenko A., Toyofuku F., Ueno E., Yamasaki K., Obayashi C., Hyodo K., Li G., Pan L., Jiang X. and Ando M. X-ray Dark-Field Imaging and potential of its clinical application. *Proceedings of SPIE.* 5745: 32-39, 2005.

55) Ando M., Hashimoto E., Hashizume H., Hyodo K., Inoue H., Kunisada T., Maksimenko A., Mori K., Rubenstein E., Roberson J., Shimao D., Sugiyama H., Takeda K., Toyofuku F., Ueno E., Umetani K., Wada H. and Pattanasiriwisawa W. Clinical step onward with X-ray dark-field imaging and perspective view of medical applications of synchrotron radiation in Japan. *Nuclear Instruments & Methods in Physics Research A.* 548: 1-16, 2005.

56) Lewis RA. Medical applications of synchrotron radiation in Australia. *Nuclear Instruments & Methods in Physics Research A.* 548: 23-29, 2005.

57) Takeda T. Phase-contrast and fluorescent X-ray imaging for biomedical researches. *Nuclear Instruments & Methods in Physics Research A.* 548: 38-46, 2005.

58) Wagner A., Aurich M., Sieber N., Stoessel M., Wetzel WD., Schmuck K., Lohmann M., Reime B., Metge J., Coan P., Bravin A., Arfelli F., Rigon L., Menk RH., Heitner G., Irving T., Zhong Z., Muehleman C. and Mollenhauer JA. Options and limitations of joint cartilage imaging: DEI in comparison to MRI and sonography. *Nuclear Instruments & Methods in Physics Research A.* 548: 47-53, 2005.

59) Castro CRF., Barroso RC., de Oliveira LF. and Lopes RT. Coherent scattering X-ray imaging at the Brazilian National Synchrotron Laboratory: Preliminary breast images. *Nuclear Instruments & Methods in Physics Research A.* 548: 116-122, 2005.

60) Shimao D., Sugiyama H., Hyodo K., Kunisada T. and Ando M. Evaluation of X-ray dark-field imaging in visualization of nearly clinical articular cartilage. *Nuclear Instruments & Methods in Physics Research A.* 548: 129-134, 2005.

61) Xiao TQ., Bergamaschi A., Dreossi D., Longo R., Olivo A., Pani S., Rigon L., Rokvic T., Venanzi C. and Castelli E. Effect of spatial coherence on application of in-line phase contrast imaging to synchrotron radiation mammography. *Nuclear Instruments & Methods in Physics Research A.* 548: 155-162, 2005.

62) Siu KKW., Kitchen MJ., Pavlov KM., Gillam JE., Lewis RA., Uesugi K. and Yagi N. An improvement to the diffraction-enhanced imaging

method that permits imaging of dynamic systems. *Nuclear Instruments & Methods in Physics Research A.* 548: 169-174, 2005.

63) Rocha HS., Lopes RT., Valiante PM., Tirao G., Mazzaro I., Honnicke MG., Cusatis C. and Giles C. Diagnosis of thyroid multinodular goiter using diffraction-enhanced imaging. *Nuclear Instruments & Methods in Physics Research A.* 548: 175-180, 2005.

64) Menk RH., Rigon L. and Arfelli F. Diffraction-enhanced X-ray medical imaging at the ELETTRA synchrotron light source. *Nuclear Instruments & Methods in Physics Research A.* 548: 213-220, 2005.

65) Kitchen MJ., Paganin D., Lewis RA., Yagi N. and Uesugi K. Analysis of speckle patterns in phase-contrast images of lung tissue. *Nuclear Instruments & Methods in Physics Research A.* 548: 240-246, 2005.

66) Larsen A., Dale K. and Eek M. Radiographic Evaluation of Rheumatoid Arthritis and Related Conditions by Standard Reference Films. *Acta Radiologica Diagnosis.* 18: 481-491, 1977.

67) Hayes CW. and Conway WF. Evaluation of Articular Cartilage: Radiographic and Cross-sectional Imaging Techniques. *RadioGraphics*. 12: 409-428, 1992.

68) Buckland-Wright JC., Macfarlane DG., Lynch JA., Jasani MK. and Bradshaw CR. Joint space width measures cartilage thickness in osteoarthritis of the knee: high resolution plain film and double contrast macroradiographic investigation. *Annals of the Rheumatic Diseases.* 54: 263-268, 1995.

69) Rovati LC. Radiographic assessment. Introduction: existing methodology. *Osteoarthritis and Cartilage.* 7: 427-429, 1999.

70) Buckland-Wright C. Radiographic assessment of osteoarthritis:

comparison between existing methodologies. *Osteoarthritis and Cartilage.* 7: 430-433, 1999.

71) Vignon E., Conrozier T., Piperno M., Richard S., Carrillon Y. and Fantino O. Radiographic assessment of hip and knee osteoarthritis. Recommendations: recommended guidelines. *Osteoarthritis and Cartilage*. 7: 434-436, 1999.

72) Jansen LMA., van der Horst-Bruinsma IE., van Schaardenburg D., Bezemer PD. and Dijkmans BAC. Predictors of radiographic joint damage in patients with early rheumatoid arthritis. *Annals of the Rheumatic Disease.* 60: 924-927, 2001.

73) Scott DL. The Diagnosis and Prognosis of Early Arthritis: Rationale for New Prognostic Criteria. *Arthritis & Rheumatism.* 46: 286-290, 2002.

74) Guidelines for the Management of Rheumatoid Arthritis 2002 Update. *Arthritis & Rheumatism.* 46: 328-346, 2002.

75) Visser H., le Cessie S., Vos K., Breedveld FC. and Hazes JMW. How to Diagnose Rheumatoid Arthritis Early. A Prediction Model for Persistent (Erosive) Arthritis. *Arthritis & Rheumatism.* 46: 357-365, 2002.

76) Lehner KB., Rechl HP., Gmeinwieser JK., Heuck AF., Lukas HP. and Kohl HP. Structure, Function, and Degeneration of Bovine Hyaline Cartilage: Assessment with MR Imaging in Vitro. *Radiology.* 170: 495-499, 1989.

77) Modl JM., Sether LA., Haughton VM. and Kneeland JB. Articular Cartilage: Correlation of Histologic Zones with Signal Intensity at MR Imaging. *Radiology.* 181: 853-855, 1991.

78) Rubenstein JD., Kim JK., Morava-Protzner I., Stanchev PL. and Henkelman RM. Effects of Collagen Orientation on MR Imaging Characteristics of Bovine Articular Cartilage. *Radiology.* 188: 219-226, 1993.

79) Disler DG., McCauley TR., Kelman CG., Fuchs MD. Ratner LM., Wirth CR. and Hospodar PP. Fat-Suppressed Three-Dimensional Spoiled Gradient-Echo MR Imaging of Hyaline Cartilage Defects in the Knee: Comparison with Standard MR Imaging and Arthroscopy. *American Journal of Roentgenology.* 167: 127-132, 1996.

80) Hodler J. and Resnick D. Current status of imaging of articular cartilage. *Skeletal Radiology.* 25: 703-709, 1996.

81) Mlynarik V., Degrassi A., Toffanin R., Vittur F., Cova M. and Pozzi-Mucelli RS. Investigation of laminar appearance of articular cartilage by means of magnetic resonance microscopy. *Magnetic Resonance Imaging.* 14: 435-442, 1996.

82) Rubenstein JD., Kim JK., Henkelman RM. Effects of Compression and Recovery on Bovine Articular Cartilage: Appearance on MR Images. *Radiology.* 201: 843-850, 1996.

83) Waldschmidt JG., Rilling RJ., Kajdacsy-Balla AA., Boynton MD. and Erickson SJ. In Vitro and in Vivo MR Imaging of Hyaline Cartilage: Zonal Anatomy, Imaging Pitfalls, and Pathologic Conditions. *RadioGraphics.* 17: 1387-1402, 1997.

84) Brossmann J., Frank LR., Pauly JM., Boutin RD., Pedowitz RA., Haghighi P. and Resnick D. Short Echo Time Projection Reconstruction MR Imaging of Cartilage: Comparison with Fat-suppressed Spoiled GRASS and Magnetization Transfer Contrast MR Imaging. *Radiology.* 203: 501-507, 1997.

85) Dardzinski BJ., Mosher TJ., Li S., van Slyke MA. and Smith MB. Spatial Variation of T2 in Human Articular Cartilage. *Radiology.* 205: 546-550, 1997.

86) Freeman DM., Bergman G. and Glover G. Short TE MR Microscopy: Accurate Measurement and Zonal Differentiation of Normal Hyaline Cartilage. *Magnetic Resonance in Medicine.* 38: 72-81, 1997.

87) McCauley TR. and Disler DG. MR Imaging of Articular Cartilage. *Radiology.* 209: 629-640, 1998.

88) Loeuille D., Olivier P., Mainard D., Gillet P., Netter P. and Blum A. Magnetic resonance imaging of normal and osteoarthritic cartilage. *Arthritis & Rheumatism.* 41: 963-975, 1998.

89) Disler DG. and McCauley TR. Clinical Magnetic Resonance Imaging of Articular Cartilage. *Topics in Magnetic Resonance Imaging.* 9: 360-376, 1998.

90) Gründer W., Wagner M. and Werner A. MR-Microscopic Visualization of Anisotropic Internal Cartilage Structures Using the Magic Angle Technique. *Magnetic Resonance in Medicine.* 39: 376-382, 1998.

91) Waldschmidt JG., Braunstein EM. and Buckwalter KA. Magnetic resonance imaging of osteoarthritis. *Osteoarthritis.* 25: 451-465, 1999.

92) Klarlund M., Ostergaard M., Gideon P., Sorensen K., Jensen KE. and Lorenzen I. Wrist and finger joint MR imaging in rheumatoid arthritis. *Acta Radiologica.* 40: 400-409, 1999.

93) Wada Y., Watanabe A., Yamashita T., Isobe T. and Moriya H. Evaluation of articular cartilage with 3D-SPGR MRI after autologous chondrocyte implantation. *Journal of Orthopaedic Science.* 8:

514-517, 2003.

94) Yelin E., Meenan R., Nevitt M. and Epstein W. Work disability in rheumatoid arthritis: effects of disease, social, and work factors. *Annals of Internal Medicine.* 93: 551-556, 1980.

95) Pincus T., Callahan LF., Sale WG., Brooks AL., Payne LE. and Vaughn WK. Severe functional declines, work disability, and increased mortality in seventy-five rheumatoid arthritis patients studied over nine years. *Arthritis & Rheumatism.* 27: 864-872, 1984.

96) Pincus T., Callahan LF. and Vaughn WK. Questionnaire, walking time and button test measures of functional capacity as predictive markers for mortality in rheumatoid arthritis. *Journal of Rheumatology.* 14: 240-251, 1987.

97) Pincus T. New concepts in prognosis of rheumatic diseases for the 1990s, edited by Bellamy N. Prognosis in the Rheumatic Diseases. Dordrecht: Kluwer Academic Publishers, pp 451-492, 1991.

98) Pincus T. and Callahan LF. Early mortality in RA predicted by poor clinical status. *Bulletin on the Rheumatic Diseases*. 41: 1-4, 1992.

99) Lipsky PE., van der Heijde DMFM., Clair EWS., Furst DE., Breedveld FC., Kalden JR., Smolen JS., Weisman M., Emery P., Feldmann M., Harriman GR. and Maini RN. Infliximab and Methotrexate in the Treatment of Rheumatoid Arthritis. *The New England Journal of Medicine.* 343: 1594-1602, 2000.

100) Simon M., Girbal E., Sebbag M., Gomes-Daudrix V., Vincent C., Salama G. and Serre G. The Cytokeratin Filament-Aggregating Protein Filaggrin Is the Target of the So-called "Antikeratin Antibodies," Autoantibodies Specific for Rheumatoid Arthritis. *Journal of Clinical Investigation.* 92: 1387-1393, 1993.

101) Sebbag M., Simon M., Vincent C., Masson-Bessiere C., Girbal E., Durieux JJ. and Serre G. The Antiperinuclear Factor and the So-called Antikeratin Antibodies Are the Same Rheumatoid Arthritis-Specific Autoantibodies. *Journal of Clinical Investigation.* 95: 2672-2679, 1995.

102) Girbal-Neuhauser E., Durieux JJ., Arnaud M., Dalbon P., Sebbag M., Vincent C., Simon M., Senshu T., Masson-Bessiere C., Jolivet-Reynaud C., Jolivet M. and Serre G. The Epitopes Targeted by the Rheumatoid Arthritis-Associated Antifilaggrin Autoantibodies are Posttranslationally Generated on Various Sites of (Pro)Filaggrin by Deimination of Arginine Residues. *The Journal of Immunology.* 162: 585-594, 1999.

103) Schellekens GA., de Jong BAW., van den Hoogen FHJ., van de Putte LBA. and van Venrooij WJ. Citrulline is an Essential Constituent of Antigenic Determinants Recognized by Rheumatoid Arthritis-specific Autoantibodies. *Journal of Clinical Investigation.* 101: 273-281, 1998.

104) Schellekens GA., Visser H., de Jong BAW., van den Hoogen FHJ., Hazes JMW., Breedveld FC. and van Venrooij WJ. The Diagnostic Properties of Rheumatoid Arthritis Antibodies Recognizing a Cyclic Citrullinated Peptide. *Arthritis & Rheumatism.* 43: 155-163, 2000.

105) Korn GA. and Korn TM. Mthematical Handbook for Scientists and Engineers: Definitions, Theorems and Formulas for Reference and Review. *Dover Publications, Inc New York.* 2000.

106) ICRU report 44. Tissue Substitutes in Radiation Dosimetry and measurement. *International Commission on Radiation Units and Measurement.* 1989.

107) Kohra K. An Application of Asymmetric Reflection for Obtaining X-ray Beams of Extremely Narrow Angular Spread. *Journal of Physics Society Japan.* 17: 589-590, 1962.

108) Zachariasen WH. Theory of X-ray Diffraction in Crystal. *Dover Publications, Inc New York.* 1967.

109) Handbooks on Synchrotron Radiation, Vol. 3, edited by Brown GS. and Moncton DE. *Elsevier Science Publishers B.V.* 1991.

110) Kikuta S. X sen Kaisetsu – Sanran Gizyutsu (Zyou), 2nd edition. *Tokyo Daigaku Syuppan Kai.* 1996.

111) ICRU report 17. Radiation Dosimetry: X Rays Generated at Potentials of 5 to 150 kV. *International Commission on Radiation Units and Measurement.* 1970.

112) Klevenhagen SC. Experimentally determined backscatter factors for x-rays generated at voltages between 16 and 140 kV. *Physics in Medicine and Biorogy.* 34: 1871-1882, 1989.

113) Grosswendt B. Dependence of the photon backscatter factor for water on source to phantom distance and irradiation field size. *Physics in Medicine and Biology.* 35: 1233-1245, 1990.

114) Sugita Y., Sugiyama H., Iida S. and Kawata H. Measurement of the Static Debye-Waller Factor of Silicon Crystals by the Pendellösung Fringe Method. *Japanese Journal of Applied Physics.* 26: 1903-1906, 1987.

115) Iida S., Sugiyama H., Sugita Y. and Kawata H. Measurement and Analysis of the Debye-Waller Factor of Cz-Silicon with Small Oxygen Precipitates. *Japanese Journal of Applied Physics.* 27: 1081-1087, 1988.

116) Okitsu K., Iida S., Sugita Y., Takeno H., Yagou Y. and Kawata H. Numerically Simulated and Experimentally Obtained X-ray Section Topographs of a Spherical Strain Field in a Floating Zone Silicon Crystal. *Japanese Journal of Applied Physics.* 31: 3779-3785, 1992.

117) Stoller DW. Magnetic Resonance Imaging in Orthopaedics & Sports Medicine. *J.B. Lippincott Company.* 1989.

118) Yoshioka H, Haishi T., Uematsu T., Matsuda Y., Itai Y. and Kose K. MR Microscopy of the Articular Cartilage with a 1.0T Permanent Magnet Portable MR System: Preliminary Results. *Magnetic Resonance in Medical Sciences.* 2: 51-55, 2003.

119) International Basic Safety Standards for Protection against Ionizing Radiation and for the Safety of Radiation Sources. *IAEA Safety Series.* No. 115: 279-280, 1996.